2011

Flat Indentation of Filled and Unfilled PDMS

Amir Mohammad Nazari

Flat Indentation of Filled and Unfilled PDMS

(Spine title: Flat Indentation of Filled and Unfilled PDMS)

(Thesis Format: Monograph)

by

Amir Mohammad Nazari

Graduate Program

in

Engineering Science

Department of Mechanical and Materials Engineering

A thesis submitted in partial fulfillment

of the requirements for the degree of

Master of Engineering Science

School of Graduate and Postdoctoral Studies

The University of Western Ontario

London, Ontario, Canada

THE UNIVERSITY OF WESTERN ONTARIO

SCHOOL OF GRADUATE AND POSTDOCTORAL STUDIES

CERTIFICATE OF EXAMINATION

Supervisor	Examiners
Dr. D. M. Shinozaki	Dr. R. Klassen
	Dr. L. Jiang
	Dr. P. Simpson

The thesis by

Amir Mohammad Nazari

Entitled:

Flat Indentation of Filled and Unfilled PDMS

is accepted in partial fulfillment of the

requirements for the degree of

Master of Engineering Science

Date _____

_____

Chair of the Thesis Examination Board

ABSTRACT

Recently, Polydimethylsiloxane (PDMS) has attracted much attention as a useful polymer in various fields due to its excellent properties. On the contrary poor mechanical properties are the major drawbacks of PDMS which has led to many researches to overcome this deficiency.

One way to enhance the mechanical properties and broaden the applications is preparation of nanocomposite of PDMS and clay along with probing the mechanical properties. Among the mechanical characterization methods, indentation technique is known as a useful method to examine the local mechanical properties of PDMS and PDMS-clay nanocomposites.

In this study, flat indentation test is carried out on bulk PDMS and PDMS-clay nanocomposites. Validity of the Sneddon's theory proposed for flat cylindrical indenter is approved in terms of both elastic deformations under the flat tip and indentation load-displacement behavior for filled and unfilled PDMS. Moreover effect of clay and cross-linker amount on the stress fields and indentation load-displacement curves is discussed. Stress distributions along radial distance by finite element analysis (FEA) are examined to investigate the reason of radial crack initiation during indentation test.

Indentation test of thin films of PDMS and PDMS-clay filled nanocomposite adhering to the rigid substrate was also conducted. Distribution of the radial and shear stresses near the interface regime is examined by FEA to assess the validity of Dehm et al.'s model. The result showed a good agreement with Dehm's model which was used to compute the critical interfacial shear strength leading failure in the interface of thin film and substrate.

Keywords: Polydimethylsiloxane, Indentation, nanocomposite, finite element analysis, interfacial shear strength.

To my parents, sister& niece

AKNOWLEDGEMENT

I am really indebted to my parents who unremittingly supported me to make this work possible.

I wish to express my special thanks to my dearest friend, Hadi Vafadar Moradi, for his invaluable assistance, his encouragement and immense support.

There are many other people who helped me and I would like to thank them all, however listing their names here would be impossible.

TABLE OF CONTENTS

LIST OF TABLES

LIST OF FIGURES

SYMBOLS AND NOMENCLATURE

a	Indenter Radius
$2a$	Indenter diameter
r/a	Normalized radial distance
E	Elastic modulus
F	Indenter load
F_c	Critical indentation debonding load
h	Indentation displacement
h_f	Critical indentation debonding depth
P	Indentation stress
P_c	Critical indentation debonding stress
R	Cross-linker ratio
V	Indenter velocity
W	Elastic strain energy density
u_z	Displacement in Z-direction
u_r	Displacement in radial direction
σ_Z	Axial stress
σ_r	Radial stress
σ_θ	Hoop stress
τ_{max}	Critical interfacial shear stress
υ	Poisson's ratio
λ_0	Wavelength of the sinusoidal function
δ	Coating thickness

Chapter 1. INTRODUCTION

Polydimethylsiloxane (PDMS) is one of the widely used types of the organosilicon compounds classified in the rubber-like materials group. Materials in this category are well known for large geometric changes of initial shape and recovery capacity from large deformation. Over the last two decades several studies have been conducted on PDMS due to its promising properties such as chemical inertness, low density, high fracture toughness, no toxicity and bio compatibility. PDMS has been mostly utilized as a coating material for insulation and anticorrosion. It is also used in micro-fluid devices, micro and nanofabrication, optical systems, deformable electronics and biomedical applications.

However, poor tensile properties of PDMS remain the main challenges to overcome. Previous researches have shown that the mechanical properties of PDMS can be enhanced using fillers as reinforcement such as carbon black in polymer matrix (Kraus 1965, 1978). Among various tested fillers, layered silicate is of particular interest due to high surface area and surface reactivity (Giannelis et al. 1995, 2000), (Wang et al. 1998), (Takeuchi et al. 1999), (Pinnavaia et al. 2001).

It is essential to characterize mechanical properties of the bulk and thin films of PDMS and clay filled-PDMS nanocomposites for successful application. There are different methods and approaches available for mechanical properties characterization such as uniaxial tensile test. Indentation has arisen as an easy and non-destructive tool for measuring mechanical properties of small local volumes such as yield stress, fracture stress, ductility and hardness. In the other word, using indentation method it is possible to characterize the thin film and coating materials without removing them from substrate.

According to author's knowledge little has been done with regards to the indentation of the nanocomposites of PDMS and clay, and the examination of the stress fields near the indenter especially in the case of the cylindrical flat indenter.

This thesis investigates the mechanical properties of the bulks and thin films of PDMS and clay-filled PDMS nanocomposites using indentation test. The study also includes the modeling of the indentation which is crucial for effective use of the method.

Finite Element Analysis (FEA) application program ABAQUS was used for modeling under the same conditions as applied during experimental procedures.

Chapter four discusses the indentation of the bulk PDMS samples containing various degrees of cross-linker, and clay-PDMS nanocomposites with different amounts of clay to investigate:

1- The validity of the load-displacement relation proposed by Sneddon (1945) for the load-displacement curves obtained by indentation of PDMS and clay-PDMS nanocomposites.

2- The agreement of radial, axial, hoop and shear stress distribution along radial distance obtained by FEA in this study with the Sneddon's theory.

3- The effect of the clay and cross-linker amount on the load-displacement curves and stress contours obtained by indentation test and FEA respectively.

4- Crack initiation through examination of the hoop and radial stress distribution along the radial distance.

In chapter five, the indentation of the thin films of PDMS with various degrees of cross-linker and clay filled PDMS nanocomposites containing different amounts of clay adhering to the glass substrate is studied to investigate:

1- The agreement of shear and radial stresses distribution near the substrate and thin film interface with model proposed by Dehm et al. and calculation of the interfacial shear strength by Dehm et al.'s method.

2- The effect of cross-linker amount on the interfacial shear strength.

Chapter 2. LITERATURE REVIEW

2.1 Rubbery Materials

Rubber-like materials have remarkable mechanical properties including large geometric changes of their initial shapes and their capacity to recover from large deformation. These materials do not follow a linear stress-strain behavior; therefore a nonlinearity stress-strain relationship is defined for the rubbery materials. Such mechanical behavior is modeled adequately by hyperelasticity. Hyperelasticity is the capability of a material to undergo large elastic strain due to small forces, without losing its original properties.

Hyperelastic constitutive relations are expressed by a single function, W, which describes the elastic strain energy density.

Mooney (1940), Rivlin and Saunders (1951) proposed a theory of large elastic deformation of rubber. Blatz and Ko (1962) presented a new strain energy function to the deformation of rubbery materials, and also Yeoh (1993) suggested a strain-energy function for the characterization of carbon-black filled rubber. Ogden (1972) stated an energy function for the characterization of rubber-like solids for nonlinear large elastic deformations based on strain energy density functions.

2.1.1 Strain energy models defined for hyperelastic materials

In this section, the strain energy of the hyperelastic materials will be calculated. Due to the importance of the deformation gradient tensor and green strain tensor in defining strain energy (W), they will also be explained.

- Deformation gradient tensor

The first thing which should be considered is to measure displacement and deformation through space. A change in the configuration of a continuum body results in a displacement. The displacement of a body has two components: a rigid-body

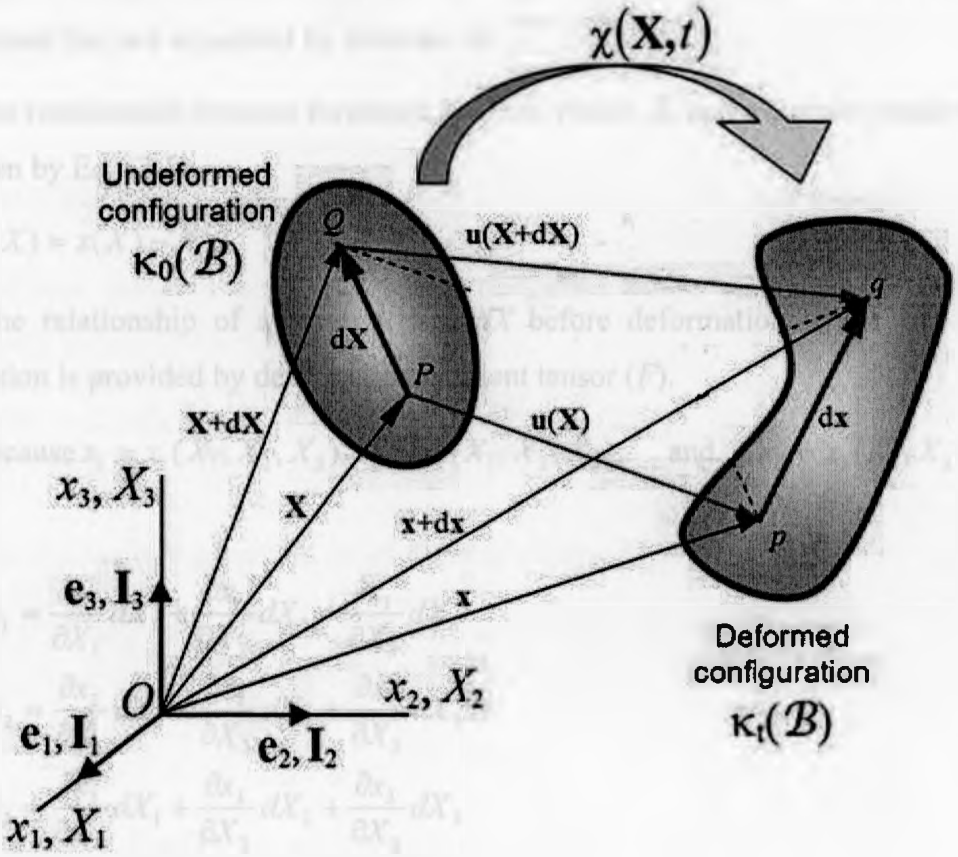

Figure 2.1: Motion of continuum body (Wikipedia).

displacement and a deformation. A rigid-body displacement consists of a simultaneous translation and rotation of the body without changing its shape or size. Deformation implies the change in shape and/or size of the body from an initial or undeformed configuration $\kappa_0(\beta)$ to a current or deformed configuration $\kappa_t(\beta)$ as shown in Figure 2.1.

Consider two neighboring material particles P and Q that are infinitesimally close to each other separated by distance dX in the reference configuration $\kappa_0(\beta)$. In the deformed or current configuration $\kappa_t(\beta)$, the materials points P and Q take up positions p and q where they are separated by distance dx.

The relationship between reference position vector, X, and a current position vector, x, is given by Eq. (2.1):

$$u(X) = x(X) - X \tag{2.1}$$

The relationship of a material line dX before deformation to the line dx after deformation is provided by deformation gradient tensor (F).

Because $x_1 = x_1(X_1, X_2, X_3), x_2 = x_2(X_1, X_2, X_3),$ and $x_3 = x_3(X_1, X_2, X_3),$ we have:

$$\begin{aligned} dx_1 &= \frac{\partial x_1}{\partial X_1} dX_1 + \frac{\partial x_1}{\partial X_2} dX_2 + \frac{\partial x_1}{\partial X_3} dX_3 \\ dx_2 &= \frac{\partial x_2}{\partial X_1} dX_1 + \frac{\partial x_2}{\partial X_2} dX_2 + \frac{\partial x_2}{\partial X_3} dX_3 \\ dx_3 &= \frac{\partial x_3}{\partial X_1} dX_1 + \frac{\partial x_3}{\partial X_2} dX_2 + \frac{\partial x_3}{\partial X_3} dX_3 \end{aligned} \tag{2.2}$$

These three relations can be written in matrix notation as:

$$\begin{Bmatrix} dx_1 \\ dx_2 \\ dx_3 \end{Bmatrix} = \begin{bmatrix} \frac{\partial x_1}{\partial X_1} & \frac{\partial x_1}{\partial X_2} & \frac{\partial x_1}{\partial X_3} \\ \frac{\partial x_2}{\partial X_1} & \frac{\partial x_2}{\partial X_2} & \frac{\partial x_2}{\partial X_3} \\ \frac{\partial x_3}{\partial X_1} & \frac{\partial x_3}{\partial X_2} & \frac{\partial x_3}{\partial X_3} \end{bmatrix} \begin{Bmatrix} dX_1 \\ dX_2 \\ dX_3 \end{Bmatrix} \equiv [F] \begin{Bmatrix} dX_1 \\ dX_2 \\ dX_3 \end{Bmatrix} \tag{2.3}$$

Where *[F]* is the matrix associated with the deformation gradient tensor F.

$$[F]=\begin{bmatrix} \frac{\partial x_1}{\partial X_1} & \frac{\partial x_1}{\partial X_2} & \frac{\partial x_1}{\partial X_3} \\ \frac{\partial x_2}{\partial X_1} & \frac{\partial x_2}{\partial X_2} & \frac{\partial x_2}{\partial X_3} \\ \frac{\partial x_3}{\partial X_1} & \frac{\partial x_3}{\partial X_2} & \frac{\partial x_3}{\partial X_3} \end{bmatrix} \tag{2.4}$$

Also Eq. (2.2) could be written in the form of Eq. (2.5).

$$dx = F.dX = dX.F^T, F = (\frac{\partial x}{\partial X})^T \tag{2.5}$$

-Green strain tensor

Distance between points *P* and *Q (dx)* and points *p* and *q (dX)* are given respectively by Eq. (2.6).

$$\begin{aligned} (dS)^2 &= dX.dX = dX_i dX_i = (dX_1)^2 + (dX_2)^2 + (dX_3)^2 \\ (ds)^2 &= dx.dx = dx_i.dx_i = (dx_1)^2 + (dx_2)^2 + (dx_3)^2 \end{aligned} \tag{2.6}$$

The change in the squared lengths can be expressed as:

$$(ds)^2 - (dS)^2 = dx.dx - dX.dX = dX.(F^T.F).dX - dX.dX = 2dX.E.dX \tag{2.7}$$

$$E = \frac{1}{2}(F^T.F - I) \tag{2.8}$$

E is called green strain tensor. In the index notation, the rectangular Cartesian components of *E* are given by:

$$E_{ij} = \frac{1}{2}(\frac{\partial u_i}{\partial X_j} + \frac{\partial u_j}{\partial X_i} + \frac{\partial u_k}{\partial X_i}\frac{\partial u_k}{\partial X_j}) \tag{2.9}$$

The normal strains E_{11}, E_{22}, E_{33} and shear strains E_{12}, E_{23}, E_{13} could be written using Eq. (2.9).

$$E_{11} = \frac{\partial u_1}{\partial X_1} + \frac{1}{2}\left[\left(\frac{\partial u_1}{\partial X_1}\right)^2 + \left(\frac{\partial u_2}{\partial X_1}\right)^2 + \left(\frac{\partial u_3}{\partial X_1}\right)^2\right]$$

$$E_{22} = \frac{\partial u_2}{\partial X_2} + \frac{1}{2}\left[\left(\frac{\partial u_1}{\partial X_2}\right)^2 + \left(\frac{\partial u_2}{\partial X_2}\right)^2 + \left(\frac{\partial u_3}{\partial X_2}\right)^2\right]$$

$$E_{11} = \frac{\partial u_3}{\partial X_3} + \frac{1}{2}\left[\left(\frac{\partial u_1}{\partial X_3}\right)^2 + \left(\frac{\partial u_2}{\partial X_3}\right)^2 + \left(\frac{\partial u_3}{\partial X_3}\right)^2\right] \tag{2.10}$$

$$E_{12} = \frac{1}{2}\left(\frac{\partial u_1}{\partial X_2} + \frac{\partial u_2}{\partial X_1} + \frac{\partial u_1}{\partial X_1}\frac{\partial u_1}{\partial X_2} + \frac{\partial u_2}{\partial X_1}\frac{\partial u_2}{\partial X_2} + \frac{\partial u_3}{\partial X_1}\frac{\partial u_3}{\partial X_2}\right)$$

$$E_{23} = \frac{1}{2}\left(\frac{\partial u_2}{\partial X_3} + \frac{\partial u_3}{\partial X_2} + \frac{\partial u_1}{\partial X_2}\frac{\partial u_1}{\partial X_3} + \frac{\partial u_2}{\partial X_3}\frac{\partial u_2}{\partial X_3} + \frac{\partial u_3}{\partial X_2}\frac{\partial u_3}{\partial X_3}\right)$$

$$E_{13} = \frac{1}{2}\left(\frac{\partial u_1}{\partial X_3} + \frac{\partial u_3}{\partial X_1} + \frac{\partial u_1}{\partial X_1}\frac{\partial u_1}{\partial X_3} + \frac{\partial u_2}{\partial X_1}\frac{\partial u_2}{\partial X_3} + \frac{\partial u_3}{\partial X_1}\frac{\partial u_3}{\partial X_3}\right)$$

-Strain energy models

The right Cauchy-Green tensor, A is obtained from the deformation gradient such that

$$A = F^T.F \tag{2.11}$$

and A is used to define the following strain invariants:

$$I_1 = \lambda_1^2 + \lambda_2^2 + \lambda_3^2 = tr(A)$$

$$I_2 = \lambda_1^2\lambda_2^2 + \lambda_2^2\lambda_3^2 + \lambda_1^2\lambda_3^2 = \frac{1}{2}\left(I_1^2 - tr(A)\right) \tag{2.12}$$

$$I_3 = \lambda_1^2.\lambda_2^2.\lambda_3^2 = \det(A)$$

Here, the λ_i's and I_i's are the principal stretch ratios and strain invariants respectively. I_3 is a volumetric constant. Hyperelastic materials are assumed to be incompressible ($\Delta V = 0$), so I_3 takes unity.

$$\lambda_1^2\lambda_2^2\lambda_3^2 = 1 \tag{2.13}$$

The strain energy, W, is usually expressed as a function of strain invariants, $W(I_1, I_2, I_3)$or principal stretch ratios,$W(\lambda_1, \lambda_2, \lambda_3)$, depending on the hyperelastic model. Some hyperelastic models would be explained as follows:

1-Mooney-Rivilin model: Rivlin Proposed a strain-energy-based model for incompressible hyperelasticity, commonly referred to as the polynomial or the Mooney-Rivlin model, which takes the following form:

$$W = \sum_{i,j}^{\infty} C_{ij} (I_1 - 3)^i (I_2 - 3)^j \tag{2.14}$$

where C_{ij} is constant. For example, the Mooney-Rivlin form with two parameters is:

$$W = C_{10}(I_1 - 3) + C_{01}(I_2 - 3) \tag{2.15}$$

2-Neo-Hookean model: This model was suggested by Treloar and taking only the first term of Eq.(2.15), the Neo-Hookean model is obtained by:

$$W = C_{10}(I_1 - 3) \tag{2.16}$$

3-Yeoh or reduced polynomial model: Yeoh suggested another model in 1993 which can be derived from Rivlin's formulation, Eq.(2.14), under the assumption that the second strain invariant, I_2, is constant with stretch and thus does not contribute in the strain energy function.

$$W = \sum_{i=1}^{N} C_{i0} (I_1 - 3)^i \tag{2.17}$$

2.2 Polydimethylsiloxane (PDMS)

Polysiloxane silicone rubber is one of the various types of the synthetic rubbery materials. The main polymer chain of polysiloxane silicone rubber is composed of silicium and oxygen atoms rather than hydrocarbons and the most widely used grade of the silicone rubbers is polydimethylsiloxane (PDMS) as shown in the Figure 2.2. PDMS was first synthesized by General Electric and Dow Corning and consequently was commercialized in 1945 (Hofmann 1989).

2.2.1 Cross-linking PDMS

PDMS acts as a viscous liquid due to free movement of its chains in the room temperature. Therefore, when it is stretched or compressed, it cannot return to the original state. In the other word, PDMS exhibits plastic or irreversible deformation until it is cross-linked. Cross-linking is a process by which elastomeric materials are generally prepared; it consists of the formation of a molecular network by a chemical tying of independent chain molecules. The cross-linking PDMS can retrieve to the original state after large imposed deformations. Generally cross-linking can be categorized in two groups as follows:

1- Random cross-linking: Polymer chains can be connected anywhere along the chain.

2- Selective cross-linking: End-linking of the PDMS chains is an example for this kind of cross-linking.

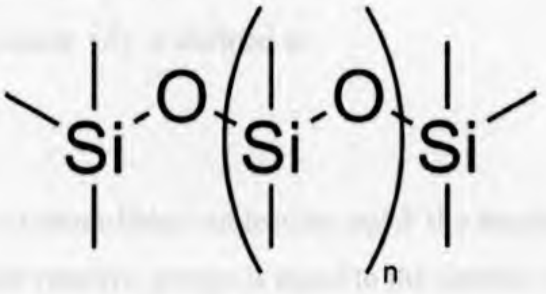

Figure 2.2: Schematic structure of the polydimethylsiloxane including silicium and oxygen atoms in the main chain and methyl in the side groups where n is the number of the repeating monomer $[SiO(CH_3)_2]$ units (Wikipedia).

Tetraethylorthosilicate (TEOS) as a cross-linker and tin(II)-ethylhexanoate as a catalyst were used to cross-link PDMS chains by means of end linking method. TEOS has four reactive groups. It can release an ethyl group in reaction with the chain end and make connection with the chain ends as shown in Eq.(2.18) (Moloodi et al. 2009).

$$\sim\sim [SiO(CH_3)_2]-OH + (OC_2H_5)_3Si - C_2H_5 \rightarrow \\ \sim\sim [SiO(CH_3)_2]-OSi(OC_2H_5)_3Si + C_2H_5OH \quad (2.18)$$

Ratio of the cross-linker (R) is defined as:

$$R = \frac{4M}{2N} \quad (2.19)$$

where M is the number of cross-linker molecules and N the number of polymer chains. If the number of cross-linker reactive groups is equal to the number of chain ends, R is one. In an ideal case all of the reactive groups react with the chain ends and there is no free chain end and no unused cross-linker.

Takeuchi (1999) reported that there are some side reactions that occur during cross-linking of the PDMS and they are given in Eqs.(2.20) and (2.21).

$$\sim\sim Si(Me)_2OH + \sim\sim Si(Me)_2OH \rightarrow \sim\sim SiOSi \sim\sim + H_2O \quad (2.20)$$

$$(EtO)_3SiOEt + (EtO)_3SiOEt\ (H_2O) \rightarrow (EtO)_3SiOSi(EtO)_3 + 2EtOH \quad (2.21)$$

Due to side reactions, steric hindrance and possible existence of more than two reactive groups per chain (Patel, 1992) an extra cross-linker is required for cross-linking of all the chain ends.

Patel (1992) stated that $R = 2.2$ was the optimum amount of the cross-linker using for hydroxyl terminated PDMS where the molecular weight was 23 kg/mol. This amount of cross-linker was the best for obtaining the highest elastic modulus.

In situ formation of the silica due to the presence of the extra cross-linker can occur in the solution (Moloodi 2009). Extra TEOS is hydrolyzed by the water simply absorbed during mixing to precipitate the SiO_2 filler into a cross-linked PDMS network. The reaction below shows the in situ formation of the silica in system.

$$Si(OC_2H_5)_4 + 2H_2O \rightarrow SiO_2 + 4C_2H_5OH \quad (2.22)$$

2.2.2 Properties of the cross-linked PDMS

PDMS is chosen for many applications owing to its outstanding properties as mentioned below:

- Low melting and glass-transition temperature
- Much more stable than hydrocarbon chains due to the higher bond energy of a $Si-O$ bond ($373\ KJ.mole^{-1}$) than that of a $C-C$ bond ($343 KJ.mole^{-1}$)
- Low density
- Excellent resistance to electromagnetic radiation compared to the other elastomers
- Chemical inertness
- Above approximately $150°C$, PDMS shows the best mechanical properties of all elastomers
- Low temperature flexibility, PDMS only hardens below -50 and become brittle.
- Highly hydrophobic surface
- Transparency
- No toxicity and biocompatibility

Recently PDMS has been widely used in soft lithography, biomedical application, microfluidic, optical systems. Furthermore PDMS has attracted much attention in deformable electronics such as paper like displays, electronic skins for robots and humans, flexible solar cells and sensor skins. These applications consist of a stretchable polymer (PDMS) fabricated on a rigid substrate (silicon nitride) and a thin film of the conductive metallic layers deposited on the polymer (Xiang et al. 2005) (Li et al. 2007) (Lu et al. 2007).

Poor tensile properties and high cost of making PDMS are the drawbacks of it. In some applications such as tunable microdoublet lenses and dielectric elastomer actuators the mechanical response of PDMS under applied loading is one of the major issues (Choi et al. 2008). So the use of fillers such as silica can partly solve the weak mechanical

properties of PDMS. Lately a commercial PDMS product named "Sylgard" which has approximately 60 percent by weight of silica filler have been made by Dow Corning.

2.3 Clay filled PDMS

Recently many efforts have been made to improve the weak mechanical properties of the PDMS. One of the valuable methods was to add clay to PDMS. The first reported use of clay platelets was patented by Gianino and Angelone.

Layered silicate is one of the most important types of nanoclay. Due to some properties such as high surface area and surface reactivity, they are being considered as a reinforcement in polymer matrix. Layered silicates are composed of a fraction of hydrous, magnesium, or aluminum silicates with two types of sheets, tetrahedral and octahedral.

As shown in Figure 2.3, every clay platelet has thickness of almost 1*nm* and the lateral dimension of the platelet may vary from 30 *nm* to several microns.

There are two important categories of clay: -1:1, -2:1.

When one octahedral sheet is bonded to one tetrahedral sheet, a 1:1 clay mineral results. Hectorite, saponite, and montmorillonite are the most commonly types of layered silicate with 2:1 structure. In this structure there are two tetrahedral and one octahedral layer. Figure 2.4 depicts the structure of 2:1 phyllosilicates. Stacking of the layers makes Van der Waals gap between the layers called gallery or interlayer.

Isomorphic substitution within the layers generates negative charges that are counterbalanced by alkali and alkaline earth cations placed inside the galleries, and this structure gives them hydrophilic properties.

This hydrophilic property is a main problem of Layered silicates. To solve this problem, the hydrophilic surface of layered silicates should convert to an organophilic surface to be compatible with an organic matrix. This can be performed by an ion-exchange reaction with cationic surfactants such as primary, secondary alkylphophonium.

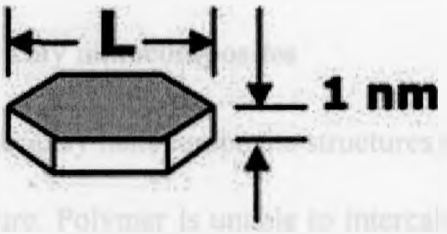

One Clay Platelet

L: 100 – 200 nm in case of MMT

Figure 2.3: General shape of one clay platelet (Ray et al. 2003).

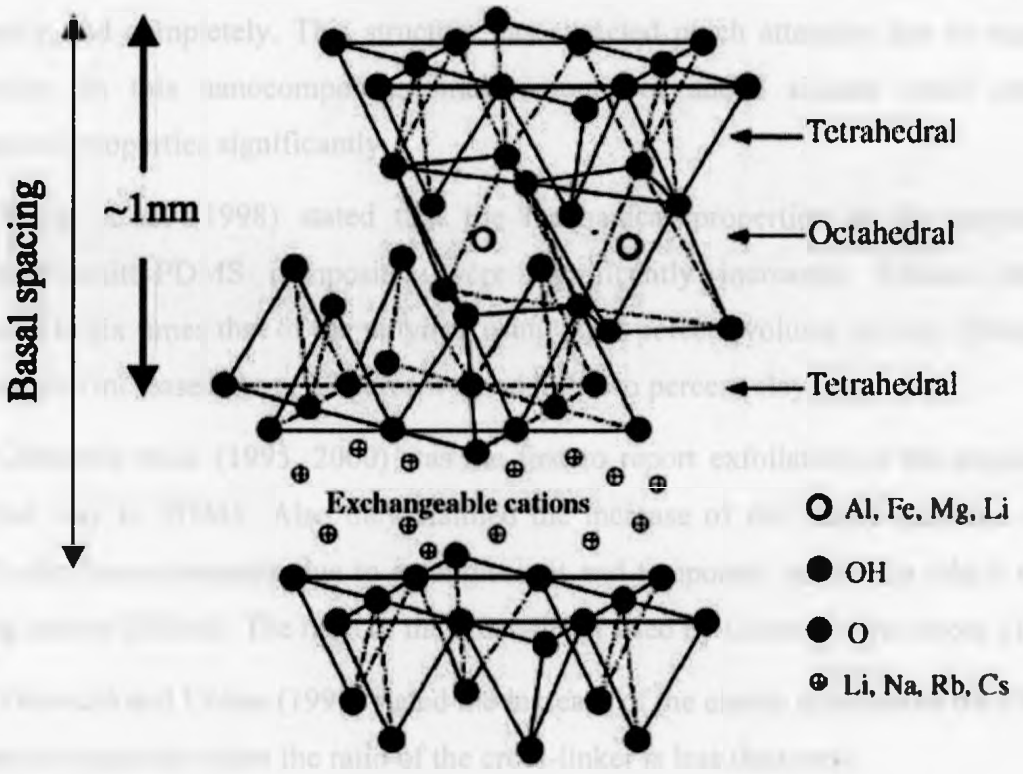

Figure 2.4: Basic structures of 2 : 1 clay minerals (Ray et al. 2003).

2.3.1 Structures of polymer clay nanocomposites

Three types of polymer-clay nanocomposite structures are shown in Figure 2.5.

a- Conventional structure. Polymer is unable to intercalate between silicate sheets. In this structure, the properties of nanocomposites would be weak because of poor interfacial adhesion between polymer and clay.

b- Intercalated structure. Extended polymer chains are inserted into the gallery space between parallel silicate layers. In this structure, the properties would be better in comparison with the previous structure. The electrostatic force between the clay particles is too much for the polymer chains to push them away from each other.

c- Exfoliated structure. Individual silicate layers are separated in polymer matrix uniformly and completely. This structure has attracted much attention due to excellent properties. In this nanocomposite, small amount of added silicate could enhance mechanical properties significantly.

Wang et al. (1998) stated that the mechanical properties of the intercalated montmorrillonite-PDMS composites were significantly increased. Tensile strength increased to six times that of the polymer using eight percent volume of clay. Elongation at break also increased about 80 percent by adding two percent clay.

Giannelis et al. (1995, 2000) was the first to report exfoliation of the organically modified clay in PDMS. Also they claimed the increase of the elastic modulus of the PDMS-clay nanocomposite due to entanglement and temporary restriction which makes moving chains difficult. The ratio of the cross-linker used by Giannelis was about 11.

Takeuchi and Cohen (1999) stated the increase of the elastic modulus of the PDMS-clay nanocomposites when the ratio of the cross-linker is less than one.

Pinnavaia et al. (2001) reported the clay improved the modulus and ultimate stress and strain.

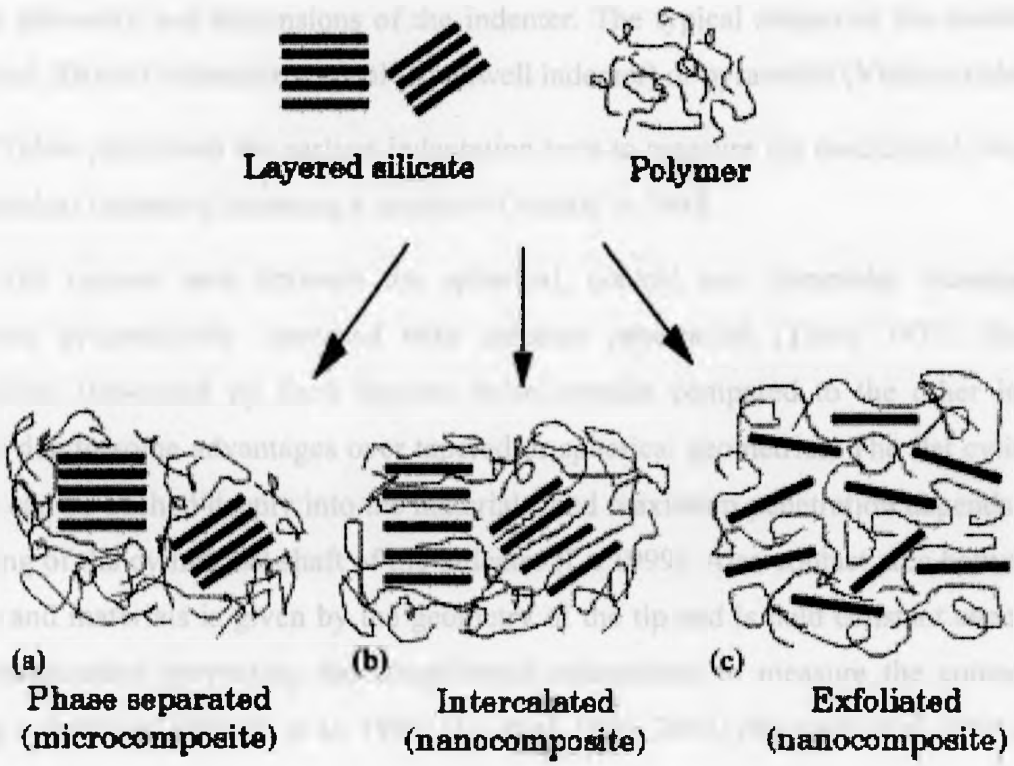

Figure 2.5: Three types of polymer clay nanocomposite structures (Alexandre et al. 2000).

2.4 Indentation

Examination of the mechanical properties of PDMS and clay-filled nanocomposites is necessary for their successful application. Lately indentation has become a significant method to probe the mechanical properties of the materials comprising elastic modulus, yield strength, fracture toughness and fatigue.

Indentation technique consists of a rigid indenter pushed into the materials defined by the geometry and dimensions of the indenter. The typical shapes of the indenter are spherical (Brinell indenter), conical (Rockwell indenter) or pyramidal (Vickers indenter).

Tabor performed the earliest indentation tests to measure the mechanical properties by spherical indenters indenting a number of metals in 1948.

The contact area between the spherical, conical and pyramidal indenters and materials progressively increased with indenter penetration (Tabor 1970). Recently cylindrical flat-ended tip have become more popular compared to the other indenter shapes due to some advantages over tapered or spherical geometries. The flat cylindrical punch can be pushed deeply into the materials, and maximum penetration depends on the buckling of the cylindrical shaft of the indenter (Lu 1999). Also contact area between flat punch and materials is given by the geometry of the tip and is held constant even in the deep penetration preventing the complicated calculations to measure the contact area during indentation (Wright et al. 1992) (Lu et al. 1999, 2002) (Riccardi et al. 2004) (Choi et al. 2008).

An important drawback in the case of the flat cylindrical indenter is that the local nonlinearities of the material and the geometry occur near the sharp corners of the indenter that can change the force-depth response (Pavliotis et al. 2002).

2.4.1 Indentation of the rubber-like materials

Indentation of the bulk of linear elastic materials has been extensively studied. The problem of the elastic contact between two spherical surfaces with different radii and elastic constants was originally considered by Hertz (Oliver et al. 1992). Sneddon used

the Hankel transforms to derive the load-displacement relation for an arbitrary shaped axisymmetric punch (Sneddon 1945).

Up to now most work in the literature only focused on the indentation of an elastic half space and multilayer structure. Little has been done in the case of the indentation of the bulk and thin film of the rubber-like material.

Lim and Chaudhri (2004) carried out a number of indentation tests on several elastic solids consisting of a natural rubber compound, neoprene and three different compositions of polydimethylsiloxane (Sylgard 184). In their study, the tungsten carbide cones with three different angles were used as indenters. They showed that the indentation load-displacement behavior of all the elastic solids is well fitted by the Sneddon's theory (1965) for frictionless indentations.

Carrillo et al. (2005) examined the nanoindentation of the PDMS (Sylgard 184) with different degrees of crosslinking to characterize the elastic moduli. They reported that elastic moduli diminish (2.04 to 0.42 MPa) with decreasing of the amount of cross-linker.

Lim and Chaudhri (2006) studied the pyramidal indentation of several blocks of elastic solids including a neoprene, rubber and PDMS (Sylgard 184) with three different amounts of cross-linker (2.5%, 5% and 10% by volume). They proposed that the experimental data have the significant discrepancies with predictions of the Sneddon's theory.

Giannakopoulos and Triantafyllou (2007) carried out the indentation test with spherical indenter on the incompressible rubber material accompanied by finite element analysis. Furthermore they found a set of analytic expressions that relate the indentation depth with the applied vertical force, the contact radius and the radius of the sphere proved by experimental data. Also uniaxial tensile tests were also performed and it was found that the initial elastic modulus correlates well with the indentation response. The experiments suggest stiffer indentation response than that predicted by linear elasticity.

The quasi-static indentation of a rubber-like material was studied by Giannakopoulos and Panagiotopoulos (2009). The sharp rigid cones were used during

indentation tests. They showed the elastic modulus at infinitesimal strains correlates well with the indentation response.

2.4.2 Indentation-induced delamination of a coating from a substrate

Interfacial adhesion is defined as a state that two bodies are held together by interfacial forces. The delamination of the thin films adhering to the substrate is a major issue for micro and nanoelectronics and optoelectronic devices. Interfacial failure and surface damage may affect the performance of coating system and limit the reliability of a device. Thus reliable characterization of interfacial strength is critical to the improvement of adhesion properties and to control of quality in multilayer structures and devices (Geng et al 2007). It is difficult to perform conventional characterization methods, such as tensile testing to measure the interfacial strength between a thin film and substrate. Micro and nanoindentation technique have attracted much attention to compute the mechanical properties of the thin film including hardness, elastic modulus and yield strength. Indentation methods have also been applied to calculate the adhesion strength between films and substrates. The interfacial delamination is occurred by pushing a rigid indenter into the coating. There are some papers which deal with this issue to examine interfacial adhesion. The most relevant papers are discussed below.

Chiang et al. (1982) evaluated the interfacial strength between a surface coating and a substrate using a Vickers indenter. They stated that indentation deformation compressed the coating leads to the delamination of the coating from the substrate.

Mattewson (1986) proposed that the radial displacement caused by the indentation produces a shear stress at the interface which causes the initiation and propagation of cracks.

Ritter et al. (1989) reported that indentation-induced debonding of the coating occurs in three conditions in the case of the Vickers indenter as shown in the.

1- Type 1 that the deformation is linear elastic until debonding occurs in the thin film underneath the indenter.

2- Type 2 that the deformation is plastic until debonding occurs in the thin film underneath the indenter.

3- Type 3 that the debonding occurs when the indenter pierces into the rigid substrate.

Also they stated that the failure condition depends on the properties of the coating, coating thickness, adhesive strength and the indenter sharpness. For example in the case of the thin well-adhered coatings with Vickers indenter the type 3 would be occurred (Ritter et al. 1989).

Based on the shear lag model, Dehm et al. (1997) suggested an approximate elastic model for estimation of the interfacial strength of a metal film on a ceramic substrate using a conical indenter. The Dehm's model was developed by Lu and Shinozaki (2002) to the indentation of the polymeric thin films on various substrates using a flat-ended cylindrical indenter. Geng et al (2007) evaluated the indentation-induced delamination of the polymeric coatings quantitatively by Vickers indentation.

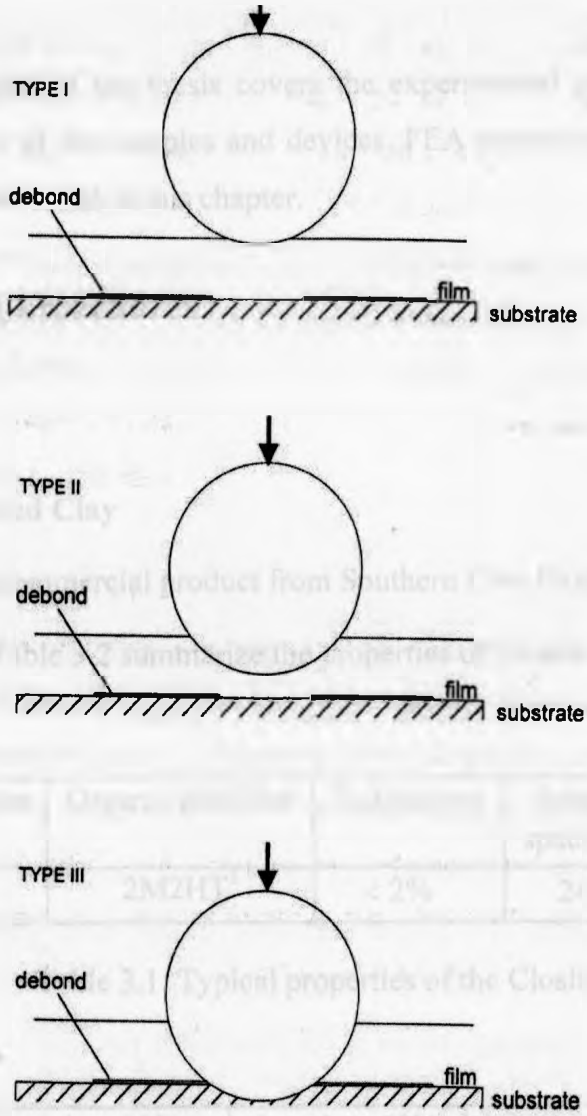

Figure 2-6: Schematic illustration of the of the three types of the interface debonding 1) Debonding under elastic deformation in thin film 2) debonding under plastic deformation in the thin film 3) Debonding occurs when the indenter pierces in to the substrate (Lu 1999).

Chapter 3. ANALYSIS AND METHODOLOGY

The third chapter of the thesis covers the experimental methods and procedures including preparation of the samples and devices. FEA procedures, mesh and boundary conditions are also discussed in this chapter.

3.1 Experimental Procedures

3.1.1 Materials

- Organically Modified Clay

Closite 20A, a commercial product from Southern Clay Product was used.

Table 3.1 and Table 3.2 summarize the properties of Closite 20A.

Treatment/Properties	Organic Modifier	% Moisture	Inter layer spacing d_{001}	Density g/cc
Closite 20A	2M2HT[1]	< 2%	24.2 A	1.77

Table 3.1: Typical properties of the Closite 20A.

less than 10%	less than 50%	less than 90%
2 μ	6 μ	13 μ

Table 3.2: Typical dry particle sizes of the Closite 20A.

[1] 2M2HT: Dimethyl, dehydrogenated tallow, quaternary ammonium

- Polymer

Polydimethylsiloxane (PDMS) purchased from United Chemicals Inc. PDMS was dried at 60°C in the oven for one day to remove ethanol and water. Ethanol and water was removed to prevent the reaction of OH group in these molecules with TEOS and catalyst (Moloodi 2009).

PDMS network were synthesized using TEOS and tin(II)-ethylhexanoate as cross-linker and catalyst respectively. Both cross-linker and catalyst were purchased from Sigma-Aldrich.

3.1.2 Apparatus

- Mixing components, molding and curing

PDMS networks were fabricated by mixing various degrees of cross-linker (R2.2-R11), required amounts of PDMS shown in Table 3.3, tin(II)-ethylhexanoate and TEOS. The mixtures were stirred using mechanical mixer for 4 minutes.

Clay-PDMS-R11 nanocomposites were synthesized by mixing the required proportional of the PDMS and clay given in Table 3.4. The mechanical stirrer speed was increased incrementally from 500 to 3000 *rpm* during five minutes, and sonication was utilized for 30 *min* for further homogenization. Sonication was carried out while the mixture was kept in a container filled with ice to avoid agglomeration of the particles due to heat produced during the process. In the next step tin(II)-ethylhexanoate and TEOS were added by a syringe. The mechanical stirring of the solution was performed for 4 minutes at 3000 *rpm*.

The mixtures were poured in to glass moulds made of soda lime glass microscopic slides to prepare thin film samples for both tensile and indentation tests; the moulds had the dimensions of 2.5 *cm* x 7.5 *cm* and 2.5 *cm* x 2.5 *cm*. Use of the glass slide facilitates obtaining a smooth surface for indentation and tensile test.

A plastic cylinder of 2 *cm* diameter and 4 *cm* height was employed as a mould for bulk PDMS and nanocomposites samples.

The mould containing the mixtures was placed in a sealed chamber, which was evacuated with a vacuum pump. This allowed for any bubbles in the mixture to escape from it. Samples were cured at room temperature for two days.

In order to prepare samples for tensile test, a scalper was used to cut the samples to I shaped beams which were removed from the glass moulds. Polymer and nanocomposites blocks were removed from the plastic cylinder.

	PDMS (gr)	TEOS (gr)	Tin(II)-ethylhexanoate (gr)
$R_{2.2}$	1	0.036	0.005
R_5	1	0.01724	0.005
R_{11}	1	0.00759	0.005

Table 3.3: PDMS network made of 23 kg/mol chains with different amount of cross-linker

	PDMS (gr)	TEOS (gr)	Tin(II)-ethylhexanoate (gr)	Clay (gr)
1% Clay	0.99	0.03564	0.005	0.01
3% Clay	0.97	0.03492	0.005	0.03
5% Clay	0.95	0.0342	0.005	0.05
7% Clay	0.93	0.03348	0.005	0.07

Table 3.4: Relative amounts of reactants used in the synthesis of PDMS-clay nanocomposites

- Tensile test

Uniaxial tensile tests were carried out to examine the stress-strain behaviours and define the material properties of the PDMS and PDMS-clay nanocomposites in finite element analysis. Tests were performed on a standard screw driven Instron shown in Figure 3-1 at a certain cross-head speed 1 $mm.min^{-1}$. A load cell with maximum capacity 600 Kg was used to measure the force. The Instron machine was connected to a PC to calibrate the load cell, adjust the cross-head speed and record the load and displacement data. All tests were done at room temperature.

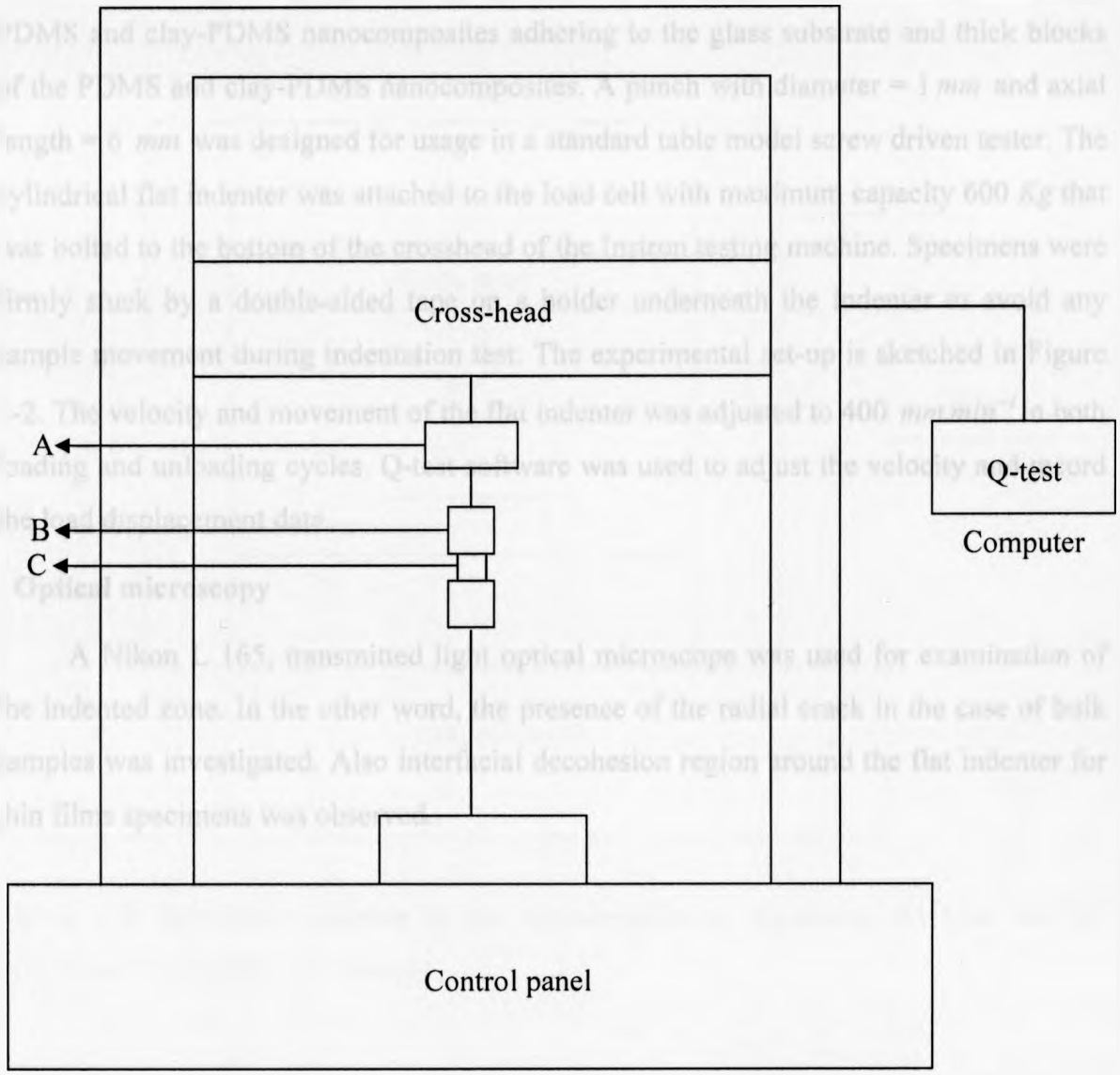

Figure 3-1: Schematic diagram of the uniaxial tensile apparatus. A) load cell B) Grips C) Sample.

- Indentation test

Indentation tests were carried out on two types of specimens: thin films of the PDMS and clay-PDMS nanocomposites adhering to the glass substrate and thick blocks of the PDMS and clay-PDMS nanocomposites. A punch with diameter = 1 *mm* and axial length = 6 *mm* was designed for usage in a standard table model screw driven tester. The cylindrical flat indenter was attached to the load cell with maximum capacity 600 *Kg* that was bolted to the bottom of the crosshead of the Instron testing machine. Specimens were firmly stuck by a double-sided tape on a holder underneath the indenter to avoid any sample movement during indentation test. The experimental set-up is sketched in Figure 3-2. The velocity and movement of the flat indenter was adjusted to 400 $mm.min^{-1}$ in both loading and unloading cycles. Q-test software was used to adjust the velocity and record the load displacement data.

- Optical microscopy

A Nikon L 165, transmitted light optical microscope was used for examination of the indented zone. In the other word, the presence of the radial crack in the case of bulk samples was investigated. Also interfacial decohesion region around the flat indenter for thin films specimens was observed.

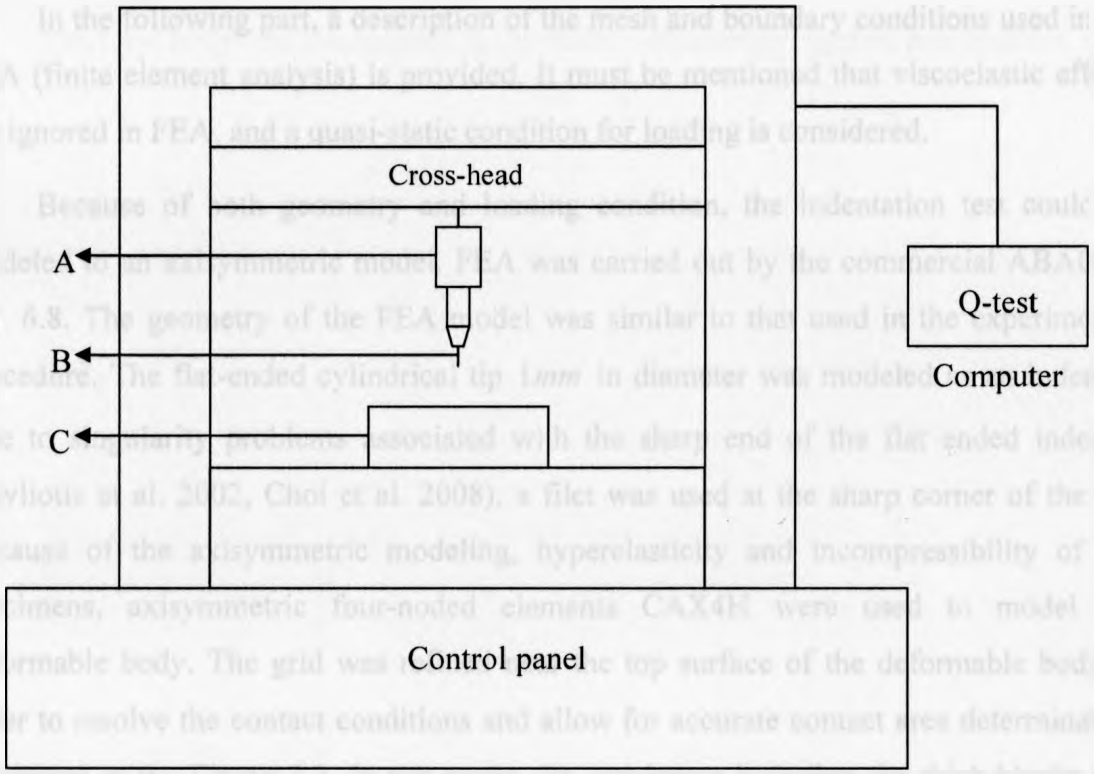

Figure 3-2: Schematic diagram of the macroindentation apparatus. A) load cell B) cylindrical flat indenter C) Sample.

3.2 Finite element procedures

3.2.1 The FEA mesh and boundary conditions

In the following part, a description of the mesh and boundary conditions used in the FEA (finite element analysis) is provided. It must be mentioned that viscoelastic effects are ignored in FEA, and a quasi-static condition for loading is considered.

Because of both geometry and loading condition, the indentation test could be modeled to an axisymmetric model. FEA was carried out by the commercial ABAQUS ver. 6.8. The geometry of the FEA model was similar to that used in the experimental procedure. The flat-ended cylindrical tip $1mm$ in diameter was modeled as an indenter. Due to singularity problems associated with the sharp end of the flat ended indenter (Pavliotis et al. 2002, Choi et al. 2008), a filet was used at the sharp corner of the tip. Because of the axisymmetric modeling, hyperelasticity and incompressibility of the specimens, axisymmetric four-noded elements CAX4H were used to model the deformable body. The grid was refined near the top surface of the deformable body in order to resolve the contact conditions and allow for accurate contact area determination illustrated in the Figure 3.3. In this study, the specimens including the thick blocks and thin films of PDMS and clay-PDMS nanocomposites were treated as a deformable body and the indenter was considered to be perfectly rigid (cannot deform but can translate or rotate), because the elastic modulus of the indenter is almost 35000 times greater than the deformable body. The reference node is the point chosen on the surface of the rigid body and all translation and rotation apply on it. Contact between the rigid indenter surface and the specimen was modeled using rigid surface contact elements.

Friction between the indenter surface and the specimen was defined through the "interaction" between contact pairs. In the present study, the friction coefficient was set to zero.

Proper boundary conditions were enforced at the symmetric boundaries in order to model the axisymmetric problem correctly explained as follows:

The nodes along the central axis of the cylinder were constrained to move only along the *Z*-axis.

The nodes at the bottom of the deformable body were constrained in the *Z* and *R*-axes (due to the rigidity of the substrate)

The rigid body was constrained in the radial direction and against any rotation.

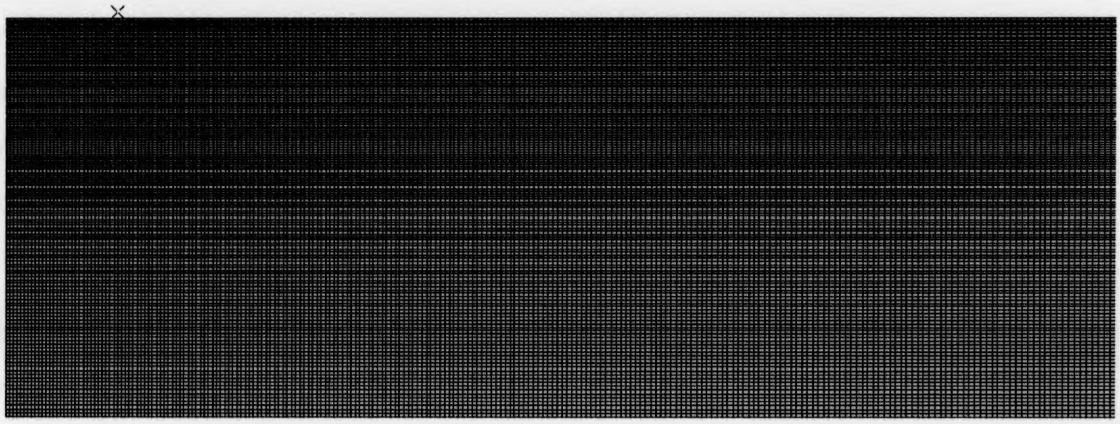

Figure 3.3: Finite element mesh used in the modeling of the indentation of the PDMS and nanocomposites of clay-PDMS.

3.2.2 Materials properties used in the FEA

In the modeling, it was assumed that the PDMS and clay-filled PDMS nanocomposites were isotropic, homogeneous, incompressible materials ($\upsilon = 0.5$) (Gent 1954, Livermore et al. 2005, Carrillo et al 2005). In addition, it was further assumed that viscous and thermal effects are negligible.

In the case of the hyperelastic materials, Abaqus uses a strain energy potential (W), rather than a Young's modulus and Poisson's ratio, to relate stresses to strains in hyperelastic materials. Several different strain energy potentials are available: a polynomial model, the Ogden model, the Arruda-Boyce model, the Marlow model, and the Van der Waals model. Simpler forms of the polynomial model are also available, including the Mooney-Rivlin, neo-Hookean, reduced polynomial, and Yeoh models.

In this study, to define hyperelastic materials, the nominal stress-strain data required as input into the Abaqus model acquired from the uniaxial tensile testing on the relevant materials as shown in the Figure 3-4.

All curves were well fitted to the Neo-Hookean or reduced polynomial strain energy model with parameter 1 given by Eq. (2.16). All fitted curves are shown in Figure 3.6-Figure 3.12. The constitutive parameters obtained used in FEA model are summarized in the Table 3-5.

To simulate the indentation process, a downward displacement was imposed on the indenter. This caused the indenter to push into the surface of the material. Therefore, a displacement with negative value in Z-direction was applied to the reference point of the indenter in the downward direction. Subsequent unloading was done by adjusting displacement in the Z-direction to zero value.

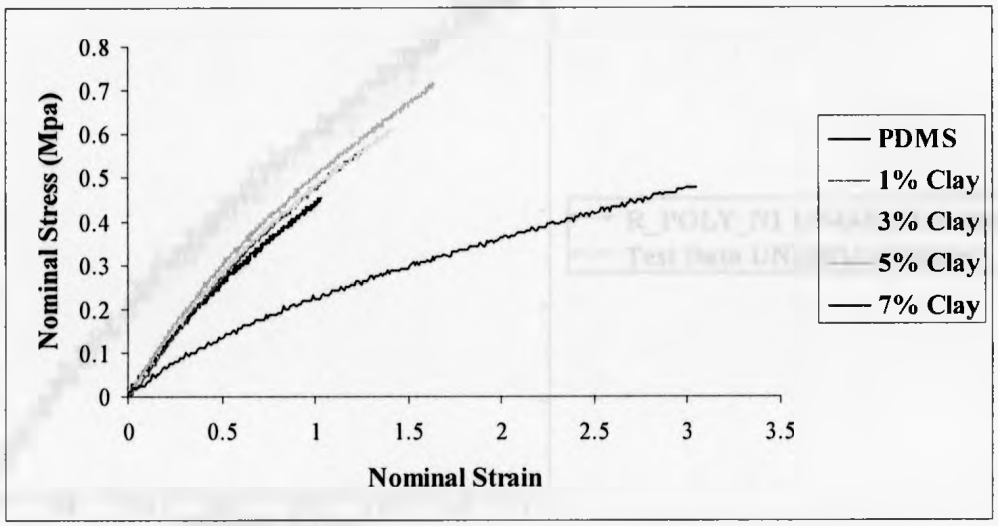

Figure 3-4: Stress-Strain curves of the PDMS and Clay-filled PDMS nanocomposites obtained from uniaxial tensile test.

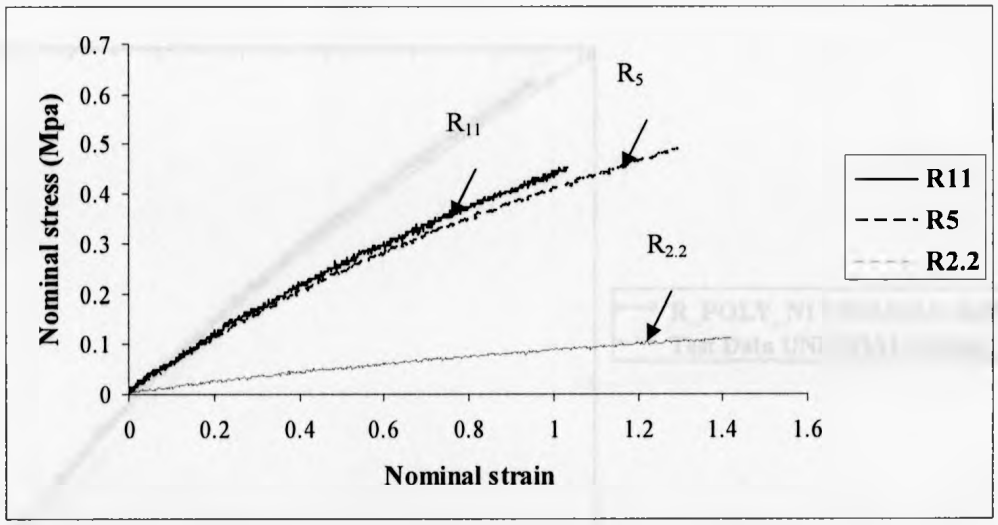

Figure 3.5: Nominal stress-strain curves of the PDMS with different amount of cross-linker obtained from uniaxial compression test.

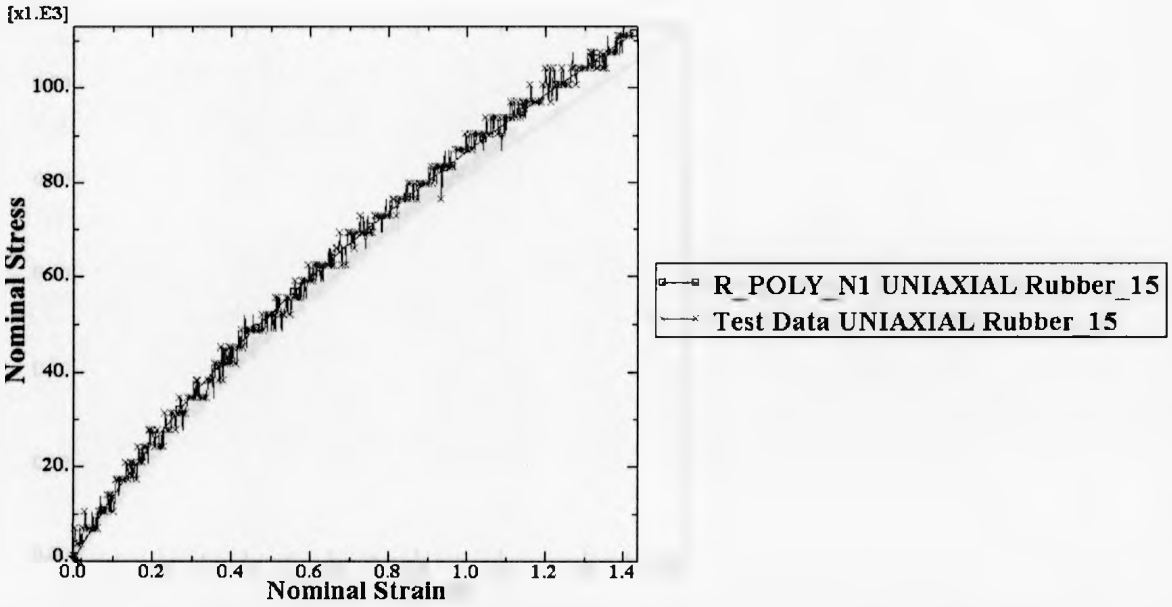

Figure 3.6: Uniaxial tensile stress-strain curve (red) is fitted to Neo-Hookean curve (blue) to define material properties of PDMS-$R_{2.2}$.

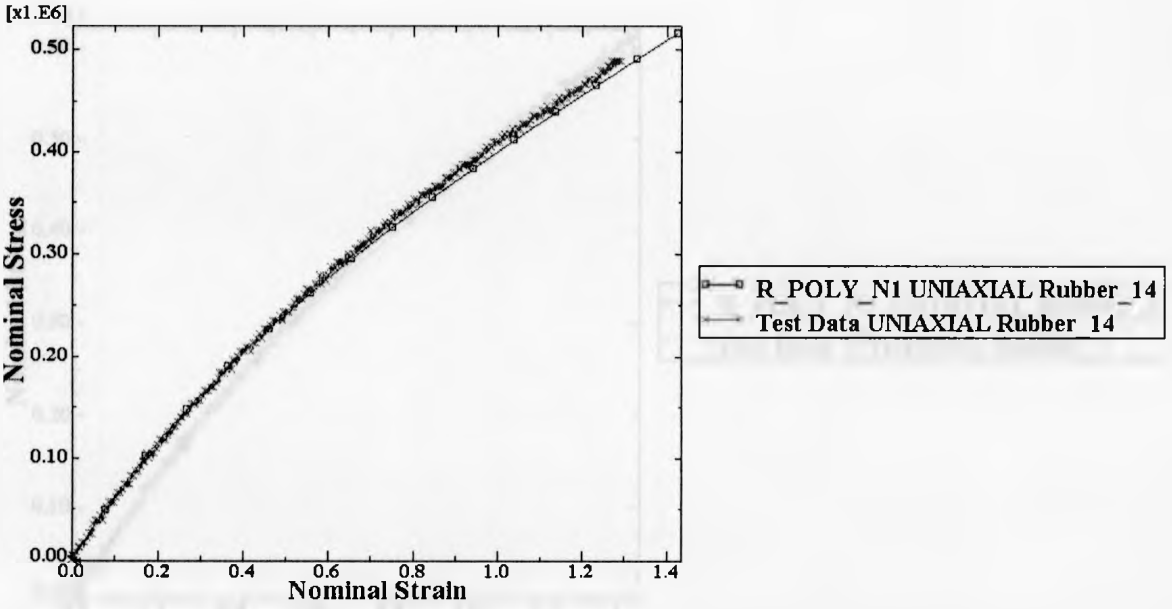

Figure 3.7: Uniaxial tensile stress-strain curve (red) is fitted to Neo-Hookean curve (blue) to define material properties of PDMS-R_5.

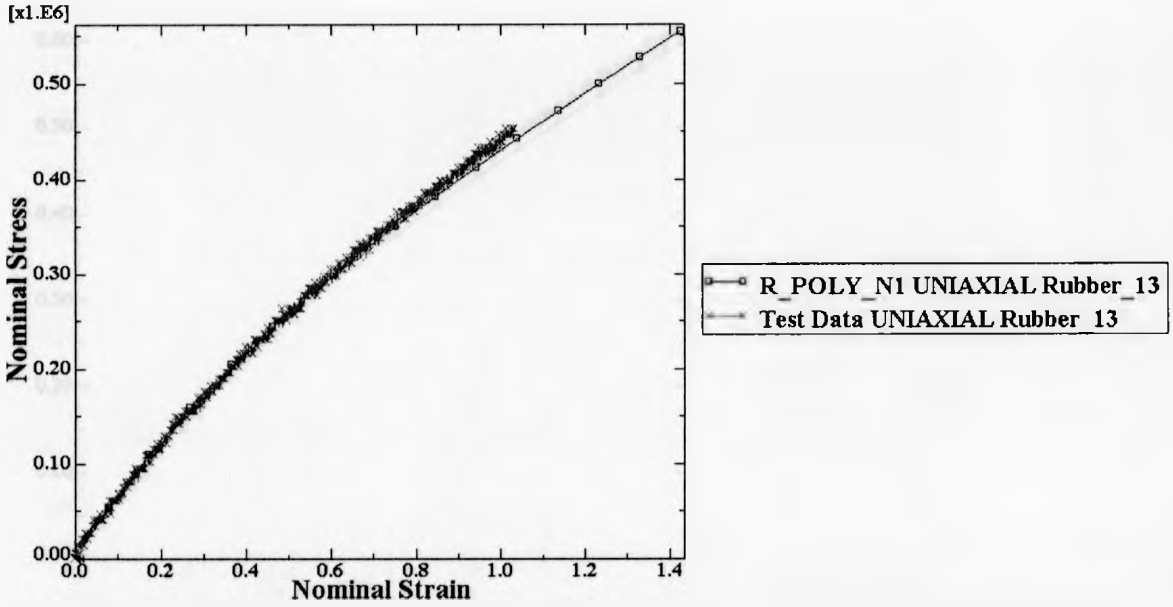

Figure 3.8: Uniaxial tensile stress-strain curve (red) is fitted to Neo-Hookean curve (blue) to define material properties of PDMS-R_{11}

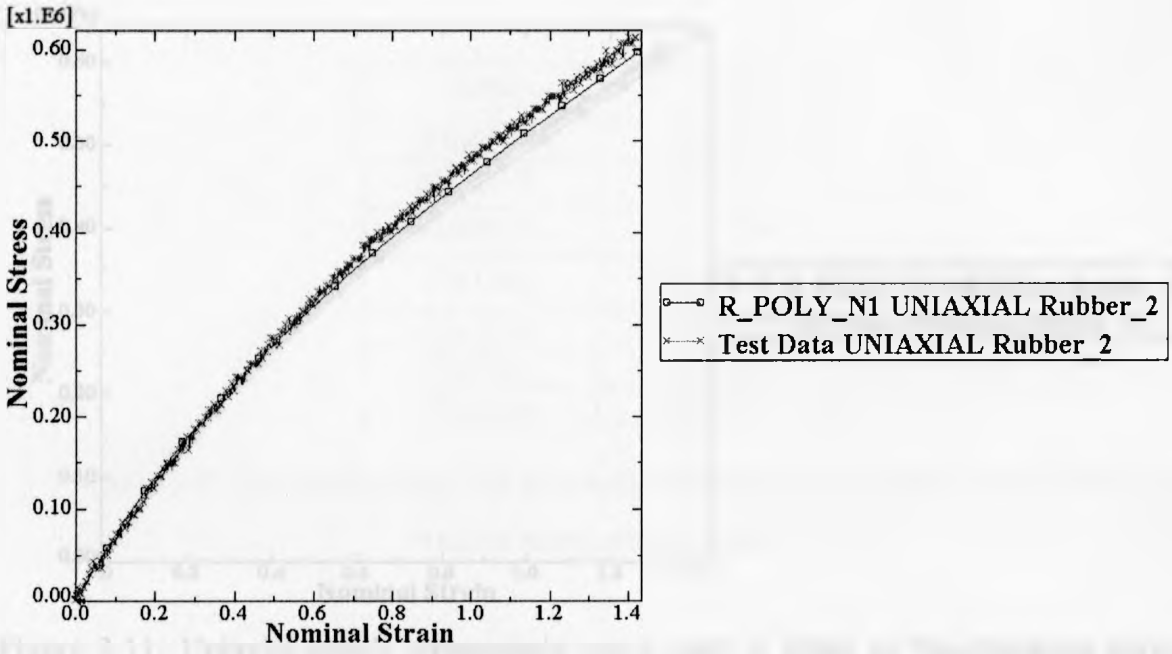

Figure 3.9: Uniaxial tensile stress-strain curve (red) is fitted to Neo-Hookean curve (blue) to define material properties of 1% clay-PDMS nanocomposite.

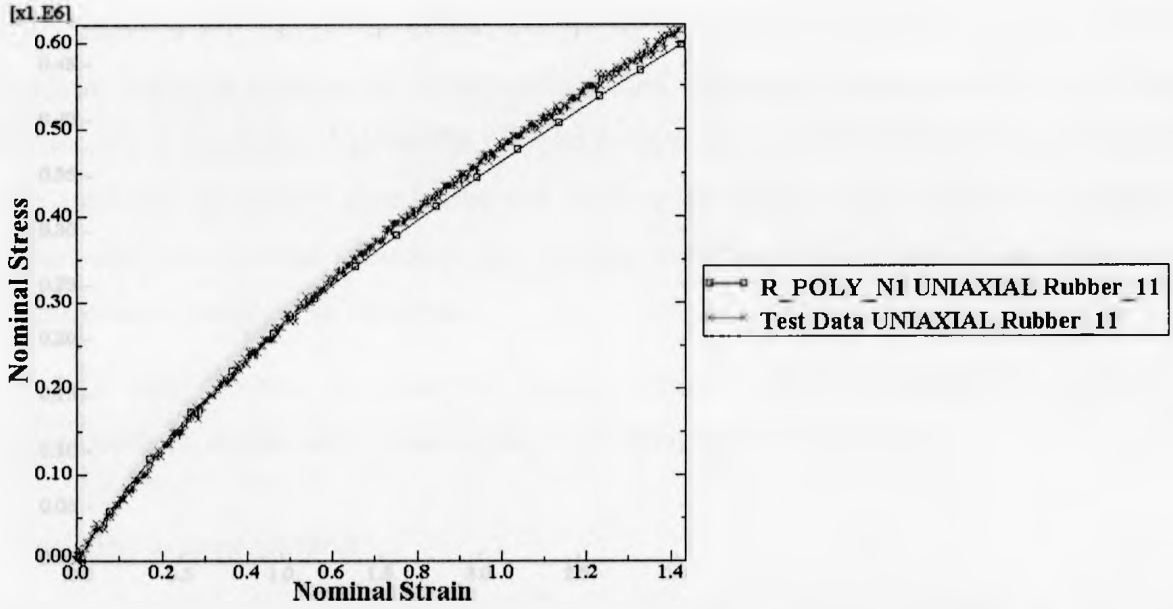

Figure 3.10: Uniaxial tensile stress-strain curve (red) is fitted to Neo-Hookean curve (blue) to define material properties of 3% clay-PDMS nanocomposite.

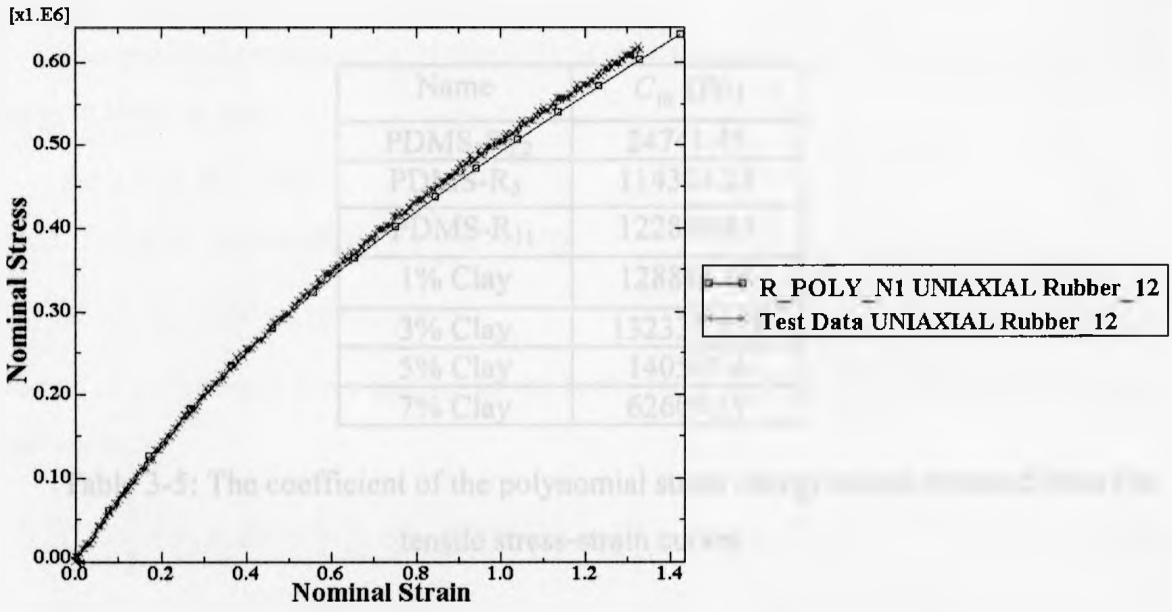

Figure 3.11: Uniaxial tensile stress-strain curve (red) is fitted to Neo-Hookean curve (blue) to define material properties of 5% clay-PDMS nanocomposite.

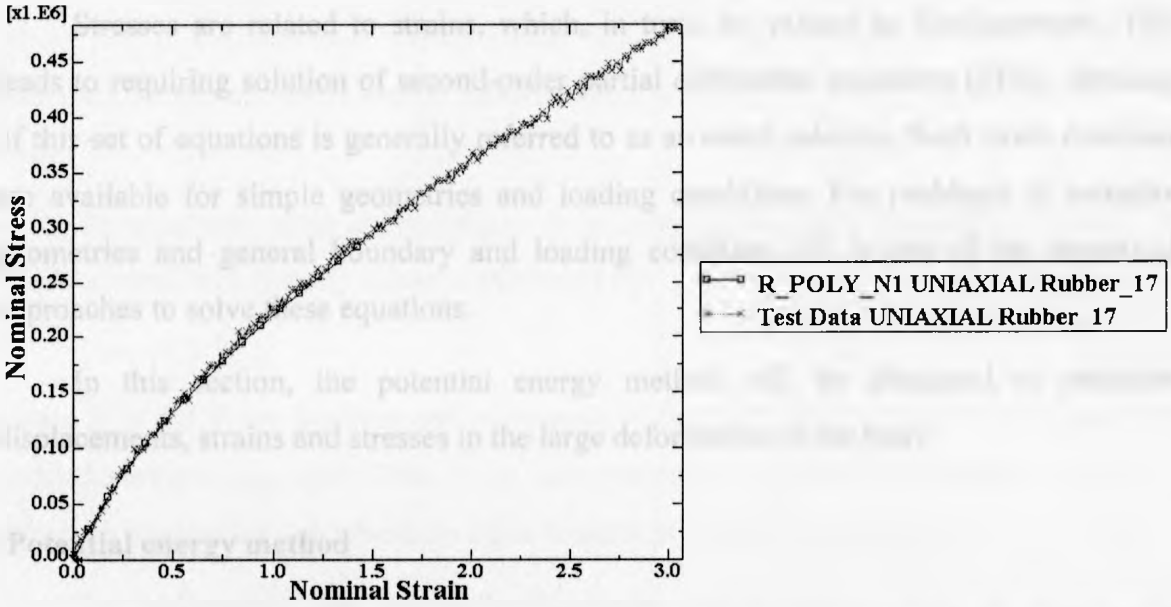

Figure 3.12: Uniaxial tensile stress-strain curve (red) is fitted to Neo-Hookean curve (blue) to define material properties of 7% clay-PDMS nanocomposite.

Name	C_{10} (Pa)
PDMS-$R_{2\,2}$	24741.45
PDMS-R_5	114304.28
PDMS-R_{11}	122860.84
1% Clay	128883.66
3% Clay	132339.823
5% Clay	140567.4
7% Clay	62609.19

Table 3-5: The coefficient of the polynomial strain energy model obtained from the tensile stress-strain curves

3.2.3- Calculation of the large deformation by Abaqus

Stresses are related to strains, which, in turn, are related to displacements. This leads to requiring solution of second-order partial differential equations (PDE). Solution of this set of equations is generally referred to as an exact solution. Such exact solutions are available for simple geometries and loading conditions. For problems of complex geometries and general boundary and loading condition, FE is one of the numerical approaches to solve these equations.

In this section, the potential energy method will be discussed to calculate displacements, strains and stresses in the large deformation of the body.

-Potential energy method

Potential energy is the energy stored in a body or in a system due to its position in a force field. The total potential energy (π) of an elastic body is defined as the sum of total strain energy (U) and the work of potential (W).

$$\pi = U + W \tag{3.1}$$

The equilibrium condition of the body is defined while the change of total potential energy is equal to zero.

$$\delta\pi = 0 \Rightarrow \delta U = \delta W \tag{3.2}$$

The work of potential (W) is given by:

$$W = -\int u.f.dV \Rightarrow \delta W = f\delta u \tag{3.3}$$

Where f is the external force applied to the body. Strain energy (U) of the elastic body is obtained by:

$$U = \frac{1}{2}\int \sigma_{ij}\varepsilon_{ij}dV = \frac{1}{2}\int <\sigma>\{\varepsilon\}dV \tag{3.4}$$

Hook's law yields Eq. (3.6)

$$<\sigma> = <\varepsilon>[D(u)] \tag{3.5}$$

$$U = \frac{1}{2}\int < \varepsilon > [D(u)]\{\varepsilon\}dV \Rightarrow \delta U = \int < \varepsilon > [D(u)]\{\varepsilon\}dV \tag{3.6}$$

where *[D]* is stiffness coefficients matrix related to the mechanical properties of the materials. In the nonlinear elastic materials *[D]* is a function of the displacement of the body.

To calculate large deformation, it is required to write Eq.(3.6) in terms of displacement field in every element expressed by:

$$u = < N > \{u_n\} \tag{3.7}$$

where N is the shape function and u_n degrees of freedom (DOF). In this modeling, four nodded element was used. Due to the axisymmetric condition, displacement in the θ direction is equal zero. So there are eight degrees of freedom per element.

Eq.(3.6) could be expresses in the following form:

$$\delta U = < \delta u_n > (\int \{N,\}.[D(u)].< N >).\{u_n\} = < \delta u_n > .[K].\{u_n\} \tag{3.8}$$

[K] is stiffness matrix. Eqs.(3.2), (3.3) and (3.8) yield:

$$[K][u_n] = [F] \tag{3.9}$$

Abaqus uses Eq. (3.9) to calculate displacement in every element. Also strains will be computed using green strain tensor.

Chapter 4. DEEP PENETRATION INDENTATION OF THE BULK PDMS AND CLAY-FILLED PDMS NANOCOMPSITES

4.1 Deep penetration indentation test

A flat cylindrical indenter was loaded on to the specimens at the predetermined displacement rate (loading cycle), and then the indenter was unloaded to zero gradually (unloading cycle). The indenter load versus indenter displacement data were recorded digitally.

Figure 4.1 and Figure 4.2 illustrate the indentation load-displacement curves of the bulk PDMS with various degrees of cross-linker and bulk clay-filled PDMS-R11 nanocomposites containing 1, 3, 5 and 7% clay respectively.

Due to the cylindrical geometry of the indenter, the contact area does not change; therefore the stress or indentation pressure (P) could be calculated by dividing the indenter load (F) by indenter cross section (Wright et al. 1992) (Lu et al. 1999, 2002).

$$P = \frac{F}{\pi a^2} \tag{4.1}$$

where "a" is the radius of the indenter.

The point where load drop or sudden displacement excursion was observed is referred to critical indentation load. The load drop is a result of the relaxation of the stress field as the crack runs (Lu 1999). The magnitudes of the critical indentation debonding depth (H_f), load (F_c) and stress (P_c) for PDMS with various amounts of cross-linker and clay-PDMS-R11 containing 1, 3, 5 and %7 clay are given in Table 4.1 and Table 4.2.

	Critical Indentation Debonding Depth $H_f\ (mm)$	Critical Indentation Debonding Load $F_c\ (N)$	Critical Indentation Debonding Stress $P_c\ (Mpa)$
PDMS-R_{11}	1.59	2.23	2.85
1% Clay	1.59	2.58	3.29
3% Clay	1.82	3.48	4.43
5% Clay	1.83	3.88	4.94
7% Clay	1.61	2.88	3.67

Table 4.1: Critical indentation debonding depth, load and stress obtained from indentation curves for bulk clay-PDMS-R_{11} nanocomposites

	Critical Indentation Debonding Depth $H_f\ (mm)$	Critical Indentation Debonding Load $F_c\ (N)$	Critical Indentation Debonding Stress $P_c\ (MPa)$
PDMS-R_{22}	4.624	1.493	1.901
PDMS-R_5	3.447	5.175	6.59
PDMS-R_{11}	1.59	2.23	2.85

Table 4.2: Critical indentation debonding load, stress and depth obtained from indentation curves for bulk PDMS with different amount of cross-linker.

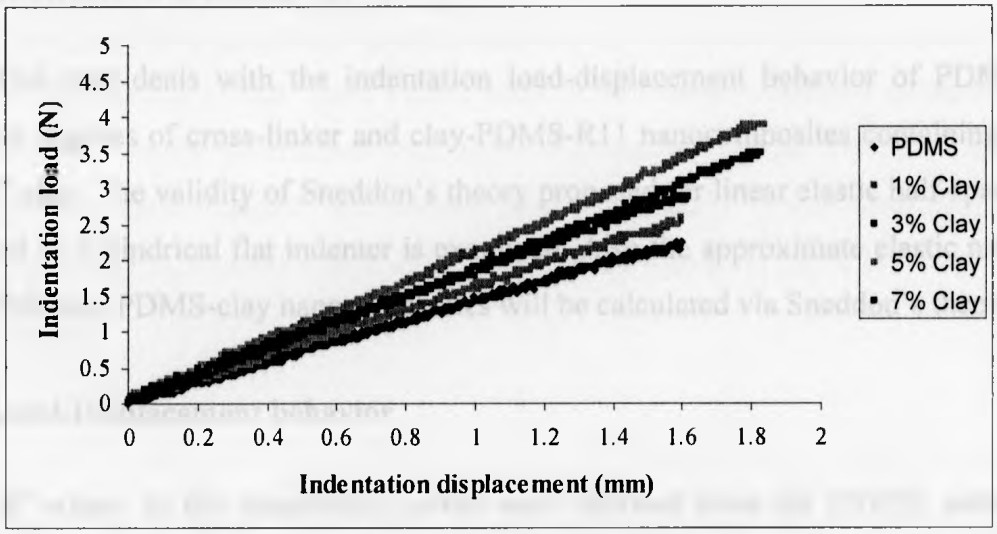

Figure 4.1: Load-displacement curves of bulk PDMS-R_{11} and clay-PDMS-R_{11} nanocomposites containing 1, 3, 5 and 7% clay obtained from indentation test.

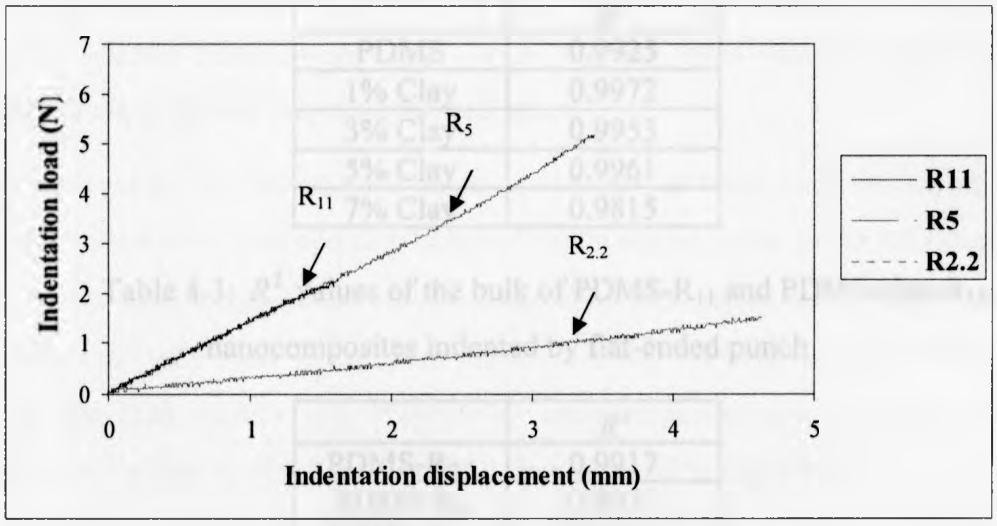

Figure 4.2: Load-displacement curves of bulk PDMS with different amount of the cross-linker obtained from indentation test.

4.2 Indentation loading curves

This part deals with the indentation load-displacement behavior of PDMS with different degrees of cross-linker and clay-PDMS-R11 nanocomposites containing 1, 3, 5 and %7 clay. The validity of Sneddon's theory proposed for linear elastic half-space body indented by cylindrical flat indenter is examined. Also the approximate elastic moduli of the PDMS and PDMS-clay nanocomposites will be calculated via Sneddon's theory.

4.2.1 Load-Displacement behavior

R^2 values[1] of the indentation curves were obtained from the EXCEL software to approve the linearity of the indentation load-displacement plots. These values were satisfactory close to unity indicating the linear behavior of the indentation plots. R^2 values are shown in Table 4.3 and Table 4.4.

	R^2
PDMS	0.9925
1% Clay	0.9972
3% Clay	0.9953
5% Clay	0.9961
7% Clay	0.9815

Table 4.3: R^2 values of the bulk of PDMS-R_{11} and PDMS-clay-R_{11} nanocomposites indented by flat-ended punch

	R^2
PDMS-R_{22}	0.9917
PDMS-R_5	0.9977
PDMS-R_{11}	0.9925

Table 4.4: R^2 values of the bulk PDMS with different amount of cross-linker indented by flat-ended punch

[1] R^2 is a measure in linear regression to assess the linearity of the expression.

4.2.2 Examination of the Load-Displacement behavior with Sneddon's theory

Sneddon (1964) proposed a general relationship between load and displacement for any punch indenting a thick linear elastic body in frictionless condition as shown in Eq. (4.2). Where F is the indentation load, h the displacement of the indenter, and m is a power law exponent related to the indenter geometry. Also α is a constant including the elastic modulus (E), Poisson's ratio of the specimen (υ) given in Eq.(4.3)

$$F = \alpha h^m \tag{4.2}$$

$$\alpha = \frac{2Ea}{1-\nu^2} \tag{4.3}$$

Lim and Chaudhri (2004) used Sneddon's load-displacement relationship and assessed its validity for rubbery materials. They performed macroindentation test on the three rubbery materials consisting of a natural rubber compound, neoprene and PDMS (Sylgard 184) by the tungsten carbide conical and spherical indenters. The indentation load versus indenter displacement of the curves was well fitted with the Sneddon's theory of a rigid cone and sphere indenting the half space.

In the case of the flat-ended cylindrical indenter, m takes unity indicating a linear relation for indentation load and displacement of the elastic body. In the previous part the linearity of the load-displacement curves obtained by indentation tests was proved by R^2 values that were very close to unity. In the other word, the behaviors of the indentation curves of the bulk PDMS and PDMS-clay nanocomposites are well fitted with the predictions of the theory of a flat cylindrical tip suggested by Sneddon.

Tip Geometry	m
Flat-ended cylindrical punch	1
spherical punch	1.5
Cone	2

Table 4.5: Theoretical values of m for three axisymmetric tip shapes.

4.2.3 Calculation of the elastic modulus by indentation test

It was clearly shown that the Sneddon's theory is applicable for PDMS and clay-filled PDMS nanocomposites. The relationship between the indenter load F and indenter displacement h proposed by Sneddon (1964) for flat cylindrical punch given in Eq.(4.4) is used to calculate the elastic modulus of PDMS and PDMS-clay nanocomposite.

$$F = \frac{2Ea}{1-\nu^2} h \tag{4.4}$$

Eqs (4.4) and (4.5) imply that the elastic modulus of the PDMS and nanocomposites can be simply approximated via calculation of the slope of the indentation load-displacement curve.

$$E = \frac{m\left(1-\nu^2\right)}{2a} \tag{4.5}$$

where m is the slope of the indentation load-displacement curve.

The Young's moduli of PDMS with various amounts of cross-linker and clay-PDMS-R11 nanocomposites are shown in Table 4.6 and Table 4.7

	E (MPa)
PDMS-R11	1.101
1% Clay	1.176
3% Clay	1.438
5% Clay	1.572
7% Clay	1.311

Table 4.6: Young's moduli of PDMS-R11 and clay-PDMS-R11 nanocomposites calculated by Sneddon's theory

	E (MPa)
PDMS-R2.2	0.230
PDMS-R5	1.039
PDMS-R11	1.101

Table 4.7: Young's moduli of PDMS with different amounts of the cross-linker calculated by Sneddon's theory

4.3 Indentation unloading curves

A flat-ended indenter was pushed into the thick PDMS and PDMS-clay nanocomposite blocks at the preselected displacement rate, and then at the certain depth before delamination occurred, the indenter load was decreased to zero at the same displacement rate as loading cycle.

Lim and Chaudhri (2004) reported a little hysteresis for the PDMS block (Sylgard 184) with different amount of cross-linker indented by tungsten carbide cone. Lim and Chaudhri (2006) also stated that the unloading curve for the PDMS block (Sylgard 184) indented by Vickers indenter closely overlaps its loading curves.

Hysteresis occurs when the unloading path of a load-displacement curve is different from the loading path. No hysteresis was observed in the case of PDMS with various amounts of cross-linker shown in Figure 4.3-Figure 4.5. Also loading curve overlaps exactly the unloading curve of the clay-PDMS-R11 nanocomposites up to 7% clay as plotted in Figure 4.6-Figure 4.8.

This behavior can be explained by capacity of the hyperelastic materials to recover from large deformation. Since these materials are stretched or compressed, after removing the load, they can return to the original state. In the other word, during unloading process the region being indented can retrieve to the primary condition.

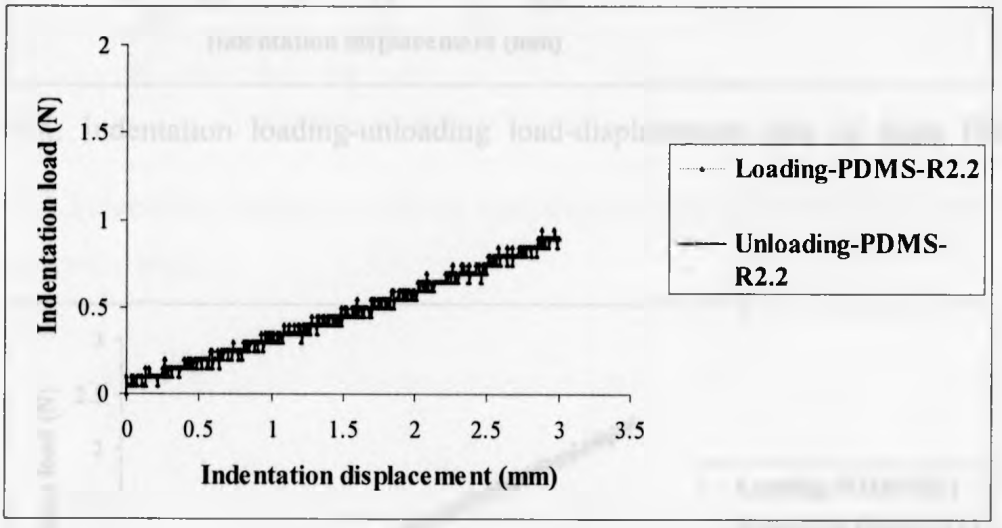

Figure 4.3: Indentation loading-unloading load-displacement plot of thick PDMS-$R_{2.2}$ block.

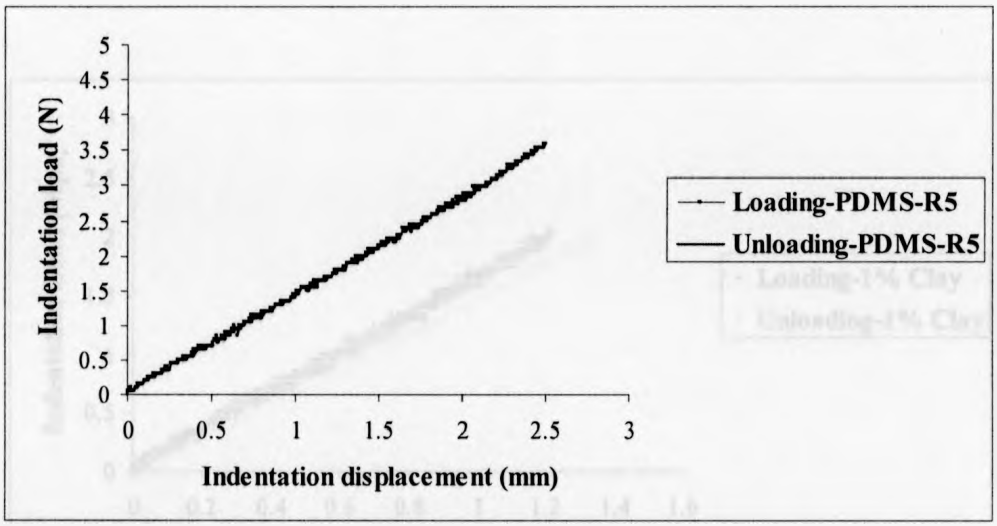

Figure 4.4: Indentation loading-unloading load-displacement plot of thick PDMS-R_5 block.

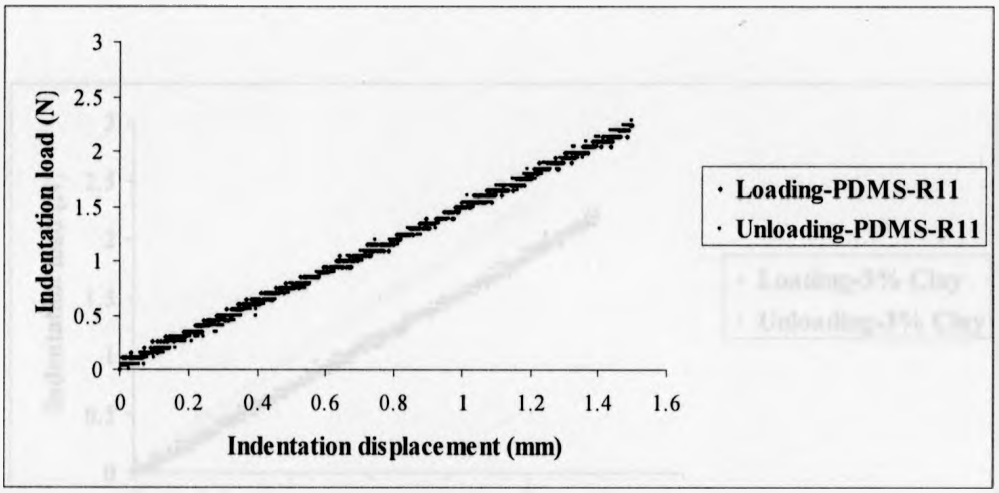

Figure 4.5: Indentation loading-unloading load-displacement plot of thick PDMS-R_{11} block.

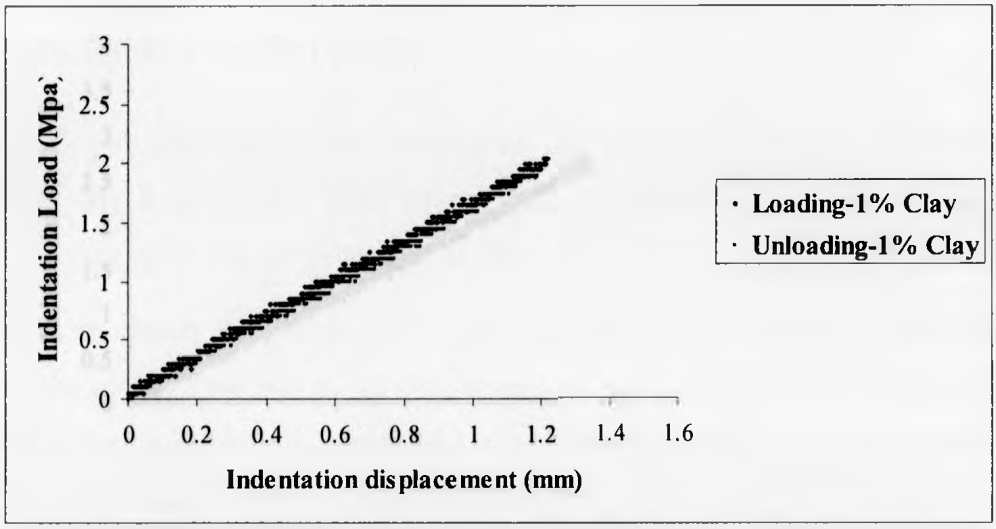

Figure 4.6: Indentation loading-unloading load-displacement plot of thick 1% clay-PDMS nanocomposites block.

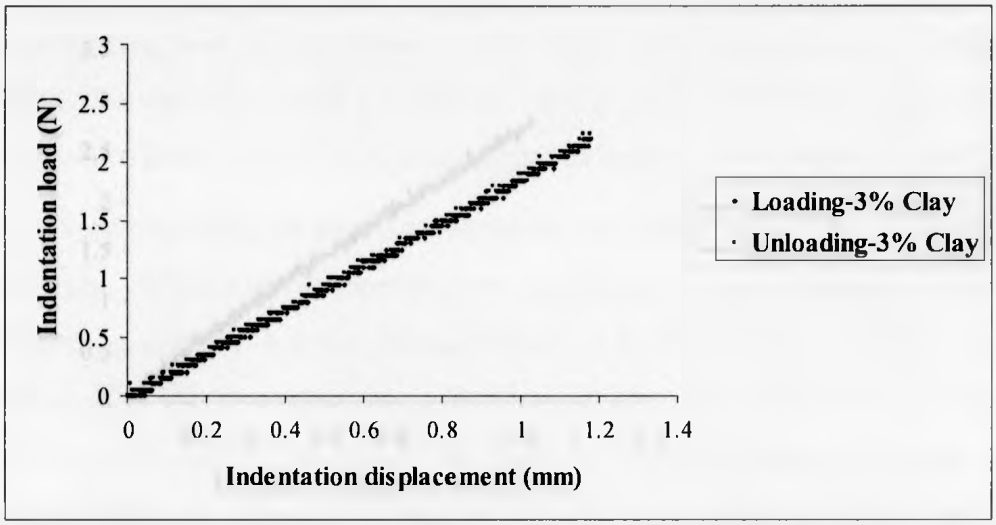

Figure 4.7: Indentation loading-unloading load-displacement plot of thick 3% clay-PDMS nanocomposites block.

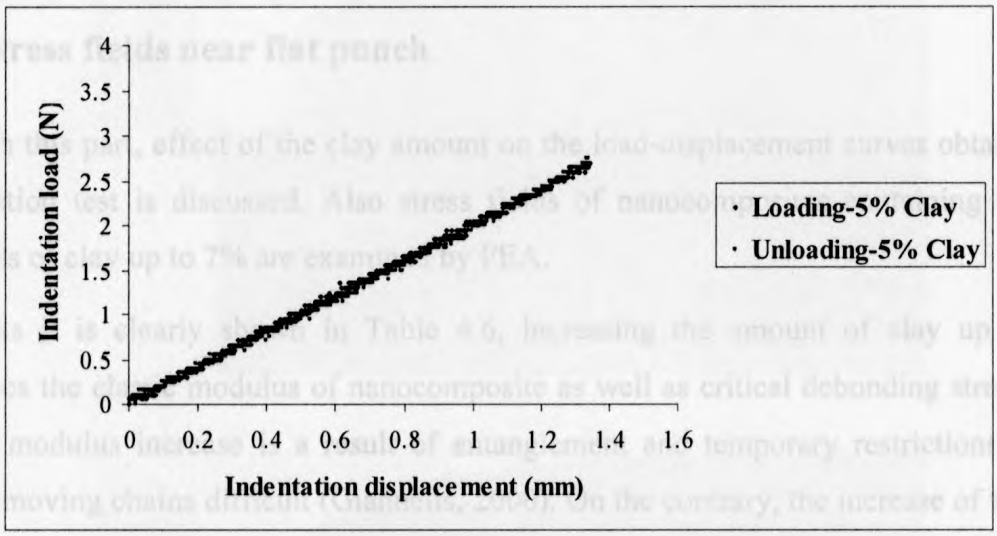

Figure 4.8: Indentation loading-unloading load-displacement plot of thick 5% clay-PDMS nanocomposites block.

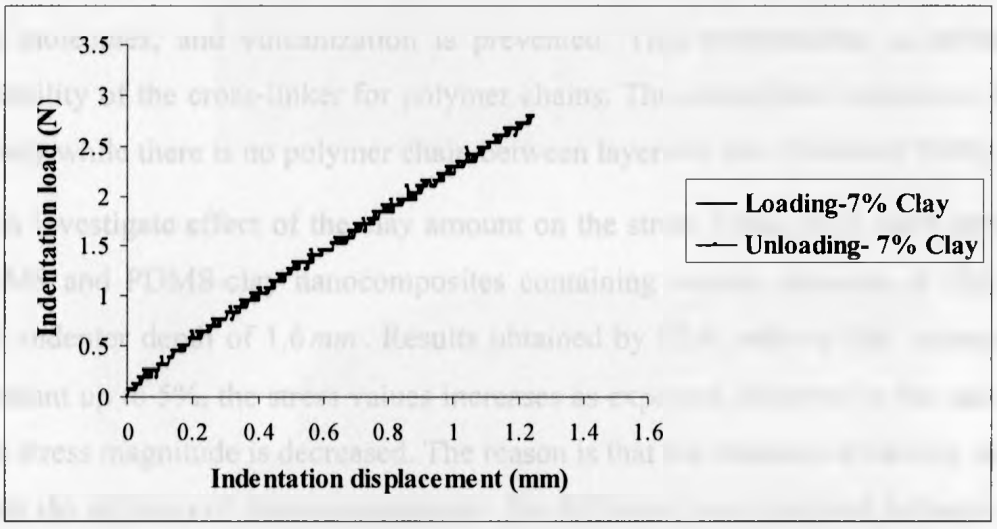

Figure 4.9: Indentation loading-unloading load-displacement plot of thick 7% clay-PDMS nanocomposites block.

4.4 Effect of clay amount on the indentation load-displacement curves and stress fields near flat punch

In this part, effect of the clay amount on the load-displacement curves obtained by indentation test is discussed. Also stress fields of nanocomposites containing various amounts of clay up to 7% are examined by FEA.

As it is clearly shown in Table 4.6, increasing the amount of clay up to 5% increases the elastic modulus of nanocomposite as well as critical debonding stress. The elastic modulus increase is a result of entanglement and temporary restrictions which makes moving chains difficult (Giannelis, 2000). On the contrary, the increase of the clay to 7% decreases the Young modulus of the nanocomposite. In the other word, PDMS nanocomposite with 7% clay behaves like a lightly cross-linked rubber. Moloodi et al. (2009) investigated the influence of the clay amount on the cross-linker function. They found that the presence of the clay particle in the system affects the function of cross-linking molecules, and vulcanization is prevented. This phenomenon is attributed to unavailability of the cross-linker for polymer chains. The cross-linker molecules enter to the gallery while there is no polymer chain between layers of clay (Moloodi 2009).

To investigate effect of the clay amount on the stress fields; FEA were carried out for PDMS and PDMS-clay nanocomposites containing various amounts of clay at the specific indenter depth of $1.6\,mm$. Results obtained by FEA indicate that increasing the clay amount up to 5%, the stress values increases as expected, however in the case of 7% clay the stress magnitude is decreased. The reason is that the increase of the clay up to 5% increases the stiffness of the nanocomposite. No difference was observed between PDMS and PDMS-clay nanocomposites in terms of contour shape. In Figure 4-10-Figure 4-12 the stress contour of the PDMS and 5%clay-PDMS nanocomposite is compared.

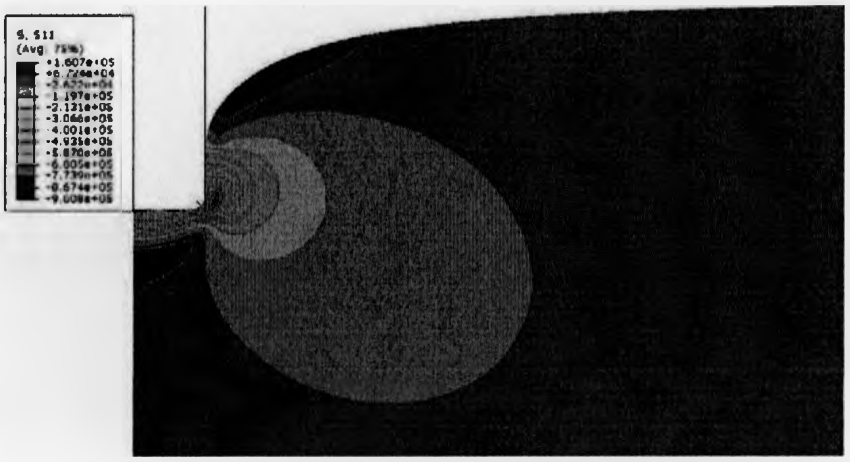

(A)

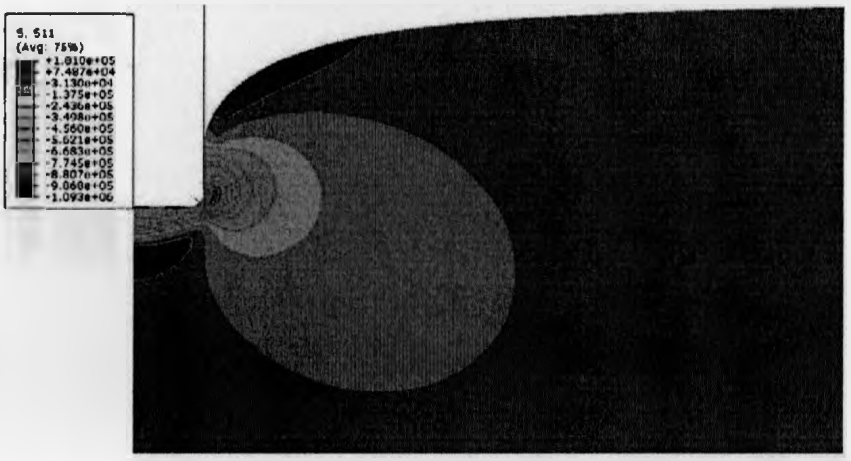

(B)

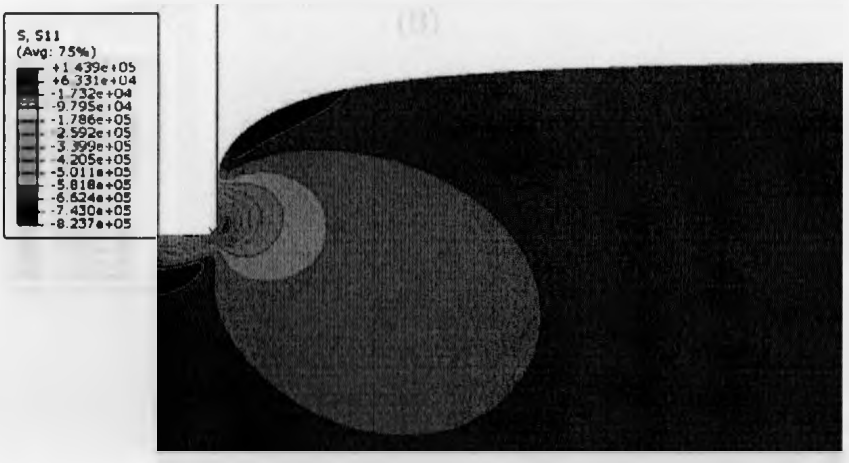

(C)

Figure 4-10: σ_r contours of A) PDMS B) 5% clay-PDMS nanocomposite C) 7% clay-PDMS nanocomposite indented by flat-ended cylindrical indenter at 1.6 *mm*.

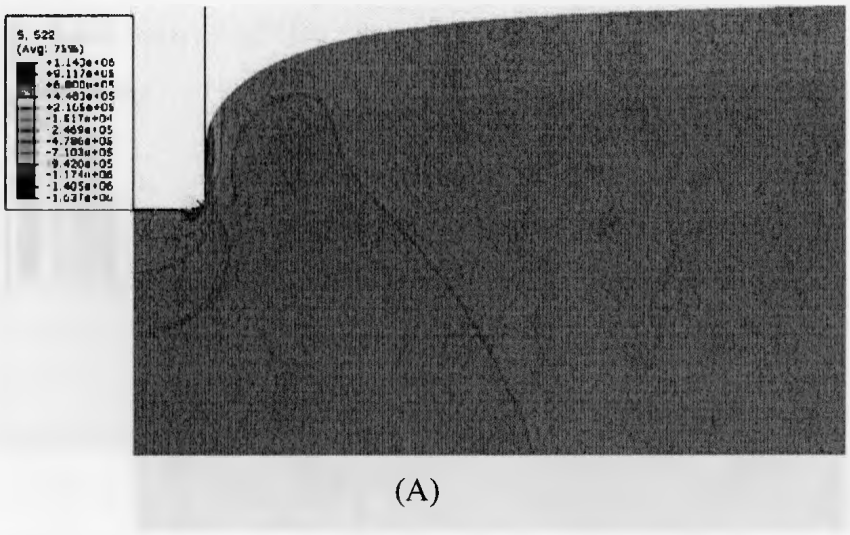

(A)

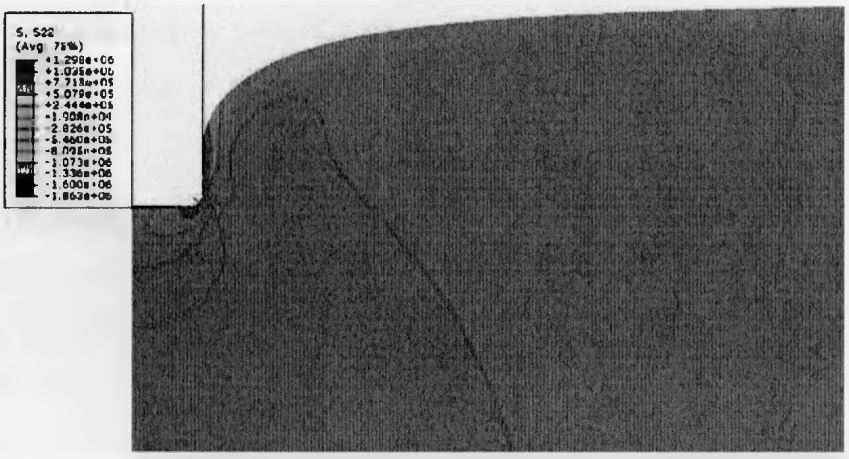

(B)

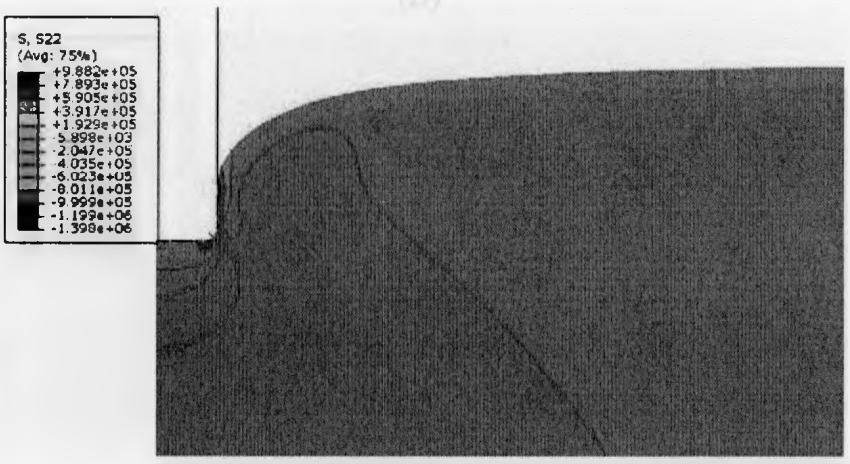

(C)

Figure 4-11: σ_z contours of A) PDMS B) 5% clay-PDMS nanocomposite C) 7% clay-PDMS nanocomposite indented by flat-ended cylindrical indenter at $1.6\,mm$.

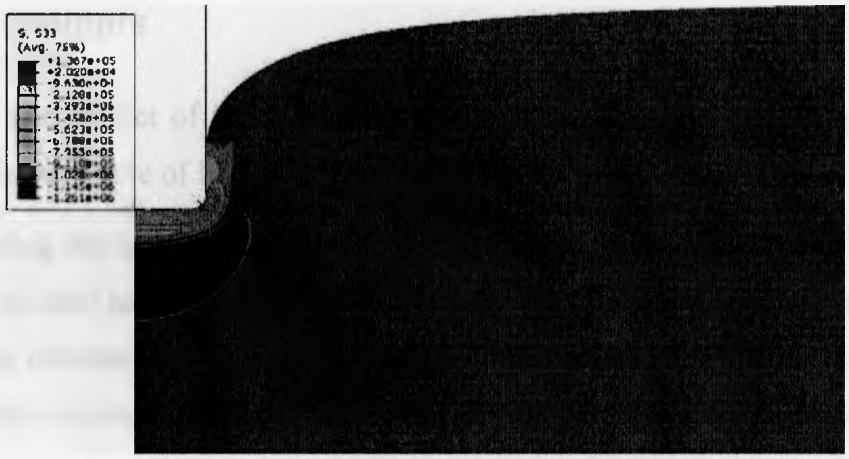

(A)

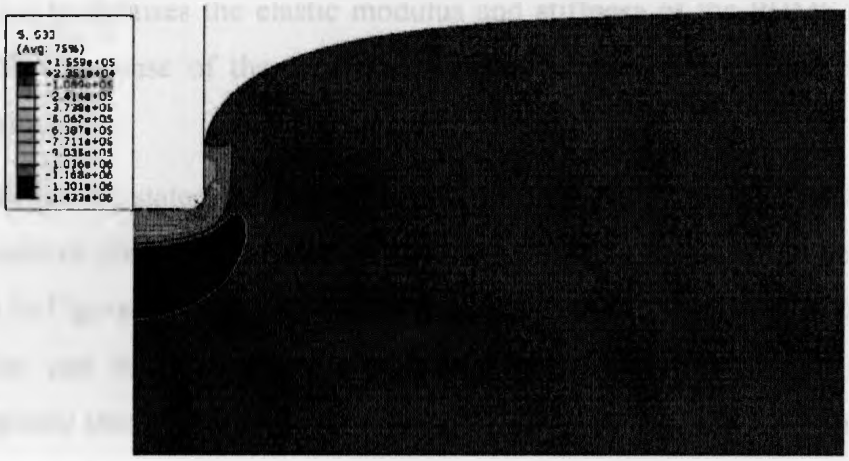

(B)

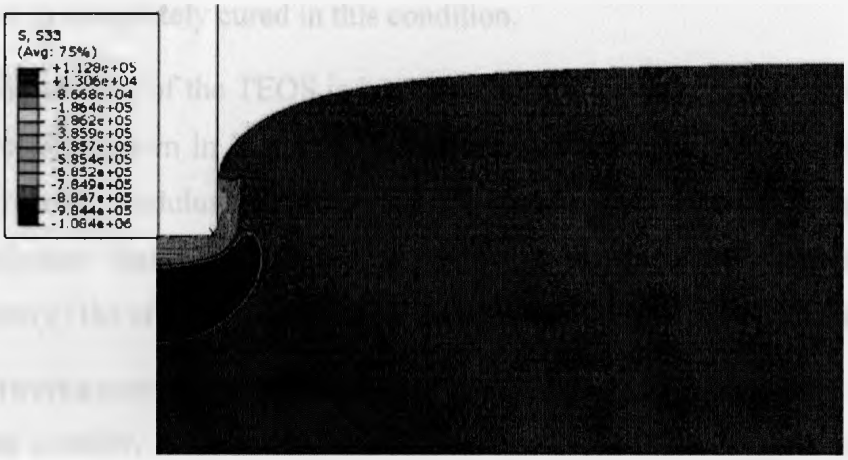

(C)

Figure 4-12: σ_θ contours of A) PDMS B) 3% clay-PDMS nanocomposite C) 7% clay-PDMS nanocomposite indented by flat-ended cylindrical indenter at 1.6 *mm*.

4.5 Effect of the amount of the cross-linker on the indentation curves and stress contours

In this part, effect of the different degrees of the cross-linker on the indentation load-displacement curve of PDMS is discussed.

Examining the stress-strain curves of PDMS with various amount of cross-linker obtained by uniaxial tensile testing shown in Figure 4.13 reveals that increasing the cross-linker amount elevates the ultimate stress value in the case of PDMS-R5, and the ultimate stress and strain values dropped off for PDMS-R11 sample. The ultimate strain of PDMS-R5 approximately was close to that of PDMS-R2.2. In addition the increase of the cross-linker from 2.2 to 5 raises the elastic modulus and stiffness of the PDMS significantly although further increase of the cross-linker up to 11 does not enhance the Young's modulus significantly.

Moloodi (2009) stated the reason for the different behaviors of PDMS containing various amounts of cross-linker based on the transformation of the tetrafunctional cross-linker shown in Figure 4.14. As mentioned in regard to in situ formation of the silica, the silica particles can be formed via hydrolyzing of the extra amount of cross-linker. Moloodi proposed that in the optimum amount of cross-linker ($R = 2.2$), the number of cross-linker reactive groups after hydrolysis process is equal to the number of chain ends since the chain is completely cured in this condition.

Since the amount of the TEOS is increased up to five, there would be some groups of silica molecules shown in Figure 4.14-B with more branches. All the chain ends are bounded and elastic modulus and stiffness of the network enhance due to interaction of silica and polymer chains. In addition flexibility of the silica networks and minimal interpenetration of the chains leads the increase of flexibility and ultimate strain.

The silica networks converts to the three dimensions shown in Figure 4.14-C reducing its flexibility and mobility with further increase of the cross-linker degree. As the result modulus is increased and ultimate strain is decreased.

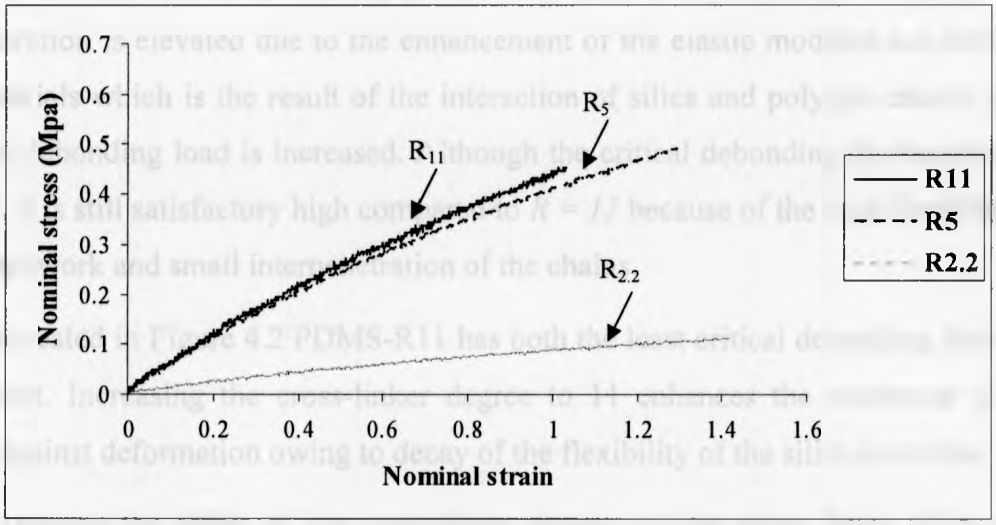

Figure 4.13: Nominal stress-strain curves of the PDMS with different amount of cross-linker obtained from uniaxial compression test.

Name	Rupture Strain	Rupture Stress (Mpa)
PDMS-R_{22}	1.42	0.111
PDMS-R_5	1.29	0.487
PDMS-R_{11}	1.034	0.452

Table 4.8: The rupture stress and strain values obtained by uniaxial tensile test for PDMS with different amount of the cross-linker

To further examine the effect of cross-linker indentation tests were carried out and surprisingly no crack initiation or indenter imprint was observed in the case of PDMS-R2.2 due to excellent flexibility of the networks even for deep indenter penetration.

Once the cross-linker amount is increased to five, the indenter load required for deep penetration is elevated due to the enhancement of the elastic modulus and stiffness of the materials which is the result of the interaction of silica and polymer chains. Thus the critical debonding load is increased. Although the critical debonding displacement is decreased, it is still satisfactory high compared to $R = 11$ because of the high flexibility of the silica network and small interpenetration of the chains.

As revealed in Figure 4.2 PDMS-R11 has both the least critical debonding load and displacement. Increasing the cross-linker degree to 11 enhances the resistance of the materials against deformation owing to decay of the flexibility of the silica networks.

To examine the effect of the cross-linker amount on the stress fields; FEA were performed for PDMS containing various amounts of cross-linker at the specific indenter depth 1.6 *mm*. Results obtained by FEA indicate that by increasing the cross-linker amount, the stress values increases. No difference was observed in terms of contour shape between PDMS with different cross-linker degrees illustrated in Figure 4.15-Figure 4.17.

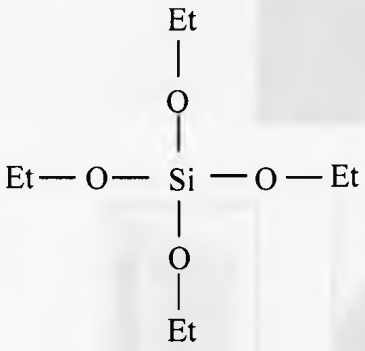

(A) Tetra functional TEOS

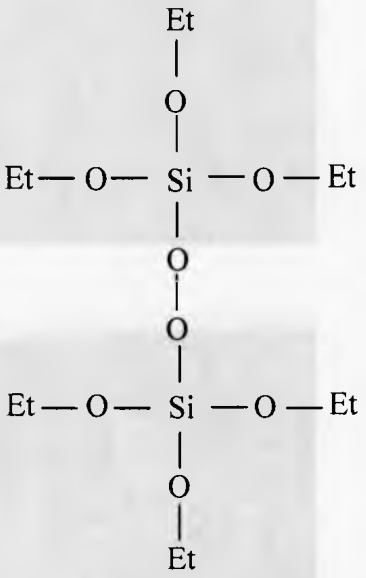

(B) Cross-linker with seven active groups

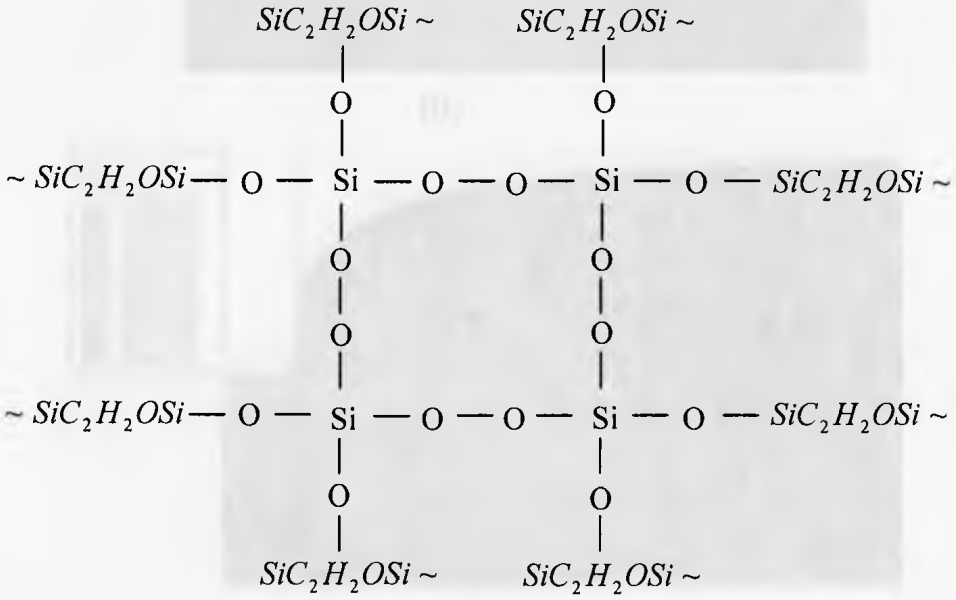

(C) Silica network as a particle

Figure 4.14: Schematic of the cross-linker molecules (Moloodi 2009).

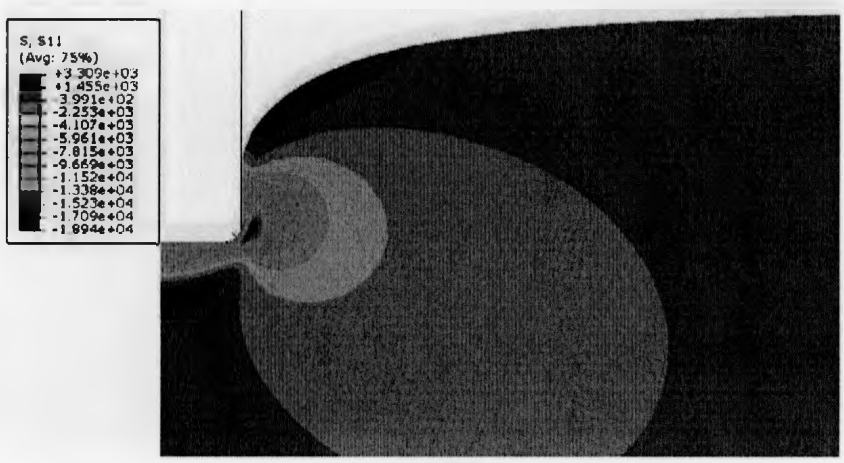

(A)

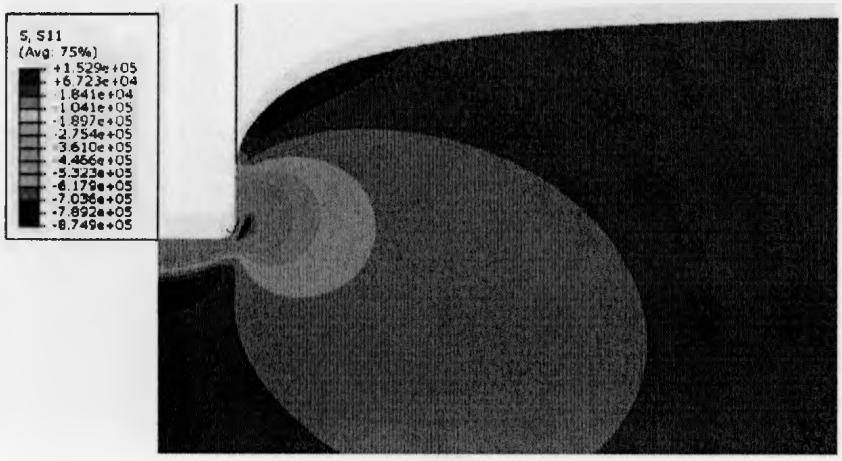

(B)

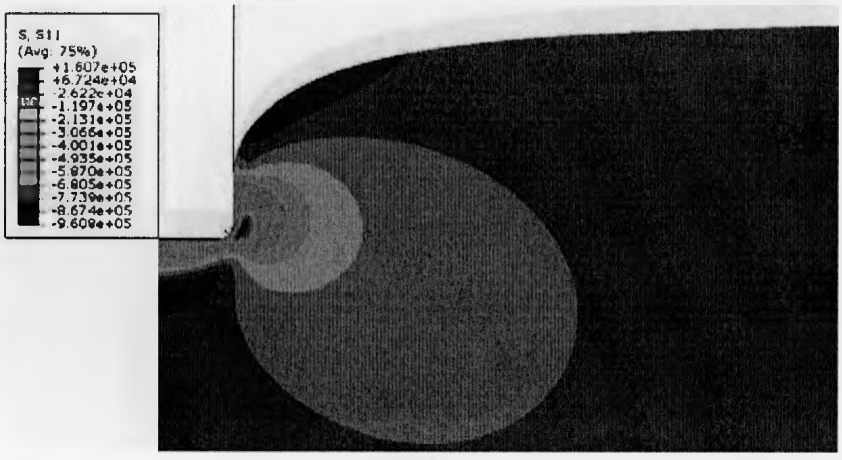

(C)

Figure 4.15: Radial stress (σ_r) contours of A) PDMS-$R_{2.2}$ B) PDMS-R_5 C) PDMS-R_{11} indented by flat-ended cylindrical indenter at $Z = 1.6\ mm$.

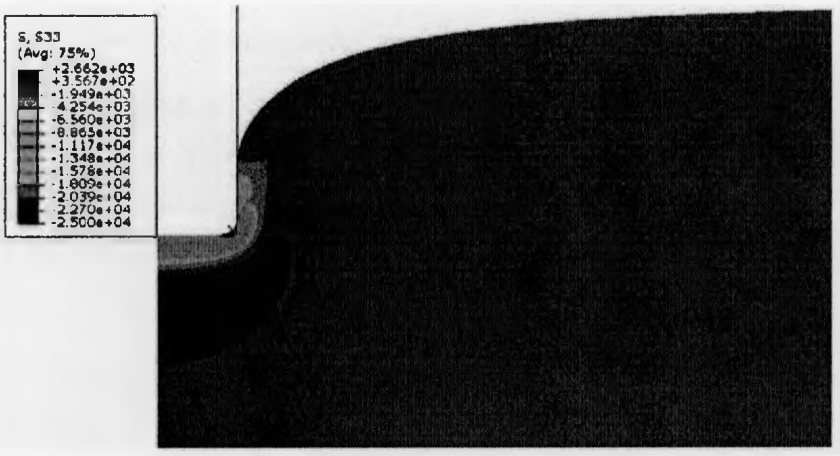

(A)

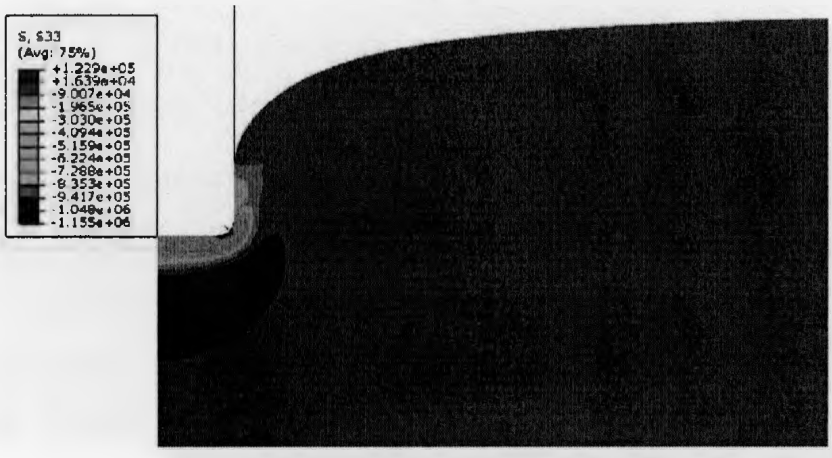

(B)

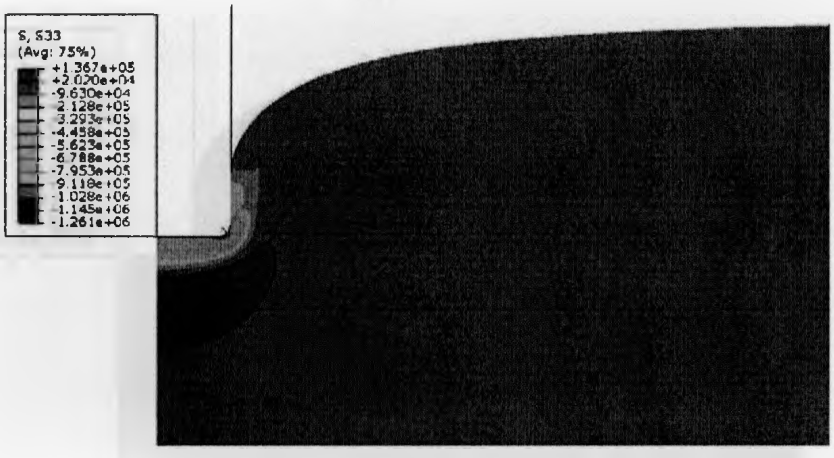

(C)

Figure 4.16: Hoop stress (σ_θ) contours of A) PDMS-$R_{2.2}$ B) PDMS-R_5 C)PDMS-R_{11} indented by flat-ended cylindrical indenter at $Z = 1.6\ mm$.

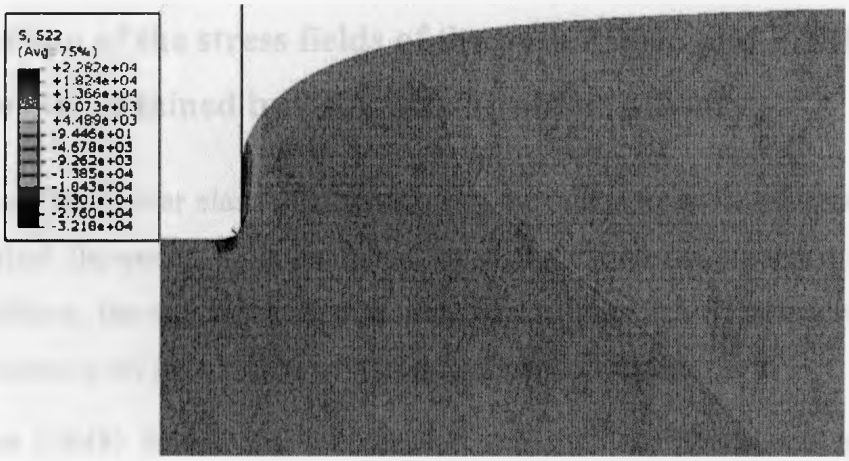

(A)

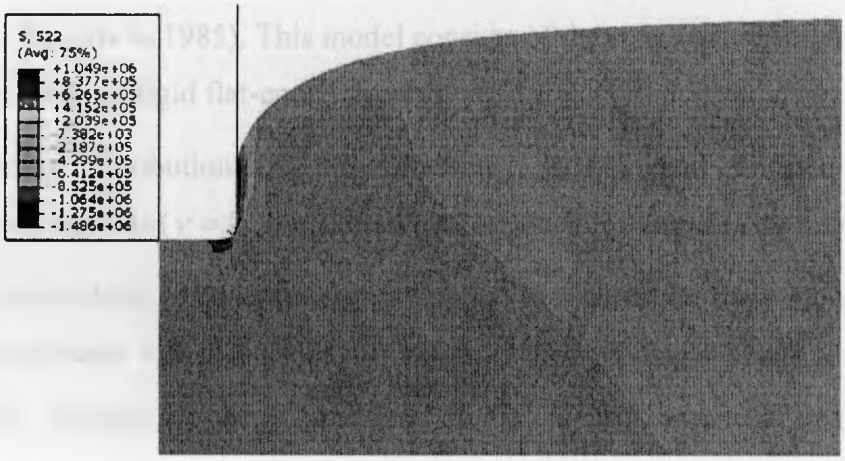

(B)

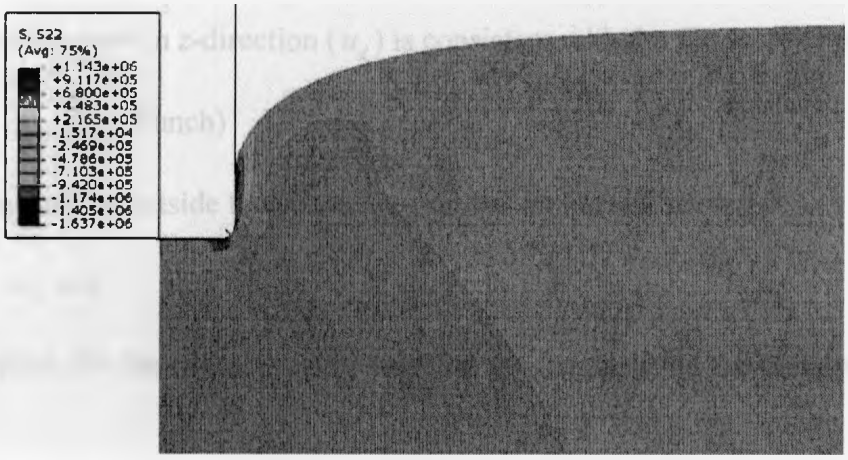

(C)

Figure 4.17: Axial stress (σ_z) contours of A) PDMS-R_{22} B) PDMS-R_5 C) PDMS-R_{11} indented by flat-ended cylindrical indenter at $Z = 1.6\ mm$.

4.6 Comparison of the stress fields of the bulk PDMS and PDMS-clay nanocomposites obtained by FEA with Sneddon's theory

In this section, linear elastic deformation of the incompressible materials ($\nu = 0.5$) under cylindrical flat-ended tip is examined by analytical model proposed by Sneddon (1964). In addition, the stress distribution under rigid flat punch obtained by Sneddon's theory is compared with FEA results of PDMS and nanocomposite.

Sneddon (1945) solved the problem of a frictionless flat punch indenting an isotropic, homogeneous and linear elastic half-space (with misprints later corrected by Mouginot and Maugis in 1985). This model consists of the stress distribution in the semi-infinite elastic body by rigid flat-ended punch.

The stress distribution of the filled-clay PDMS and unfilled PDMS as incompressible materials ($\nu = 0.5$) indented by flat punch is computed as follows:

In this calculation, axial symmetry is applied to semi-finite body along z-axis and cylindrical coordinates r, θ, z is used. It is assumed that the displacement in θ-direction and tangential stresses, $\tau_{r\theta}, \tau_{z\theta}$ are zero. It is further assumed that along the boundary $z = 0$:

The displacement in z-direction (u_z) is consistent with the flat facet of the punch.

$$u_z = u_z \text{ (Punch)} \qquad 0 \le r \le a$$

The free surface outside the contact region has no normal stress (σ_z).

$$\sigma_z = 0 \qquad r > a$$

The friction for the contact region between the indenter and the half-space is equal to zero.

$$\tau_{zr} = 0 \qquad \text{For all values of r}$$

The components of the stress ($\sigma_r, \sigma_\theta, \sigma_z, \tau_{rz}$) under flat-ended punch are given by following equations:

$$\frac{\sigma_z}{P_m} = -\frac{1}{2}\left[J_1^0 + \frac{z}{a}.J_2^0 \right] \tag{4-6}$$

$$\frac{\sigma_r}{P_m} = -\frac{1}{2}\left[J_1^0 - \frac{z}{a}.J_2^0 - (1-2\nu).\frac{a}{r}.J_0^1 + \frac{z}{r}.J_1^1 \right] \tag{4-7}$$

$$\frac{\sigma_\theta}{P_m} = -\frac{1}{2}\left[2\nu J_1^0 + (1-2\nu).\frac{a}{r}.J_0^1 - \frac{z}{r}.J_1^1 \right] \tag{4-8}$$

$$\frac{\tau_{rz}}{P_m} = -\frac{1}{2}\frac{z}{a}.J_2^1 \tag{4-9}$$

Unknown parameters are calculated as follows:

$$J_1^0 = R^{-1/2}.Sin\frac{\varphi}{2}$$

$$J_0^1 = \frac{a}{r}.\left(1 - R^{-1/2}.Sin\frac{\varphi}{2}\right)$$

$$J_2^1 = \frac{r}{a}.R^{-3/2}.Sin\frac{3\varphi}{2}$$

$$J_2^0 = \left[1 + \frac{z^2}{a^2}\right]^{1/2}.R^{-3/2}.Sin\left(\frac{3\varphi}{2} - \theta\right)$$

$$J_1^1 = \left[1 + \frac{z^2}{a^2}\right]^{1/2}.\frac{a}{r}.R^{-1/2}.Sin\left(\theta - \frac{\varphi}{2}\right)$$

$$R = \left\{\left[\frac{r^2}{a^2} + \frac{z^2}{a^2} - 1\right]^2 + 4.\frac{z^2}{a^2}\right\}^{1/2}$$

$$\tan\varphi = 2\frac{z}{a}\frac{1}{(r^2/a^2) + (z^2/a^2) - 1}$$

$$\tan\theta = \frac{a}{z} \quad , \quad P_m = \frac{2Eh}{\pi a(1-\nu^2)}$$

r is the radial distance, z the vertical distance into the specimen, a the indenter radius, P_m the indentation pressure, h indenter displacement and ν the Poisson's ratio. For PDMS and nanocomposites of the clay and PDMS categorized in the incompressible materials group, Poisson's ratio is chosen to be 0.5 (Gent 1954, Livermore et al. 2005, Carrillo et al 2005).

Radial, axial, hoop and shear stress distributions at $Z = 1.25mm$ and $h = 0.75mm$ along radial distance were plotted by analytical model proposed by Sneddon to compare with FEA results of PDMS-R11. FEA results and Sneddon's theory have a good agreement in terms of both trend and stress magnitude with Sneddon's theory in the case of PDMS-R11 while hoop stress distribution is different with regards to stress values.

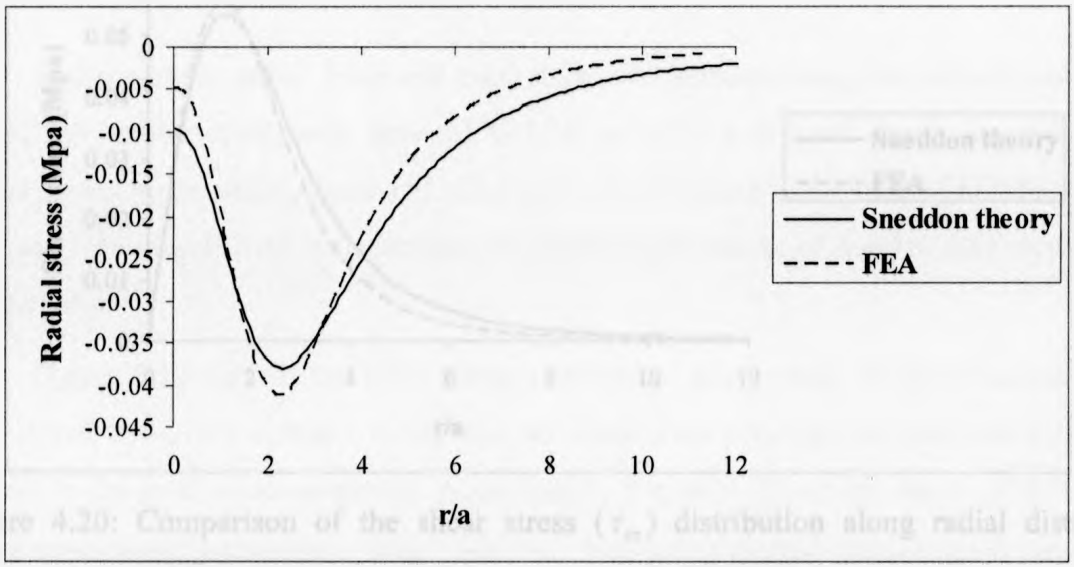

Figure 4.18: Comparison of the radial stress (σ_r) distribution along radial distance obtained by Sneddon's theory with FEA result for bulk PDMS-R_{11}.

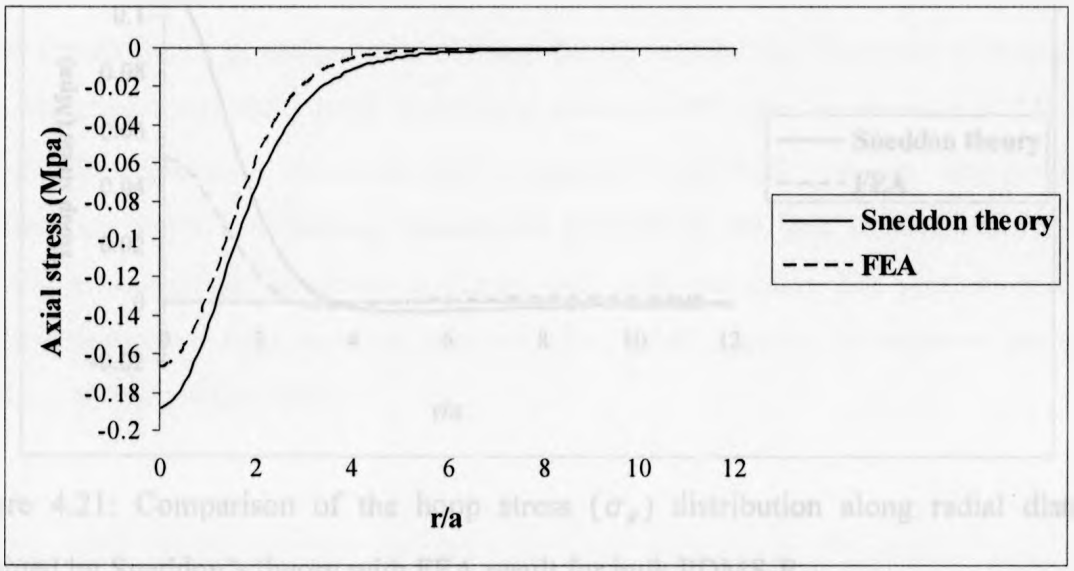

Figure 4.19: Comparison of the axial stress (σ_z) distribution along radial distance obtained by Sneddon's theory with FEA result for bulk PDMS-R_{11}.

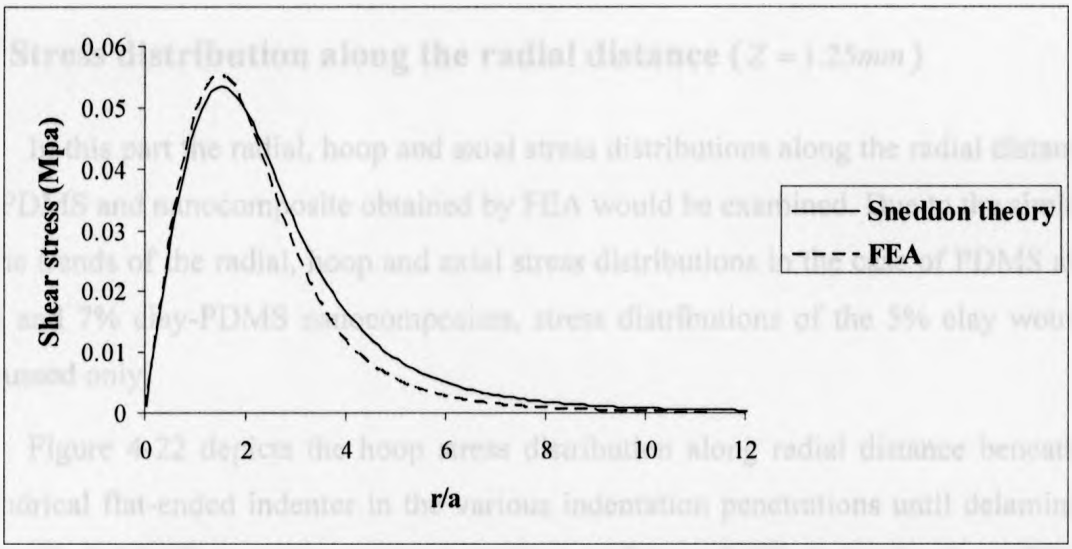

Figure 4.20: Comparison of the shear stress (τ_{rz}) distribution along radial distance obtained by Sneddon's theory with FEA result for bulk PDMS-R_{11}.

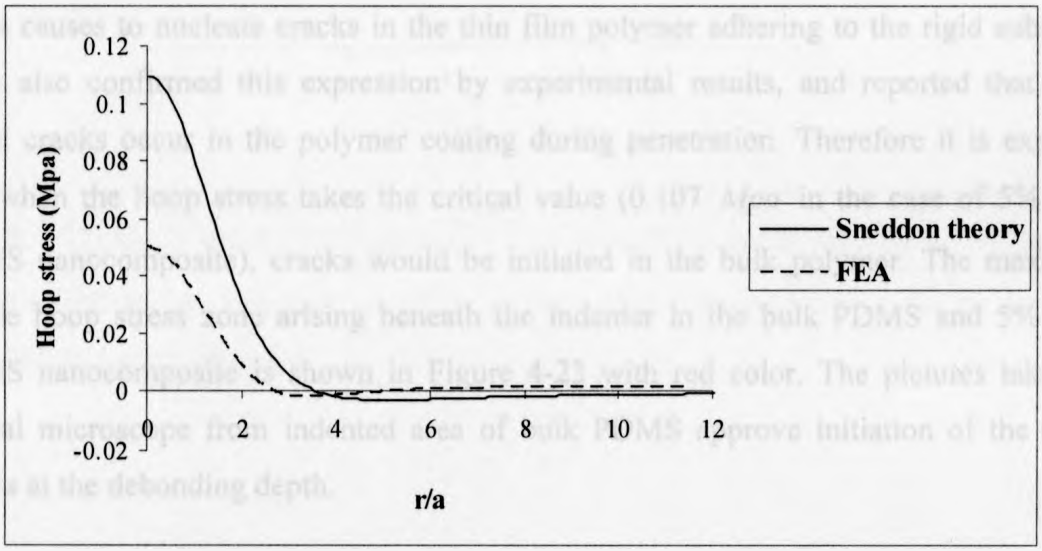

Figure 4.21: Comparison of the hoop stress (σ_θ) distribution along radial distance obtained by Sneddon's theory with FEA result for bulk PDMS-R_{11}.

4.7 Stress distribution along the radial distance ($Z = 1.25mm$)

In this part the radial, hoop and axial stress distributions along the radial distance of the PDMS and nanocomposite obtained by FEA would be examined. Due to the similarity of the trends of the radial, hoop and axial stress distributions in the case of PDMS and 1, 3, 5 and 7% clay-PDMS nanocomposites, stress distributions of the 5% clay would be discussed only.

Figure 4-22 depicts the hoop stress distribution along radial distance beneath the cylindrical flat-ended indenter in the various indentation penetrations until delamination occurs in the bulk nanocomposite. According to Figure 4-22, at the depth of 400 μm hoop stress takes the negative value near zero. Increasing the indentation depth leads the hoop stress to take the positive value initially and then gradually reduces to zero around $3a$ away from the indenter axis. Lu and Shinozaki (1999) stated that the tensile hoop stress causes to nucleate cracks in the thin film polymer adhering to the rigid substrate. They also confirmed this expression by experimental results, and reported that some radial cracks occur in the polymer coating during penetration. Therefore it is expected that when the hoop stress takes the critical value (0.107 Mpa in the case of 5% clay-PDMS nanocomposite), cracks would be initiated in the bulk polymer. The maximum tensile hoop stress zone arising beneath the indenter in the bulk PDMS and 5% clay-PDMS nanocomposite is shown in Figure 4-23 with red color. The pictures taken by optical microscope from indented area of bulk PDMS approve initiation of the radial cracks at the debonding depth.

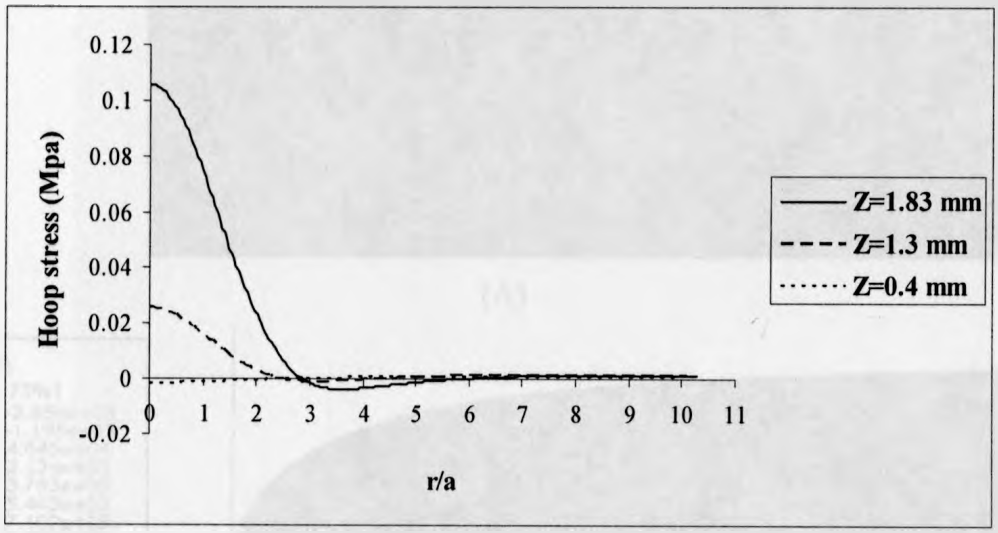

Figure 4-22: Hoop stress Distribution (σ_θ) along radial distance normalized by indenter radius in the various penetrations of the flat indenter obtained by FEA for the bulk 5% clay-PDMS nanocomposite.

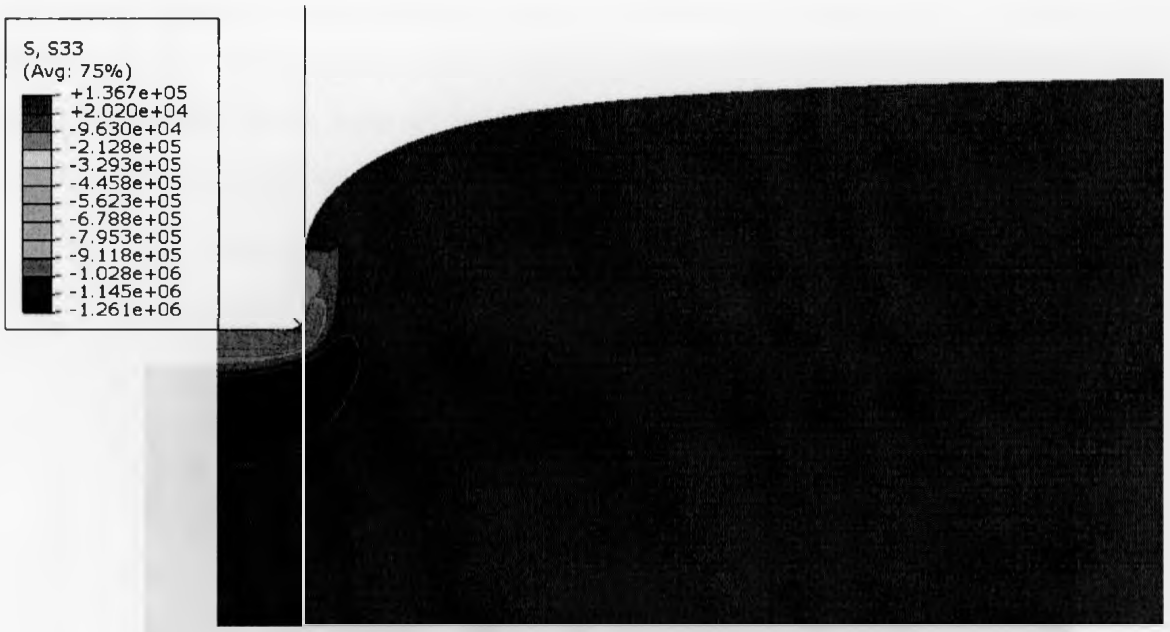

(A)

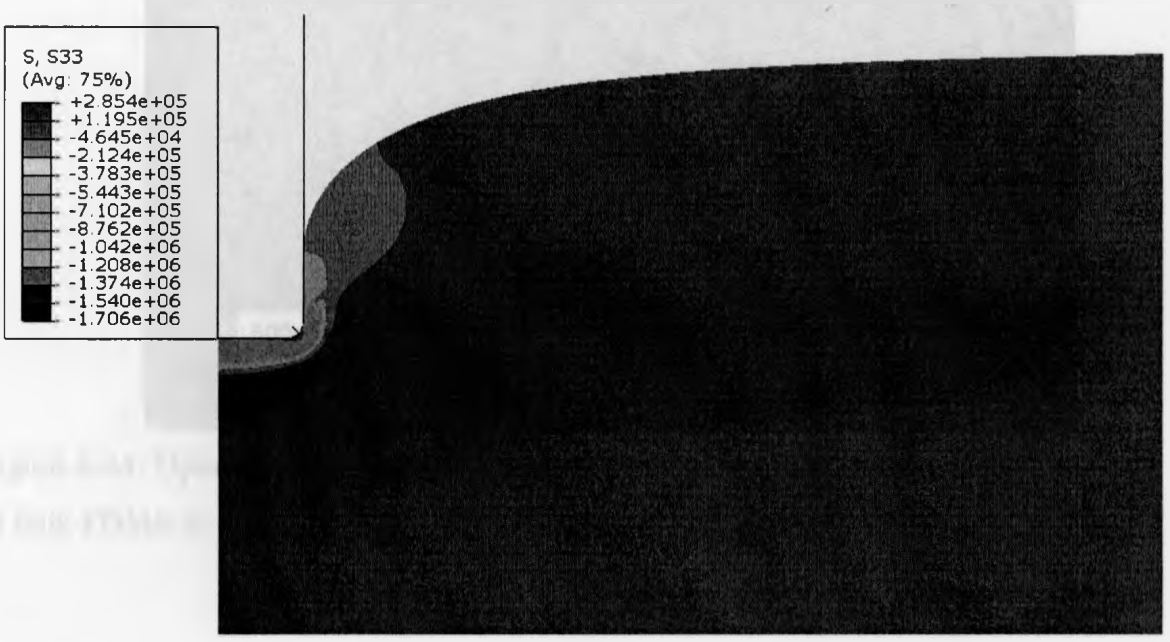

(B)

Figure 4-23: Hoop stress (σ_θ) contours of A) PDMS B) 5% clay-PDMS nanocomposite at the debonding depth.

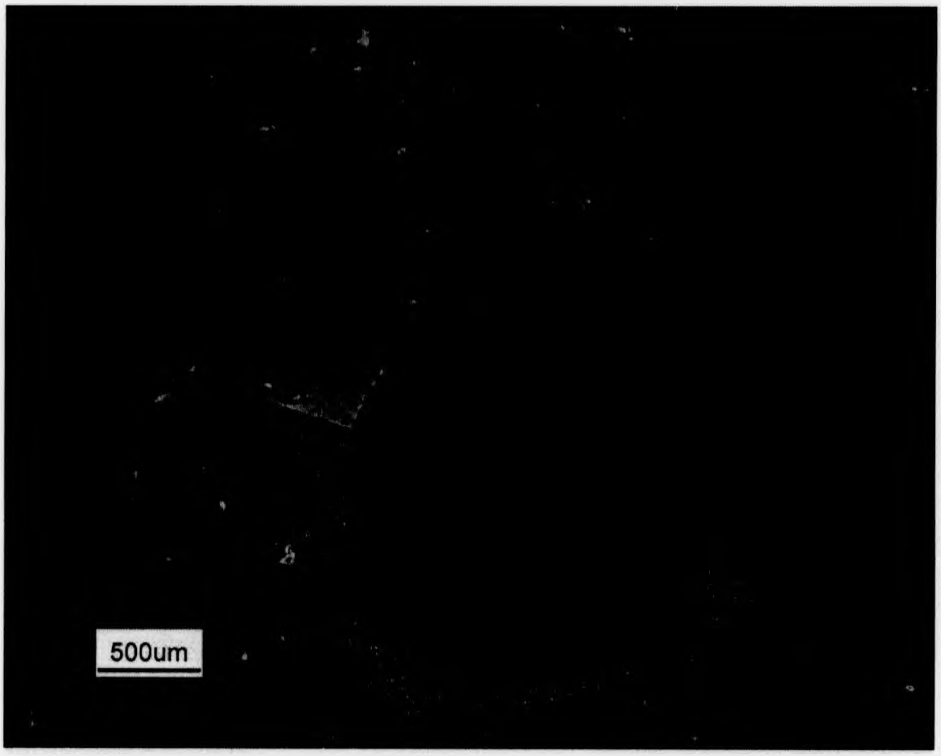

Figure 4-24: Optical micrograph illustrating the initiation of the radial cracks in the case of bulk PDMS-R_{11}.

The radial stress drops off from the positive values to negative around $2a$ from symmetrical axis and then builds up to zero as illustrated in Figurue 4-25. It is also well understood that the increase of the indenter penetration leads to higher radial stress values. The tensile stress zone arising beneath the flat indenter is shown in Figure 4-27 with red color for PDMS and 5% clay nanocomposite.

The axial stress starts from the negative value and then slightly reduces to zero at $r = 5a$ away from the center of the indenter.

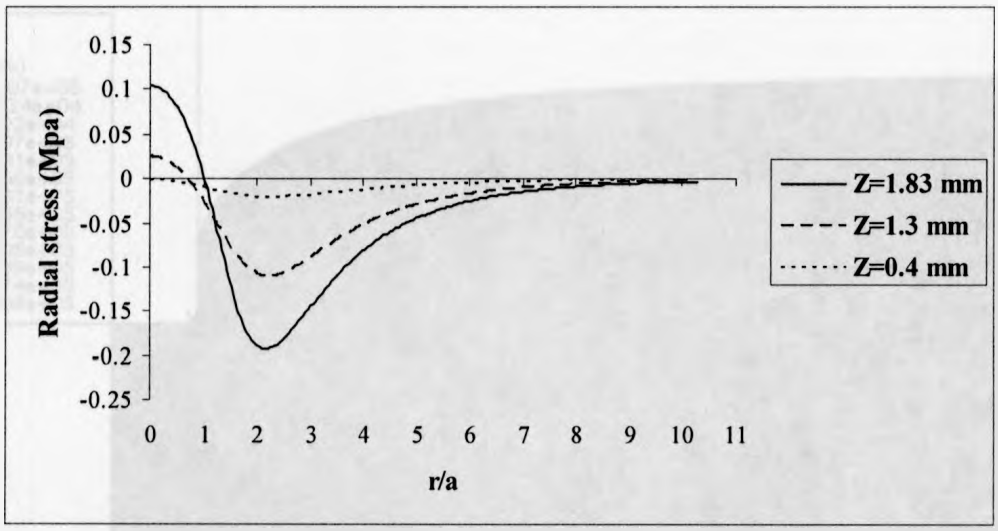

Figurue 4-25: Distribution of the radial stress (σ_r) along radial distance normalized by indenter radius (depth = $1250\mu m$) in the various penetrations of the flat indenter obtained by FEA for the bulk 5% clay-PDMS nanocomposite.

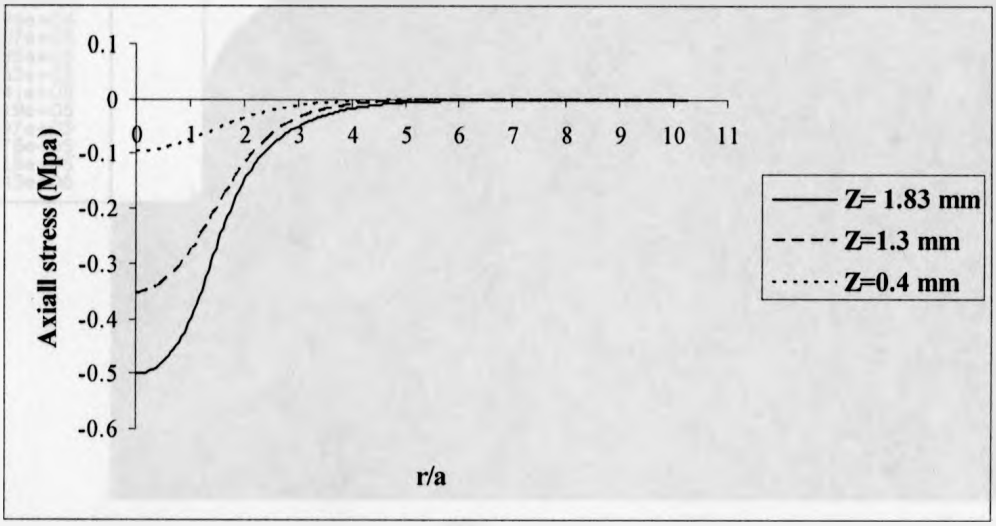

Figure 4-26: Distribution of the axial stress (σ_z) along radial distance normalized by indenter radius (depth = $1250\mu m$) in the various penetrations of the flat indenter obtained by FEA for the bulk 5% clay-PDMS nanocomposite.

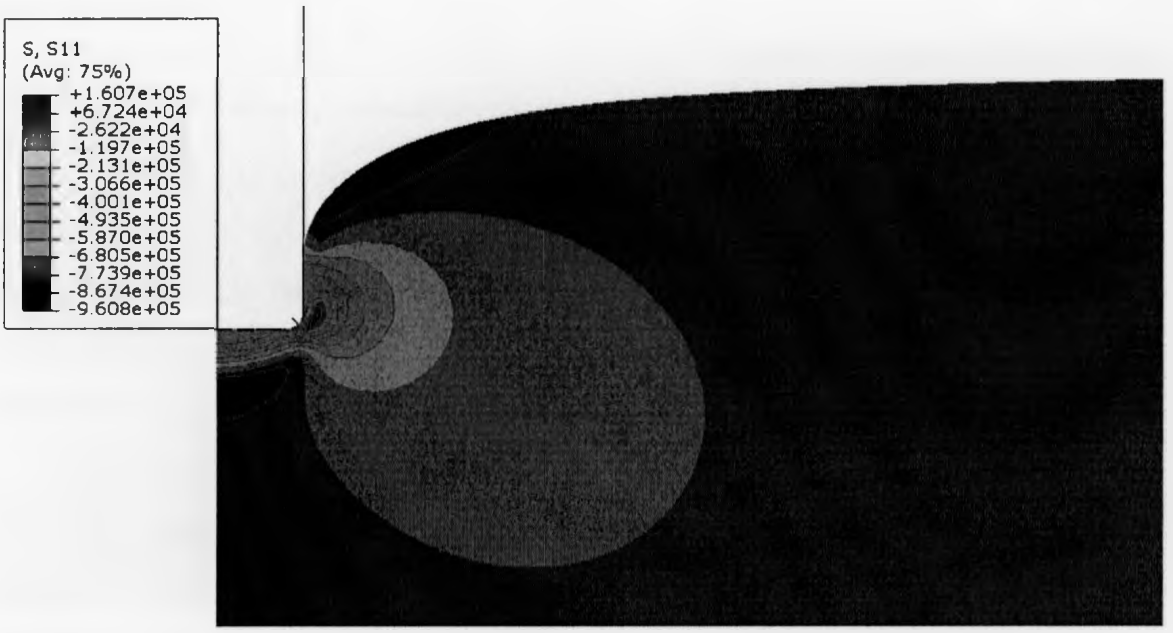

(A)

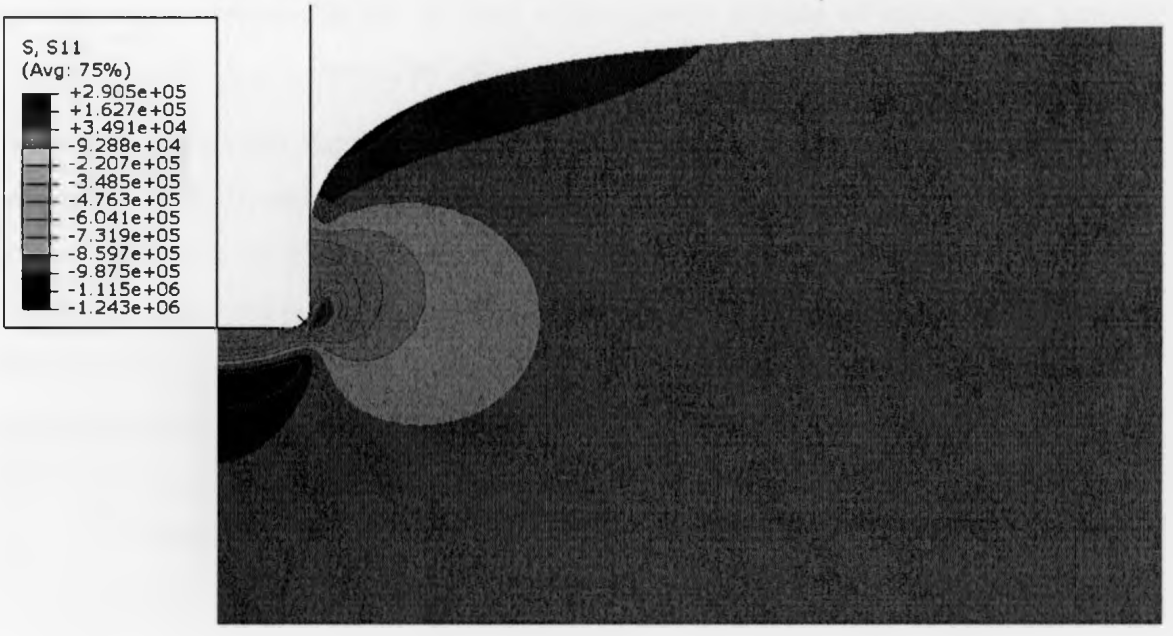

(B)

Figure 4-27: Radial stress (σ_r) contours of A) PDMS B) 5% clay-PDMS nanocomposite at the debonding depth.

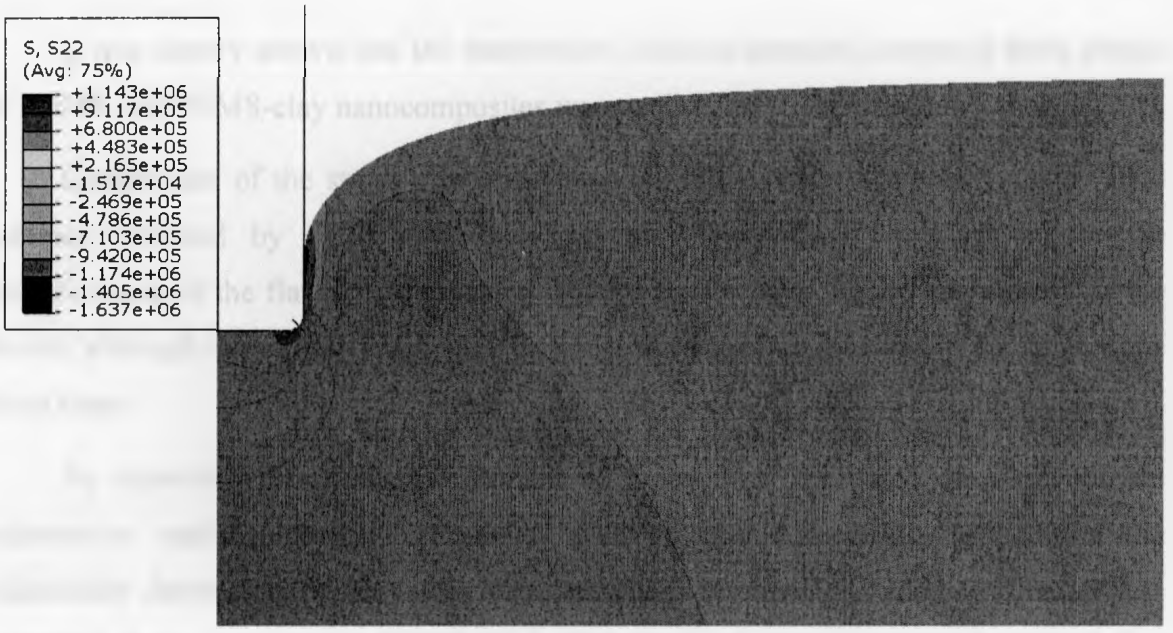

(A)

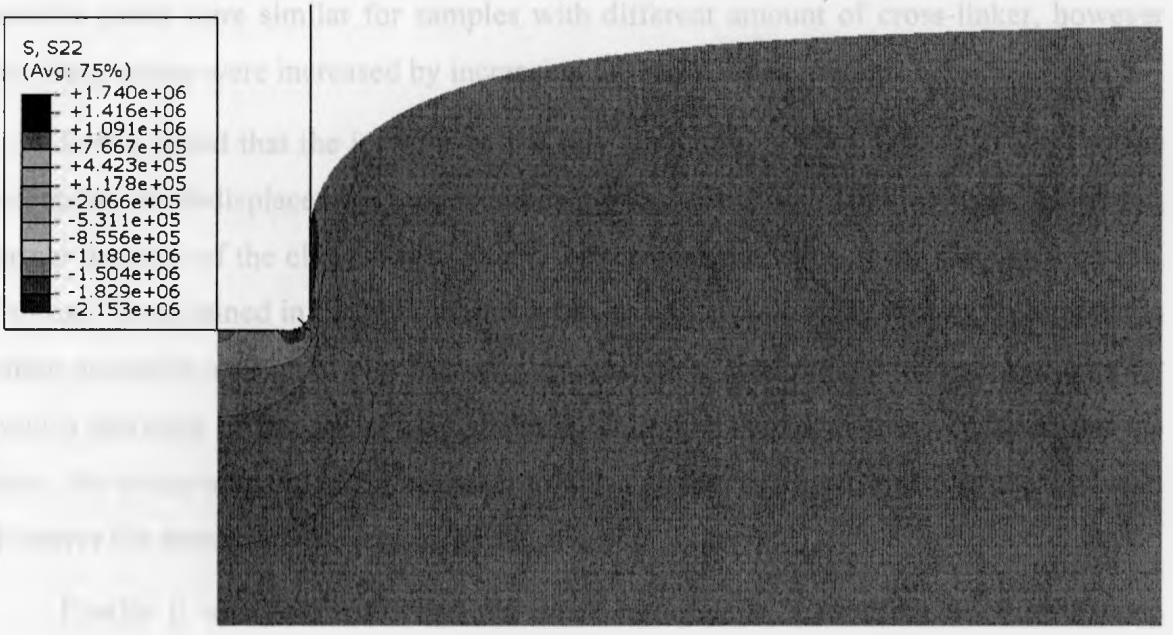

(B)

Figure 4-28: Axial stress (σ_z) contours of A) PDMS B) 5% clay-PDMS nanocomposite at the debonding depth.

4.8 Conclusion

It was clearly shown that the indentation load-displacement curves of thick blocks of PDMS and PDMS-clay nanocomposites were well-fitted to the Sneddon's theory.

Comparison of the stress distributions (axial, radial, hoop and shear) along radial distance obtained by FEA with analytical model proposed by Sneddon (in the neighborhood of the flat punch) revealed that the results have a good consistency as the model, although the stress values were different from predicted values in the case of the hoop stress.

As expected, increasing the amount of cross-linker increased the slope of the indentation load-displacement curves as well as elastic modulus. In addition the indentation debonding depth values were elevated. Interestingly no delamination was observed in the case of the PDMS-R2.2. The shape of stress contours examined at a specific depth were similar for samples with different amount of cross-linker, however the stress values were increased by increasing the cross-linker amount.

It was found that the increase of the clay amount up to % 5 raises the slope of the indentation load-displacement curves indicating that debonding load increases. However, further increase of the clay from % 5 to % 7 decreased the slope of the examined curves. This can be explained in the light of clay particles and cross-linking molecules interaction where excessive amount of clay prevents vulcanization. Examining the stress contours for various amounts of the added clay showed, while the shapes of these contours are the same, the stress magnitudes increase up to 5% clay due to improvement of the stiffness. However the stress values decrease in the case of 7% clay.

Finally it was confirmed that the crack initiation is a result of the tensile hoop stress.

Chapter 5. INDENTATION OF THE PDMS AND CLAY FILLED PDMS THIN FILMS

This chapter deals with the indentation of PDMS and PDMS-clay nanocomposite thin films adhering on a glass substrate. Stress distributions near the interface of thin film-glass substrate and validity of the analytical theory proposed by Dehm et al (1992) will be discussed. Finally critical interfacial shear strength leading to failure between film and substrate will be calculated by Dehm et al.'s theory (1992).

5.1 Indentation load-displacement behavior of filled and unfilled PDMS thin films

A flat cylindrical indenter was pushed into PDMS and nanocomposite at the same preselected displacement rate used for the bulk PDMS and nanocomposite. After observation of load drop, indenter was unloaded to zero followed by recording indenter load versus indenter displacement.

Figure 5.1 illustrates load–displacement curves of the filled and unfilled PDMS thin films adhering to the glass substrate. Critical load, stress and depth are considered as a point where load drop is observed given in Table 5.1. It was found that PDMS-R11 has the highest critical load and depth compared to others. In the other word, increasing the clay amount reduces both critical load and depth.

It can be seen from the same figure that load magnitudes in the indentation load-displacement curves are higher than those of bulk PDMS and nanocomposite. When the flat indenter is pushed into an elastic thin film adhering to the rigid substrate, the materials beneath the indenter are pushed away and deformed elastically. The rigid substrate constrains the deformation of the materials in the higher indenter depth. Therefore more indenter load is required for penetration of the flat tip. In the other word, due to the effect of substrate load magnitudes in the indentation load-displacement curves are higher than those of bulk PDMS and composite. Cheng et al. (2000) suggested that

the measured elastic moduli of the polymer films indented by a flat indenter are higher than those of bulk materials because of effect of the substrate.

In the previous chapter, linear load-displacement relationship proposed by Sneddon for cylindrical flat indenter was proved for indentation of the bulk PDMS and clay-PDMS nanocomposite. However, as shown in Figure 5.1 indentation load-displacement curves of PDMS and nanocomposite thin films do not follow a linear relationship similar to those of bulk PDMS and composite.

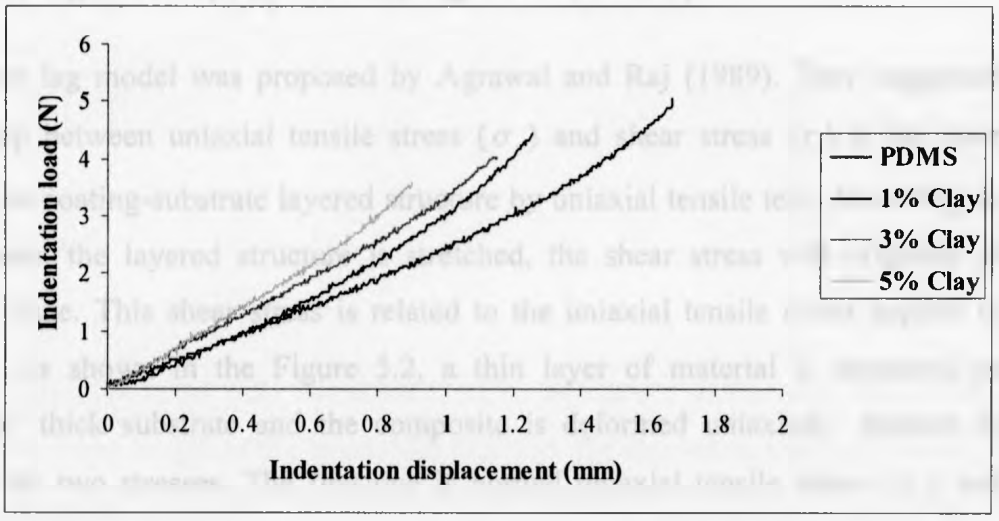

Figure 5.1: Indentation load-displacement curves of the PDMS-R_{11} and PDMS-clay nanocomposite thin films with various amount of the clay.

	Coating Thickness (mm)	Critical Indentation Debonding Depth H_f (mm)	Critical Indentation Debonding Load F_c (N)	Critical Indentation Debonding Stress P_c (MPa)
PDMS-R_{11}	2.54	1.674	5.027	6.4
1% Clay	1.88	1.259	4.428	5.64
3% Clay	1.733	1.152	4.03	5.13
5% Clay	1.3354	0.9	3.582	4.56

Table 5.1: The critical indentation debonding load, stress and depth obtained from indentation curves for PDMS-R_{11} and PDMS-R_{11}-clay nanocomposite thin films adhering on the glass substrate.

5.2 Shear lag model proposed by Agrawal and Raj

Shear lag model was proposed by Agrawal and Raj (1989). They suggested the relationship between uniaxial tensile stress (σ_r) and shear stress (τ) at the interface plane of the coating-substrate layered structure by uniaxial tensile test. According to this model, when the layered structure is stretched, the shear stress will originate at the interface plane. This shear stress is related to the uniaxial tensile stress applied to the structure. As shown in the Figure 5.2, a thin layer of material is deposited on an "infinitely" thick substrate and the composite is deformed uniaxially. Section AB is subjected by two stresses. The first one is normal uniaxial tensile stress (σ_r) and the second one is shear stress between coating and substrate. In this model, two important assumptions are considered:

- The shear stress (τ) follows sinusoidal shape with wavelength of λ_0

$$\tau = \tau_{max} \sin\left(\frac{\pi r}{\lambda_0 / 2}\right) \qquad \left(0 \le r \le \frac{\lambda_0}{2}\right) \tag{5.1}$$

where τ_{max} represents the peak stress or the maximum stress that the interface can support.

- The uniaxial tensile stress (σ_r) is constant and uniform in the middle of the region AB and gradually decreases in outer regions.

If mechanical equilibrium condition is applied to the region AB, it yields:

$$\left(\frac{\partial \sigma_r}{\partial r}\right) + \left(\frac{\partial \tau_{rz}}{\partial z}\right) = 0 \tag{5.2}$$

In the equation (5.3), τ is the shear stress on the interface plane, and δ is the film thickness.

$$\left(\frac{\partial \sigma_r}{\partial r}\right) = \frac{\tau}{\delta} \tag{5.3}$$

Integrating the sinusoidal function of shear stress, the uniaxial tensile stress is obtained by Eq.(5.5):

$$\sigma_r = \frac{1}{\delta}\int_0^r \tau dr \tag{5.4}$$

$$\sigma_r = \frac{\tau_{max}\lambda_0}{\pi.\delta} \tag{5.5}$$

Eq.(5.5) shows that with calculation of two parameters of fracture stress of the film (σ_r) and the wave length of the sinusoidal function, the maximum interfacial shear stress could be computed.

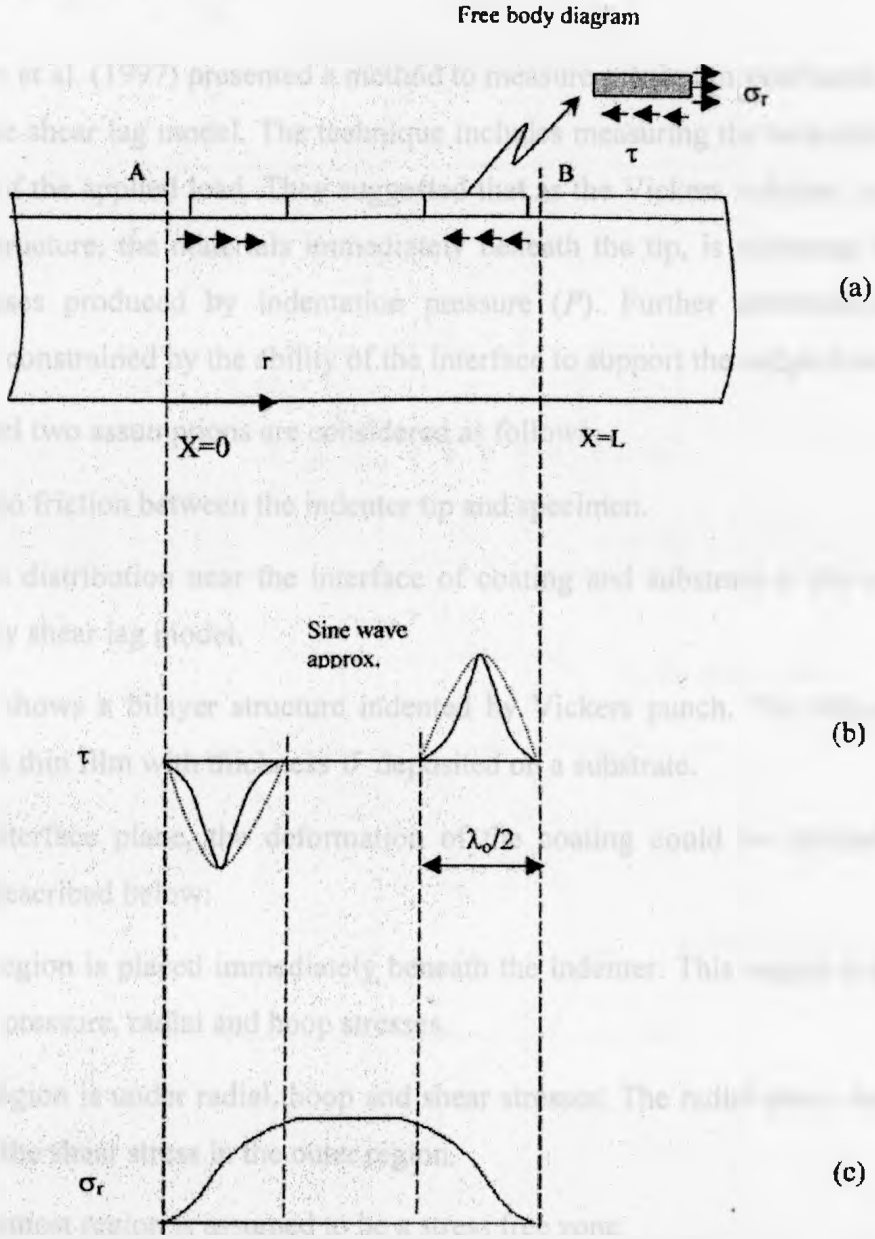

Figure 5.2: a) Shear b) uniaxial tensile stress distributions at the interface of coating-substrate proposed by Agrawal and Raj (Lu 1999).

5.3 Dehm et al.'s model

Dehm et al. (1997) presented a method to measure maximum interfacial shear stress based on the shear lag model. The technique includes measuring the indentation depth as a function of the applied load. They suggested that as the Vickers indenter is pushed into a bilayer structure, the materials immediately beneath the tip, is subjected to hoop and radial stresses produced by indentation pressure (P). Further deformation in radial direction is constrained by the ability of the interface to support the radial stress.

In this model two assumptions are considered as follows:

- There is no friction between the indenter tip and specimen.

- The stress distribution near the interface of coating and substrate is the same as that suggested by shear lag model.

Figure 5.3 shows a bilayer structure indented by Vickers punch. The bilayer structure consists of a thin film with thickness δ deposited on a substrate.

Near the interface plane, the deformation of the coating could be divided into three regions as described below:

1- AAAA region is placed immediately beneath the indenter. This region is subjected to indentation pressure, radial and hoop stresses.

2- BCAA region is under radial, hoop and shear stresses. The radial stress decreases and transfers to the shear stress in the outer region.

3- The outermost region is assumed to be a stress free zone.

The integration of τ over the half-wave length of the sinusoidal shape yields:

$$\sigma_r = \frac{1}{\delta}\int_0^r \tau dr = \frac{1}{\delta}\int_0^{\lambda/2} \tau_{\max} Sin\frac{\pi r}{\lambda/2} dr = \frac{4\tau_{\max}}{\pi} \qquad (5.6)$$

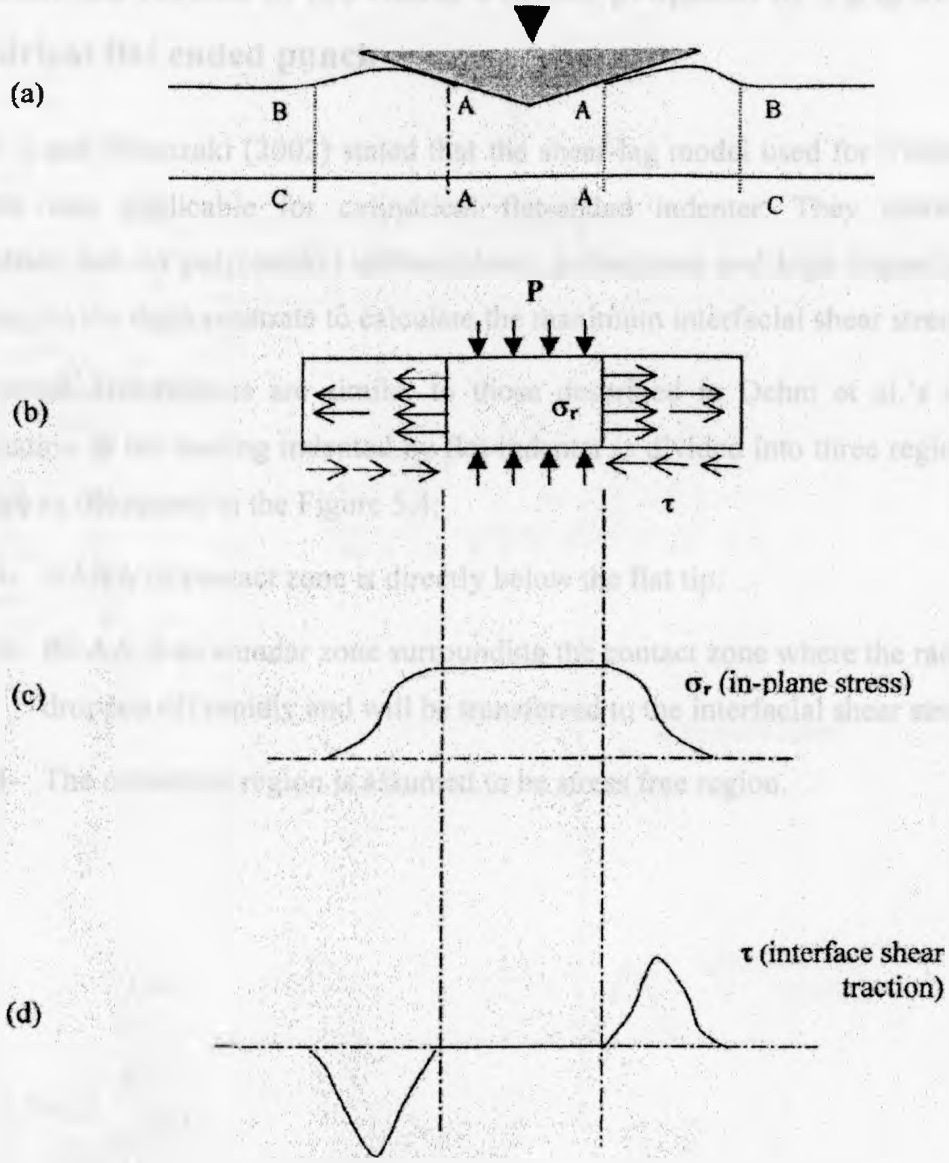

Figure 5.3: The schematic diagram of the shear lag model developed by Dehm et al. for vickers indenter (Lu 1999).

5.4 Modified version of the Dehm's model proposed by Lu et al. for cylindrical flat ended punch

Lu and Shinozaki (2002) stated that the shear-lag model used for Vickers pyramid indenter was applicable for cylindrical flat-ended indenter. They carried out flat indentation test on poly(methyl methacrylate), polystyrene and high impact polystyrene adhering on the rigid substrate to calculate the maximum interfacial shear stress.

Stress distributions are similar to those described in Dehm et al.'s model. The deformation of the coating indented by flat indenter is divided into three regions near the interface as illustrated in the Figure 5.4:

1- AAAA or contact zone is directly below the flat tip.

2- BCAA is an annular zone surrounding the contact zone where the radial stress is dropped off rapidly and will be transferred to the interfacial shear stress (τ).

3- The outermost region is assumed to be stress free region.

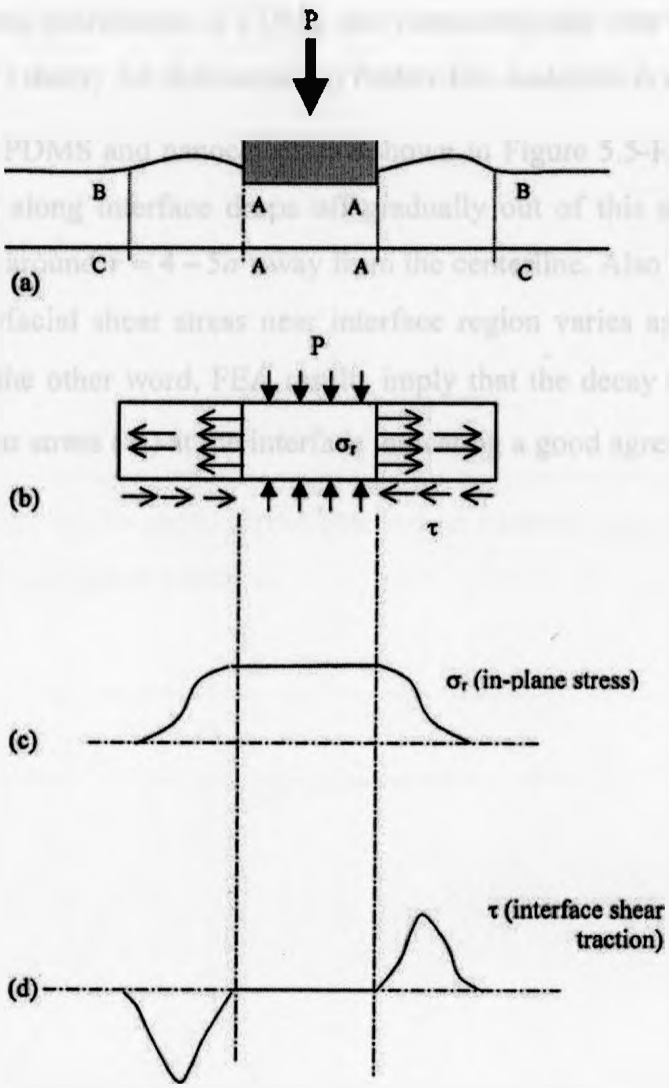

Figure 5.4: The schematic diagram of the shear lag model developed by Lu. Shinozaki for cylindrical flat-ended indenter (Lu 1999).

5.4.1 Stress distribution of PDMS and PDMS-clay nanocomposites near the interface

In this part stress distribution of PDMS and nanocomposite near the interface, and validity of the Dehm's theory for indentation of rubber-like materials is examined.

FEA results of PDMS and nanocomposite shown in Figure 5.5-Figure 5.8 indicate that the radial stress along interface drops off gradually out of this region and finally reaches to zero value around $r = 4 - 5a$ away from the centerline. Also Figure 5.9-Figure 5.12 reveal that interfacial shear stress near interface region varies approximately in a sinusoidal shape. In the other word, FEA results imply that the decay in the σ_r will be transferred to the shear stress (τ) at the interface indicating a good agreement with Dehm et al.'s model.

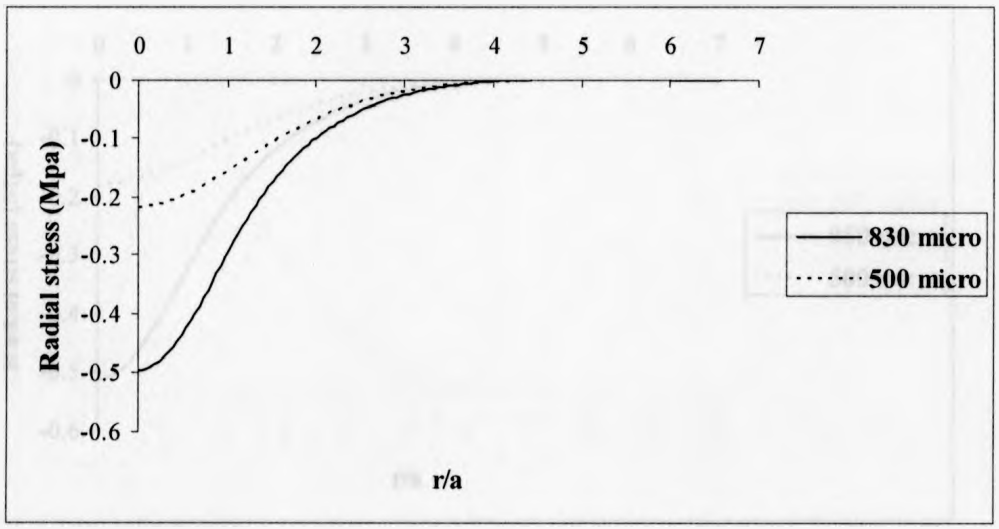

Figure 5.5: Distribution of the radial stress over *r/a* in various penetration depths near interface of PDMS-R_{11} and glass substrate.

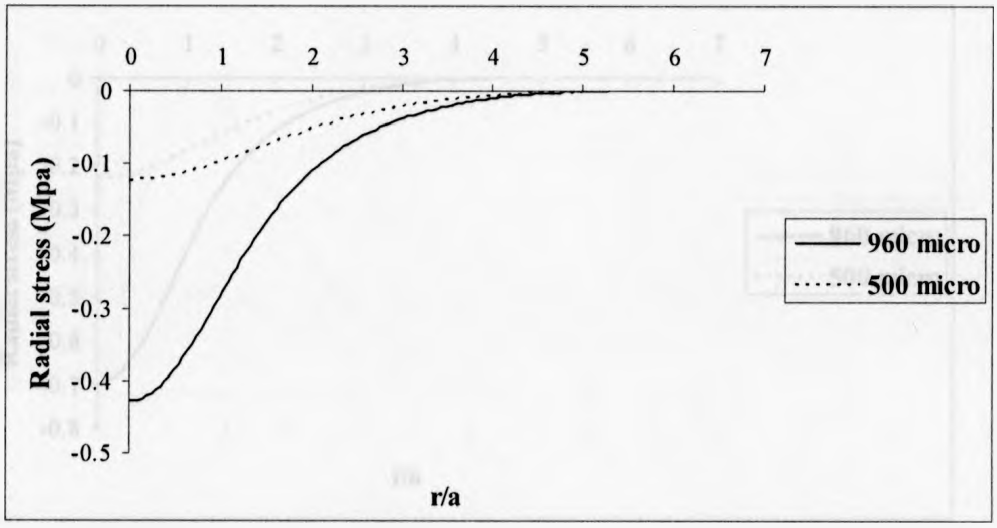

Figure 5.6: Distribution of the radial stress over *r/a* in various penetration depths near interface of PDMS-1% clay nanocomposite and glass substrate.

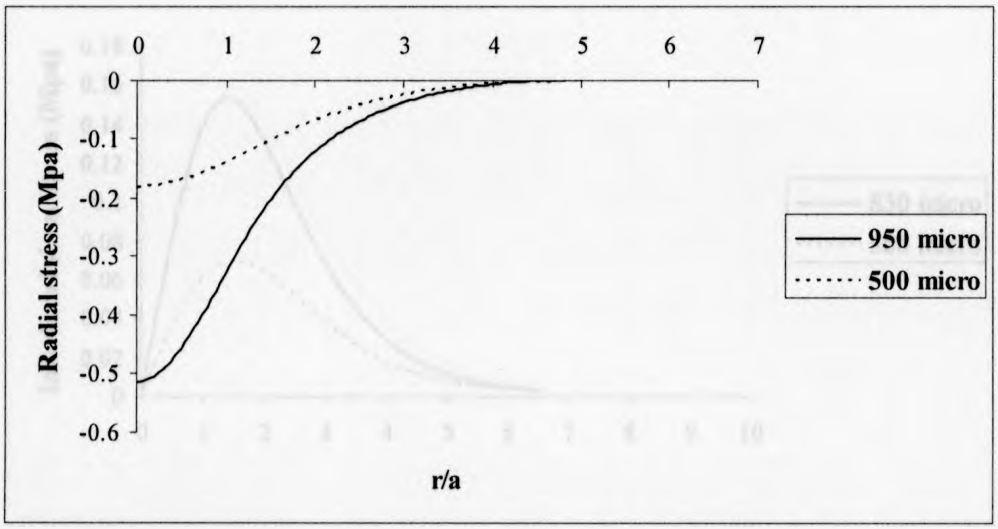

Figure 5.7: Distribution of the radial stress over *r/a* in various penetration depths near interface of PDMS-3% clay nanocomposite and glass substrate.

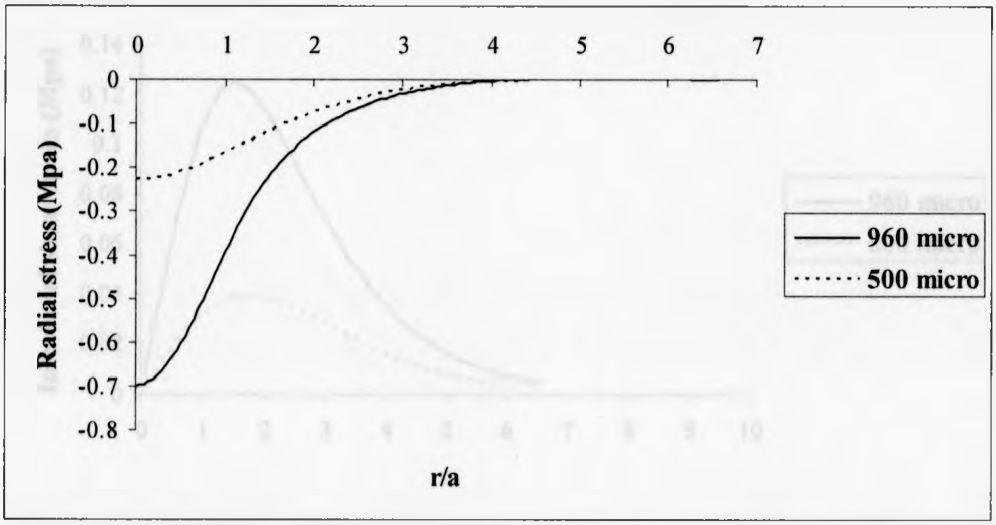

Figure 5.8: Distribution of the radial stress over *r/a* in various penetration depths near interface of PDMS-5% clay nanocomposite and glass substrate.

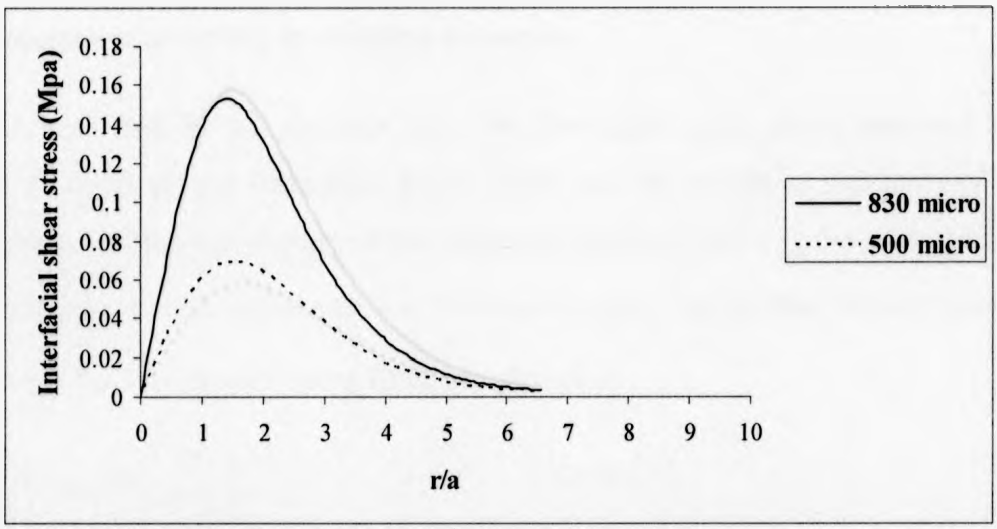

Figure 5.9: Distribution of the interfacial shear stress over *r/a* in various penetration depths near interface of PDMS-R_I1 and glass substrate.

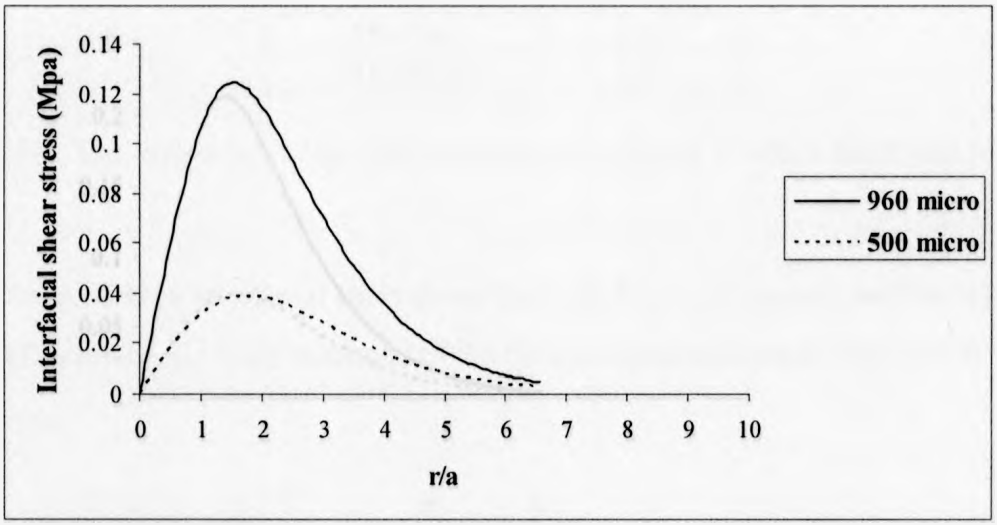

Figure 5.10: Distribution of the interfacial shear stress over *r/a* in various penetration depths near interface of 1% clay-PDMS nanocomposite and glass substrate.

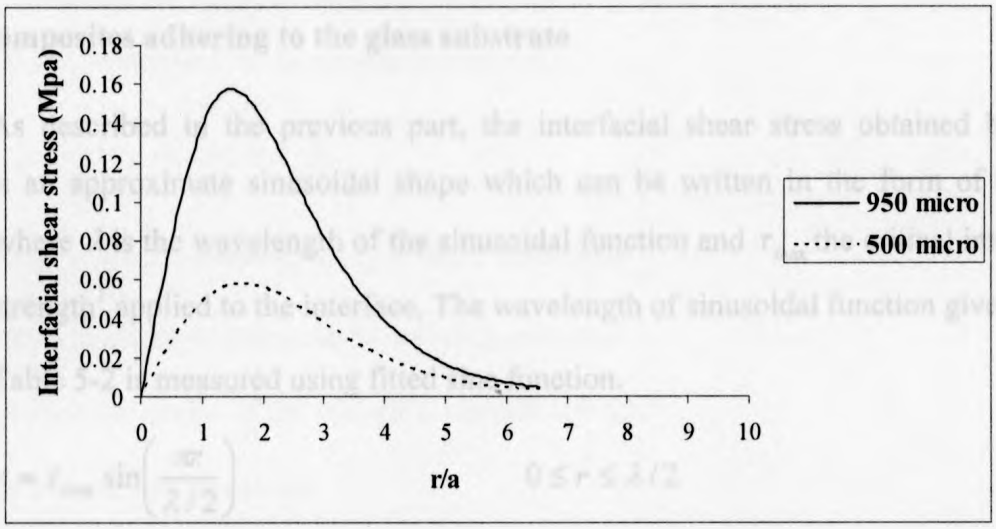

Figure 5.11: Distribution of the interfacial shear stress over *r/a* in various penetration depths near interface of 3% clay-PDMS nanocomposite and glass substrate.

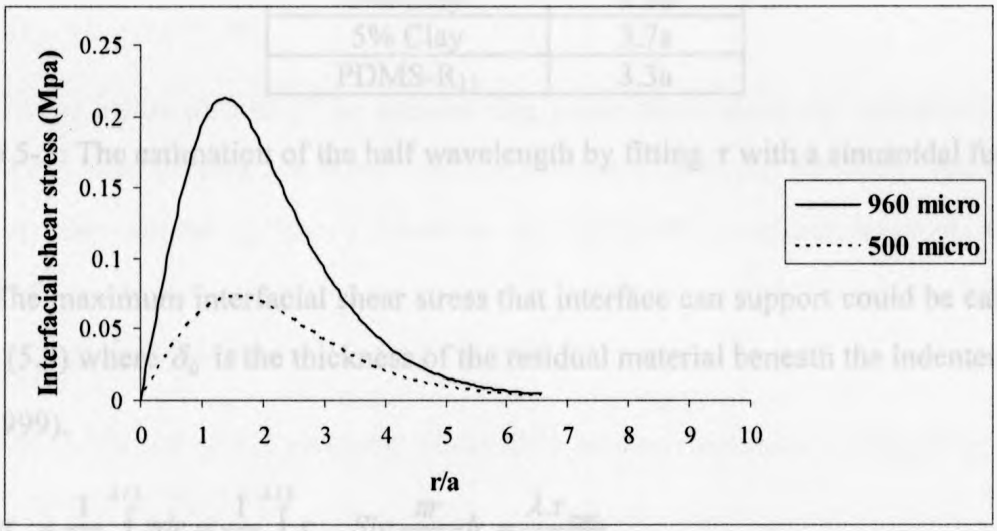

Figure 5.12: Distribution of the interfacial shear stress over *r/a* in various penetration depths (radial distance normalized by indenter radius) near interface of 5% clay-PDMS nanocomposite and glass substrate.

5.4.2 Estimation of the interfacial shear strength for PDMS and PDMS-clay nanocomposites adhering to the glass substrate

As described in the previous part, the interfacial shear stress obtained by FEA follows an approximate sinusoidal shape which can be written in the form of the Eq. (5.7), where λ is the wavelength of the sinusoidal function and τ_{max} the critical interfacial shear strength[1] applied to the interface. The wavelength of sinusoidal function given in Table 5-2 is measured using fitted sine function.

$$\tau = \tau_{max} \sin\left(\frac{\pi r}{\lambda/2}\right) \qquad 0 \le r \le \lambda/2 \tag{5.7}$$

	$\lambda/2$
1% Clay	3.5a
3% Clay	3.6a
5% Clay	3.7a
PDMS-R_{11}	3.3a

Table 5-2: The estimation of the half wavelength by fitting τ with a sinusoidal function

The maximum interfacial shear stress that interface can support could be calculated by Eq. (5.8) where δ_0 is the thickness of the residual material beneath the indenter tip (Lu et al. 1999).

$$\sigma_r = \frac{1}{\delta_0}\int_0^{\lambda/2} \tau dr = \frac{1}{\delta_0}\int_o^{\lambda/2} \tau_{max} Sin\frac{\pi r}{\lambda/2} dr = \frac{\lambda.\tau_{max}}{\pi.\delta_0} \tag{5.8}$$

To estimate the maximum interfacial shear strength, it is required to find a relationship between radial stress and indentation pressure. Dehm et al. solved this problem and used linear elastic model to make relationship between radial stress and indentation pressure. In spite of the hyperelasticity of the PDMS and PDMS-clay

[1] The maximum shear stress as interface fails called critical interfacial shear strength.

nanocomposites, the interfacial shear strength could be estimated by linear elasticity (Lotter et al. 1996, Sharp et al. 2004, White et al. 2005). Therefore, it is assumed that Eq.(5.9) can be applied for hyperelastic materials.

$$\varepsilon_\theta = \frac{1}{E}[\sigma_\theta - \upsilon(\sigma_r + \sigma_z)] \tag{5.9}$$

σ_r, σ_θ and P are the stress in the r, θ and z directions

E is elastic modulus of the material which is indented.

υ is the Poisson's ratio of the materials beneath the tip

ε_θ is the circumferential strain.

If AAAA part (Figure 5.4) immediately under the indentation tip is considered, it is understood that the stresses in the r, θ, z directions are σ , σ and –P respectively related to circumferential strain at the edge AA by Eq.(5.10).

$$E\varepsilon_\theta = (1-\upsilon)\sigma + \upsilon P \tag{5.10}$$

On the inside surface of the annular ring which constrained the deformation of the disc AAAA, the stresses are σ,$-\sigma$ and zero in the r, θ and z directions respectively. These stresses similar to above equation are linked to the circumferential strain by Eq.(5.11).

$$E\varepsilon_\theta = -(1+\upsilon)\sigma \tag{5.11}$$

Eqs.(5.10) and (5.11) yield the relationship between indentation pressure and radial stress as shown in Eq.(5.12).

$$-P = \frac{2\sigma}{\upsilon} \tag{5.12}$$

The maximum interfacial shear strength on the interfacial plane between thin film and glass substrate can be calculated by Eq. (5.13) .

$$\tau_{max} = \frac{\pi.\upsilon.P.\delta}{2\lambda} \tag{5.13}$$

	Thickness of the residual material beneath the indenter tip (δ_0)	Critical Indentation Debonding Stress P_c (MPa)	Critical interfacial shear strength (MPa)
PDMS-R_{11}	0.866	6.4	1.318
1% Clay	0.621	5.64	0.785
3% Clay	0.617	5.13	0.69
5% Clay	0.435	4.56	0.42

Table 5.3: The estimation of the critical interfacial shear strength of the PDMS and PDMS-clay nanocomposite thin films.

As shown in the Table 5.3, the interfacial shear strength decreases with the increase of the clay amount. The reason for this phenomenon might be the increase of the stiffness of the material. The raise of the stiffness leads to higher resistance of the material against deformation.

5.4.3 Effect of the cross-linker degree on the critical interfacial shear strength

In order to find out the effect of the cross-linker amount on the interfacial shear strength, indentation tests were carried out on PDMS thin films with R2.2, R5 and R11 adhering to the glass substrate. The load-displacement curves obtained from indentation test are shown in the Figure 5-13. No delamination or load drop was observed in the case of PDMS-R2.2 until the flat indenter reaches to the glass substrate. PDMS-R5 shows the higher critical load and depth compared to PDMS-R11. The critical interfacial strength values calculated by the Dehm's are given in Table 5.5. As explained in section 4.5, the function of cross linker is to increase the stiffness of composite and resistance against deformation which in turn results to lower critical load and depth for PDMS-R11. Figure 5-14 and Figure 5-15 shows the interfacial failure in the case of PDMS-R11 and PDMS-R5. The circular interfacial delamination zone interfacial is clearly visible around the indenter hole.

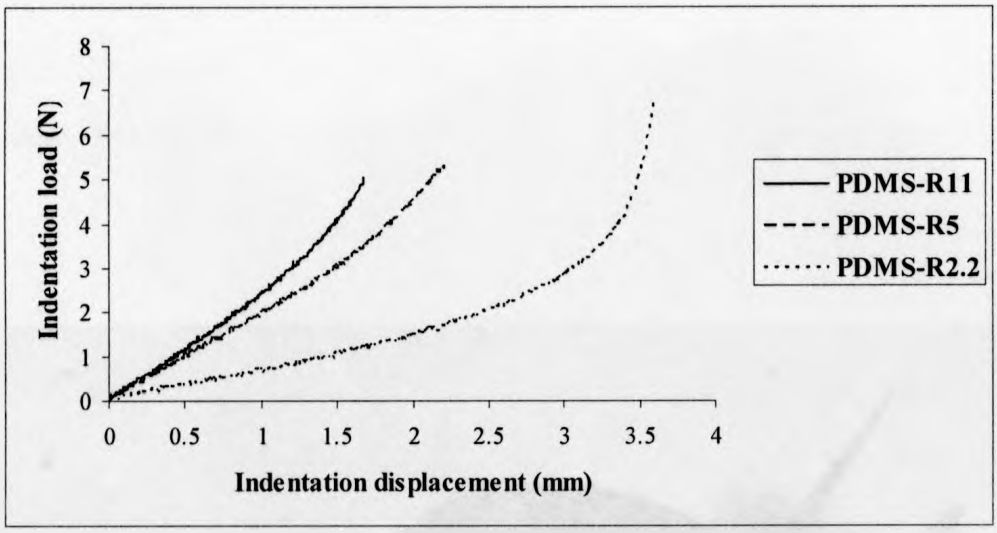

Figure 5-13: Indentation load-displacement curves of the PDMS with different amount of cross-linker.

	Coating Thickness (mm)	Critical Indentation Debonding Depth H_f (mm)	Critical Indentation Debonding Load F_c (N)	Critical Indentation Debonding Stress P_c (MPa)
PDMS-R_{11}	2.54	1.674	5.027	6.4
PDMS-R_5	3.3	2.211	5.326	6.784

Table 5.4: The critical indentation debonding load, stress and depth obtained from indentation curves of the PDMS-R_5 and R_{11} thin films adhering on the glass substrate.

	Thickness of the residual material beneath the indenter tip (δ_0)	Critical Indentation Debonding Stress P_c (MPa)	Critical interfacial shear strength (MPa)
PDMS-R_{11}	0.866	6.4	1.318
PDMS-R_5	1.089	6.784	1.757

Table 5.5: The estimation of the interfacial shear strength of PDMS-$R_{2.2}$, R_5 and R_{11} thin films according to the Dehm's model

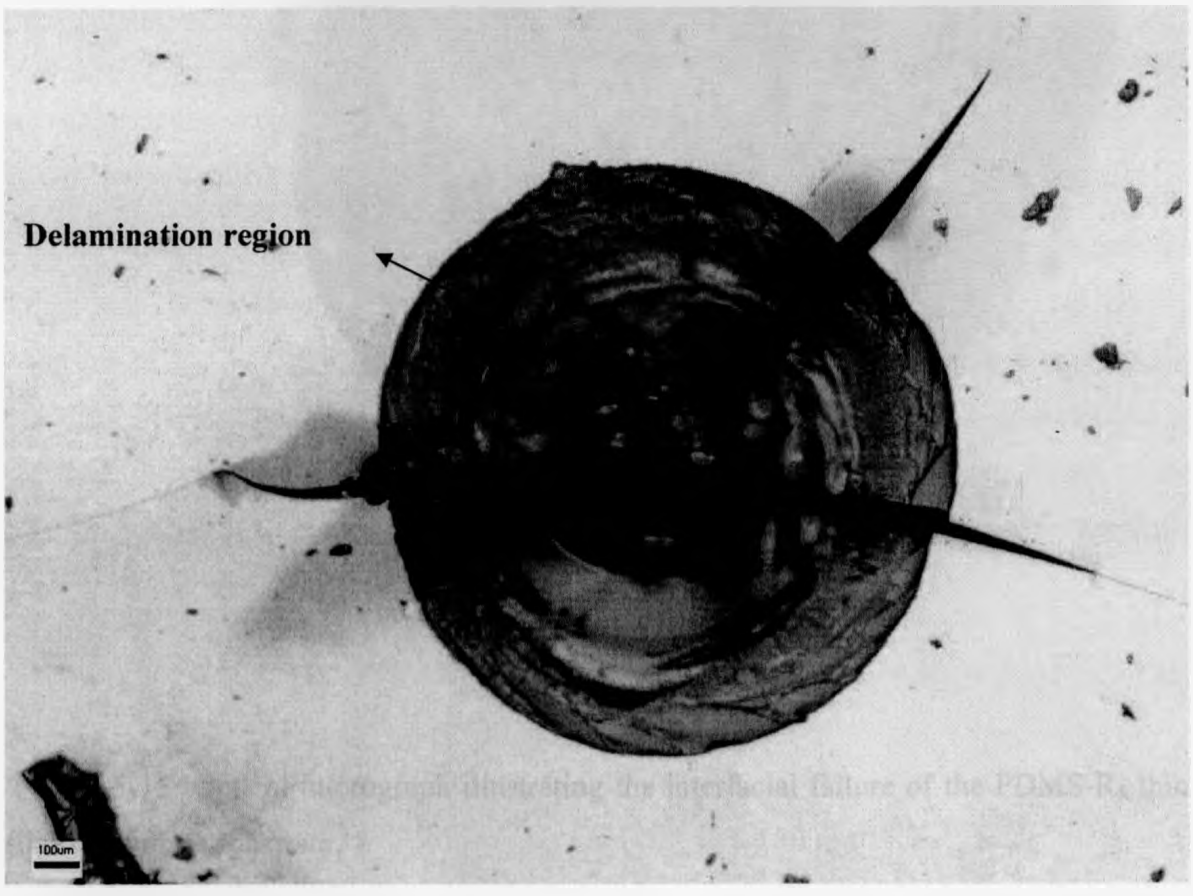

Figure 5-14: Optical micrograph illustrating the interfacial failure of the PDMS-R_{11} thin film from glass substrate.

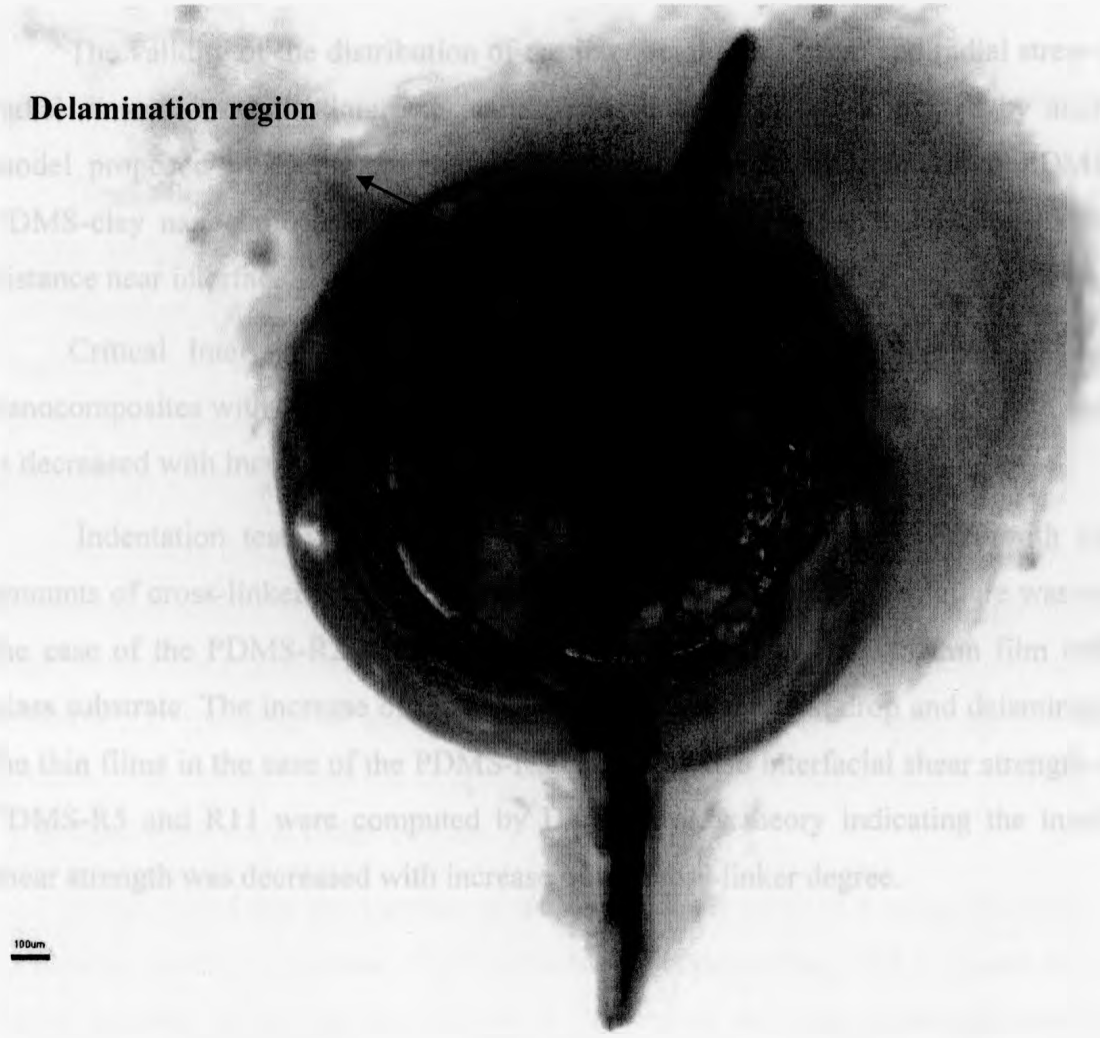

Figure 5-15: Optical micrograph illustrating the interfacial failure of the PDMS-R_5 thin film from glass substrate.

5.5 Conclusion

The validity of the distribution of the interfacial shear stress and radial stress along radial distance near the interface plane obtained by FEA was approved by analytical model proposed by Dehm. In the other word, interfacial shear stress of PDMS and PDMS-clay nanocomposites follows an approximate sinusoidal shape along the radial distance near interface.

Critical Interfacial shear strength was calculated for PDMS and PDMS-clay nanocomposites with 1%, 3% and 5 % clay. It was observed that interfacial shear strength is decreased with increasing the clay amount.

Indentation test was carried out for the thin films of the PDMS with various amounts of cross-linker adhering to the glass substrate. No interfacial failure was seen in the case of the PDMS-R2.2 indicating good adhesion of the PDMS thin film with the glass substrate. The increase of the cross-linker causes the load drop and delamination in the thin films in the case of the PDMS-R5 and R11. Also interfacial shear strength of the PDMS-R5 and R11 were computed by Dehm et al.'s theory indicating the interfacial shear strength was decreased with increase of the cross-linker degree.

Chapter 6. CONCLUSION

6.1 Indentation of the bulk PDMS and PDMS-clay nanocomposites

It was observed that the indentation load-displacement curves of thick blocks of PDMS and PDMS-clay nanocomposites were well-fitted to the Sneddon's theory. Comparison of the stress distributions (axial, radial, hoop and shear) along radial distance obtained by FEA with analytical model proposed by Sneddon (in the neighborhood of the flat punch) revealed that the results have a good consistency as the model, although the stress values were different from predicted values in the case of the hoop stress.

Increasing the amount of cross-linker increased the slope of the indentation load-displacement curves as well as elastic modulus. In addition the indentation debonding depth values were elevated. Interestingly no delamination was observed in the case of the PDMS-R2.2. The shape of stress contours examined at a specific depth were similar for samples with different amount of cross-linker, however the stress values were increased by increasing the cross-linker amount.

It was found that the increase of the clay amount up to % 5 raises the slope of the indentation load-displacement curves indicating that debonding load increases. However, further increase of the clay from % 5 to % 7 decreased the slope of the examined curves. This can be explained in the light of clay particles and cross-linking molecules interaction where excessive amount of clay prevents vulcanization. Examining the stress contours for various amounts of the added clay showed, while the shapes of these contours are the same, the stress magnitudes increase up to 5% clay due to improvement of the stiffness. However the stress values decrease in the case of 7% clay.

Finally it was confirmed that the crack initiation is a result of the tensile hoop stress.

6.2 Indentation of the thin film PDMS and PDMS-clay nanocomposites

The agreement between the distribution of the interfacial shear stress and radial stress along radial distance near the interface plane obtained by FEA and analytical model

proposed by Dehm was validated. It was shown that interfacial shear stress of PDMS and PDMS-clay nanocomposites follows an approximate sinusoidal shape along the radial distance near interface.

Interfacial shear strength was computed for PDMS and PDMS-clay nanocomposites with 1%, 3% and 5 % clay by Lu et al.'s model. It was concluded that interfacial shear strength is decreased with increasing the clay amount.

Indentation test was performed for the thin films of the PDMS with different amounts of cross-linker adhering to the glass substrate. No interfacial failure was seen in the case of the PDMS-R2.2 indicating good adhesion of the PDMS thin film with the glass substrate. The increase of the cross-linker causes the load drop and delamination in the thin films in the case of the PDMS-R5 and R11. Also interfacial shear strength of the PDMS-R5 and R11 were computed by Dehm et al.'s theory indicating the interfacial shear strength was decreased with increase of the cross-linker degree.

6.3 Future Work

1- Characterization of the mechanical properties of PDMS and nanocomposite at high temperature by indentation test, and investigation effect of the temperature on the interfacial shear strength.

2- Calculation of the interfacial shear strength of the PDMS and nanocomposite thin films adhering on a flexible substrate and modeling of the process using FEA.

3- Calculation of the interfacial shear strength in the case of 7% clay-PDMS nanocomposite and examination of the effect of clay increase up to 7%.

4- Investigation of the mechanical and conductive properties of the bilayer structure (Deposition of the metallic layer on the surface of the PDMS and nanocomposite thin films) by Micro tensile testing.

References

Agrawal. D.C and Raj. R, Measurement of the ultimate shear strength of a metal ceramic interface, Acta Materialia, 37, (1989) 1256-1264

Alexandre M. and Dubois P., Polymer-layered silicate nanocomposites: preparation, properties and uses of a new class of materials, Materials Science and Engineering, 28, (2000) 1-63.

Arruda, E.M. and Boyce, M.C., A three-dimensional co
nstitutive model for the large stretch behavior of rubber elastic materials, Journal of the Mechanics and Physics of Solids, 41, (1993)389-412.

Blatz, P.J. and Ko, W.L., Application of finite elastic theory to the deformation of rubbery materials, Transactions of the Society of Rheology, VI, (1962) 223-52.

Burnside. S. D and Giannelis . E. P, Synthesis and properties of new poly(dimethylsiloxane) nanocomposites, Chem. Mater. , 7, (1995) 1597-1600

Burnside. S. D and Giannelis . E. P, Nanostructure and properties of polysiloxane-layered silicate nanocomposites, J polym Sci, 38, (2000) 1595-1604.

Carrillo. F, Gupta. S, Balooch. M, Marshall. S. J, Marshall. G. W, Pruitt. L, Puttlitz. C, Nanoindentation of Polydimethylsiloxane elastomers: effect of crosslinking work of adhesion, and fluid environment on elastic modulus, J. Mater. Res. , 20, (2005) 2820-2830.

Chiang S. S., Marshall D. B. and Evans A. G., The response of solids to elastic/plastic indentation (fracture initiation), Applied Physics, 53, (1989) 312-318.

Choi S. T., Lee R. L. and Earmme Y. Y, Flat indentation of a viscoelastic polymer film on a rigid substrate, Acta Materialia, 56, (2008) 5377-5387.

Choi. S. T, Jeong. S. J and Earmme. Y. Y, Modified-creep experiment of an elastomer film on a rigid substrate using nanoindentation with a flat-ended cylindrical tip, Scripta Materialia, 58, (2008) 199-202.

Dehm. G, Ruhle. M, Conway. D. H and Raj. R, A microindentation method for estimating interfacial shear strength and its use in studying the influence of titanium transition layers on the interface strength of epitaxial copper films on sapphire, Acta Metallurgica, 45, (1997) 489-499.

Geng. K, Yang. F, Druffel. T, and Grulke. E. A, Nanoindentation-induced delamination of submicron polymeric coatings, Polymer, 48, (2007) 841-848.

Gent A. N. and Yeoh O. H., Small indentation of rubber blocks: effect of the size and shape of block and of lateral compression, Rubber Chemistry and Technology, (1954) 674-693.

Giannakopoulos. A. E and Triantafyllou .A, Spherical indentation of incompressible rubber-like materials, Journal of the Mechanics and Physics of Solids, 55, (2007) 1196-1211.

Giannakopoulos. A. Eand Panagiotopoulos. D. I, Conical indentation of incompressible rubber-like materials, International Journal of Solids and Structures, 46, (2009) 1436-1447.

Hofmann W, Title rubber technology handbook/Werner Hofmann, translated by Bauer R. and Meinecke E. A., Oxford University Press, c (1989)

Kraus, G. Reinforcement of Elastomers; Interscience Publishers: New York, 1965.

Kraus, G. In Science and Technology of Rubber; Eirich, F., Ed.; Academic Press: New York, 1978.

Li T. and Suo Z., Ductility of thin metal films on polymer susbtrates modulated by interfacial adhesion, Int. J. Solids Struct. 44, (2007) 1696-1705.

Lim. Y. Y and Chaudhri. M. M, Indentation of elastic solids with rigid cones, Philosophical Magzine, 84, (2004) 2877-2903.

Lim. Y. Y and Chaudhri. M. M, Indentation of elastic solids with a rigid vickers pyramidal indenter, Mechanics of Materials, 38, (2006) 1213-1228.

Livermore C and Voldman J 2004Material Properties Database, http://www.mit.edu/6.777/matprops/matprops.htm

Lötters J. C., Olthuis W., Veltink P. H. and Bergveld P., Polydimethylsiloxane as an elastic material applied in a capacitive accelerometer. J. Micromech. Microeng. 6, (1996) 52.

Lu N., Wang X., Suo Z. and Vlassak J., Metal films on polymer susbstrate stretched beyond 50%, Appl. Phys. Lett, 91, (2007).

Lu. Y, Deep penetration microindentation testing of polymers, PhD. Thesis, University of Western Ontario.

Lu. Y, Shinozaki. D. M, Microindentation induced debonding of polymer thin films from rigid substrates, Journal of Materials Science, 37, (2002) 1283-1293

Moloodi S. and Shinozaki D. M., M.Sc. Thesis, University of Western Ontario.

Mooney, M.,A theory of large elastic deformation, Journal of Applied Physics, 11, (1940) 582-92.

Patel S. K. , Malone S., Cohen C., Gillmor J. R. and Colby R. H., Elastic modulus and equilibrium swelling of poly(dimethylsiloxane) networks, Macromolecules, 25, (1992) 5241-5251.

Pavliotis G. A. and Holmes M. H., Journal of Engineering Mathematics, 43, (2002) 1-17.

Pinnavaia. T. J and Beall. G. W, Polymer-clay nanocomposites, Chichester, England, New York, Wiley, (2000)

Ray S. S., Okamoto K. and Okamoto M., Structure-property relationship in biodegradable poly(buthylenesuccinate)/layered silicate nanocomposites, Macromolecules, 36, (2003) 2355-2367.

Ritter J. E., Lardner T. J., Rosenfeld L. and Lin M. R., Measurement of adhesion of thin polymer coatings by indentation, Journal of Applied Physics, 66, (1989) 3623.

Rivlin, R.S. and Saunders, D.W, Large elastic deformations of isotropic materials, VII, experiments on the deformation of rubber", Mathematical and Physical Sciences, 243, (1951) 251-88.

Sharp K. G., Blackman G. S., Glassmaker N. J., Jagota A., and Hui C. Y., Effect of stamp deformation on the quality of microcontact printing: Theory and experiment. Langmuir 20, 6430 (2004).

Sneddon. I. N., Boussinesq's problem for a flat-ended cylinder, Mathematical Proceedings of the Cambridge Philosophical Society, 42, (1945) 29-39.

Tabor D., Indentation hardness of solids, Review of Physics in Technology, (1970) 145.

Takeuchi. H and Cohen. C, Reinforcement of poly(dimethylsiloxane) elastomers by chain-end anchoring to clay particles, Macromolecules, 32, (1999) 6792-6799.

Wang S., Long. C., Wang. X., Lu Q. and Qi Z., Synthesis and properties of silicon rubber/organomontmoriilonite hybrid nanocomposites, Journal of Applied Polymer Science, 69, (1998) 1557-1561

White C. C., Drzal P. L. and VanLandingham M. R. : Viscoelastic characterization of polymers using dynamic instrumented indentation, Journal of Polymer Science, 43, (2005) 1812-1824.

Wright. S. C, Huang. Y and Fleck. N. A, Deep penetration of polycarbonate by a cylindrical punch, Mechanics of Materials.13, (1992) 277-284.

Xiang Y., Li T., Suo Z. and Vlassak J., High ductility of a metal film adherent on a polymer substrate, Appl. Phys. Lett, 87, (2005).

Yeoh, O.H., Some forms of the strain energy function for rubber, Rubber Chem. Technol., 66, (1993) 754-71.

Yu. H. Y and Li. J. C. M. , Impression creep of LiF single crystals, Journal of Materials Science, 12, (1977) 2214.